# MAGNETIC STEERING TO SAVE SIGHT: TRABECULAR MESHWORK CELL THERAPY AS A TREATMENT FOR PRIMARY OPEN ANGLE GLAUCOMA

A Dissertation
Presented to
The Academic Faculty

by

M. Reza Bahrani Fard

In Partial Fulfillment
of the Requirements for the Degree
Doctor of Philosophy in Bioengineering in the
George W. Woodruff School of Mechanical Engineering

Georgia Institute of Technology
December 2023

# MAGNETIC STEERING TO SAVE SIGHT: TRABECULAR MESHWORK CELL THERAPY AS A TREATMENT FOR PRIMARY OPEN ANGLE GLAUCOMA

Approved by:


Dr. C. Ross Ethier, Advisor
The Wallace H. Coulter
Department of Biomedical Engineering
*Georgia Institute of Technology*
*Emory University School of Medicine*

Dr. Cheng Zhu
The Wallace H. Coulter
Department of Biomedical Engineering
George W. Woodruff
School of Mechanical Engineering
*Georgia Institute of Technology*

Dr. Stanislav Emelianov
The Wallace H. Coulter
Department of Biomedical Engineering
*Georgia Institute of Technology*

Dr. Johnna S. Temenoff
The Wallace H. Coulter
Department of Biomedical Engineering
*Georgia Institute of Technology*

Dr. Mark Prausnitz
School of Chemical & Biomolecular
Engineering
*Georgia Institute of Technology*


Date Approved: 11/29/2023

To those battling glaucoma.

# ACKNOWLEDGEMENTS

I extend my deepest gratitude to everyone whose collective support made this dissertation possible.

First and foremost, I am indebted to my advisor, Ross Ethier. His perspective on scientific conduct is encapsulated by a Margaret Mead quote (attributed) that he has incorporated in his email signatures — “Never doubt that a small group of thoughtful, committed citizens can change the world. Indeed, it is the only thing that ever has.” Ross’s unwavering support and guidance to his “small group” of researchers, of which I was privileged to be a part, have expanded my horizons and elevated my standards. I will forever value his mentorship.

I also want to express my thanks to my committee members: Stas Emelianov, Mark Prausnitz, Johnna Temenoff, and Cheng Zhu, for their invaluable feedback and the time they dedicated to refining this dissertation. Special appreciation goes to Stas for providing access to his laboratory resources, for his expertise, and enjoyable conversations.

Throughout my studies, I had the privilege of collaborating with several experts. I am extremely grateful to Markus Kuehn and Lin Cheng for their scientific contributions and resources. Wei Zhu, for countless days of experimental troubleshooting and multiple co-authorships. Becky Sappington, for the trainings on surgical procedures. Dan Stamer and Guorong Li, for expanding the scope of this work through their seemingly impossible experimental expertise. Andrew Feola, for supporting the initiation of this project and for his contagious optimism. Babak Safa, for being my go-to expert in times of crisis.

A heartfelt thanks goes out to my friends and colleagues: Tom, Mohammad, Jessica, Cydney, Nina, Gabriela, Anamik, Ogeda, Hazel, Richard, Andrea, Lisa, Stephen, Bailey, Saptarshi, Ankana, Haiyan, Gian, Edouard, Chris, for their contributions and for making this journey truly memorable.

This work would have never started to materialize if it were not for the mentorship of my master's degree advisor, Susan Hua. Her vote of confidence in my potentials has resonated with me in my moments of self-doubt.

My deepest appreciation goes to my family, friends Armin and Xena, and all others not explicitly named, for their invaluable support during grad school.

I acknowledge the funding sources for this work: NIH grant R01 EY030071 and the Georgia Research Alliance.

# TABLE OF CONTENTS

# LIST OF TABLES

# LIST OF FIGURES

# LIST OF SYMBOLS AND ABBREVIATIONS

Anterior chamber (AC)

Aqueous humor (AH)

Association for Research in Vision and Ophthalmology (ARVO)

Basement membrane material (BMM)

Carboxyfluorescein succinimidyl ester (CFSE)

Coefficient of variation (CV)

Corneoscleral trabecular meshwork (CTM)

Extracellular matrix (ECM)

Hematoxylin and eosin (H&E)

Human adipose-derived mesenchymal stem cells (hAMSC)

Induced pluripotent stem cells differentiated towards a trabecular meshwork phenotype (iPSC-TM)

Inner diameter (ID)

Inner wall of Schlemm's canal (IW)

Intraocular pressure (IOP)

Juxtacanalicular tissue (JCT)

Mesenchymal stem cells (MSC)

Normalized fluorescent pixel count (NFPC)

Off-target index (OTI)

Optimal cutting temperature (OCT)

Outer diameter (OD)

Periodic acid–Schiff stain (PAS)

Phosphate-buffered saline (PBS)

Primary human TM (phTM) cells

Primary open angle glaucoma (POAG)

Region of interest (ROI)

Retinal ganglion cell (RGC)

Schlemm’s canal (SC)

Superparamagnetic iron oxide nanoparticles (SPIONS)

Tg-MYOCY437H mice (Tg)

Trabecular meshwork (TM)

Trabecular meshwork stem cells (TMSC)

Uveoscleral trabecular meshwork (UTM)

Wildtype hybrid mice (WT)

# SUMMARY

Glaucoma, which affects almost 80 million people worldwide, is the main cause of irreversible blindness. The most common type, primary open angle glaucoma (POAG), causes gradual loss of vision by damaging retinal ganglion cells. The major risk factor for POAG is high intraocular pressure (IOP).

Current clinical treatments for POAG aim to reduce IOP, but they often have low success rates. The trabecular meshwork (TM) is a key regulator of IOP and has been shown to undergo significant changes in POAG including a loss of cells. This motivates the regeneration or restoration of the TM as a potential treatment for POAG. While TM cell therapy has shown promise in reversal of POAG pathology, previously-developed cell delivery techniques have resulted in poor cell delivery efficiency which elevates the risk of tumorigenicity and immunogenicity and undermines therapeutic potential. In addition, a lack of comprehensive characterization of the treatment effects in an appropriate POAG model is a roadblock to clinical translation.

We here tackled these shortcomings by: 1) using an optimized magnetic delivery method to significantly improve the specificity and efficiency of delivery of cells to the mouse TM, in turn reducing the risk of unwanted side-effects, and 2) employing this optimized method to test the therapeutic capabilities of two types of cells in a mutant myocilin mouse model of ocular hypertension, characterizing the morphological and functional benefits of the treatment. The central hypothesis of this work is that an optimized magnetically-driven TM cell therapy can lead to long-term clinically significant levels of IOP reduction while minimizing the risks associated with unwanted off-target cell-delivery.

This work resulted in the development of a novel magnetic TM cell therapy technique which outperformed those used previously. Employing this technique proved adipose-derived mesenchymal stem cells (hAMSC) and induced pluripotent stem cells differentiated towards a TM phenotype (iPSC-TM) to be effective in IOP lowering. Mesenchymal stem cells showed superior efficacy by stably lowering the IOP by 27% for 9 months, accompanied by increased cellularity in the conventional outflow pathway. These findings, bring magnetic TM cell therapy one step closer to clinical translation.

# CHAPTER 1. INTRODUCTION

## 1.1 Why is glaucoma important?

With nearly 80 million cases worldwide, glaucoma is the leading cause of irreversible blindness, and imposes a financial burden of at least $2.9B on the US annually (Tham et al., 2014). Glaucoma denotes a family of diseases, all of which are associated with pathological changes that lead to optic neuropathy. Of these, primary open angle glaucoma (POAG), the most common subtype of the disease and also the most prevalent in the US, progresses painlessly and results in a gradual loss of retinal ganglion cells (RGC) and a corresponding slow loss of vision. While a comprehensive understanding of the mechanism of glaucomatous damage remains elusive for POAG, an elevation in the intraocular pressure (IOP) has been identified as a major risk factor for the disease (Goel et al., 2010).

## 1.2 Dynamics of intraocular pressure

The eye is pressurized by aqueous humor (AH), secreted by the ciliary body in the posterior chamber to bathe the avascular tissues of the anterior chamber (AC) with nutrients and oxygen (Goel et al., 2010). Despite being derived from blood plasma through passive filtration and secretion (Goel et al., 2010), AH has 200 times less protein and 20-50 times higher ascorbic acid content than serum, likely to provide protection against the substantial oxidative stress in the anterior chamber (Dammak et al., 2023; Koskela et al., 1989). AH eventually exits the eye through two parallel outflow pathways located at the iridocorneal angle: (i) the unconventional (or uveoscleral) pathway, in which AH drains through the suprachoroidal space and re-enters the systemic circulation by traveling down an osmotic pressure gradient and being absorbed into the choroid or percolates across

the sclera (Johnson et al., 2017); and (ii) the conventional pathway (Figure 1), in which AH filters through the trabecular meshwork (TM) and Schlemm's canal (SC) before draining into the venous system (Hogan et al., 1971).

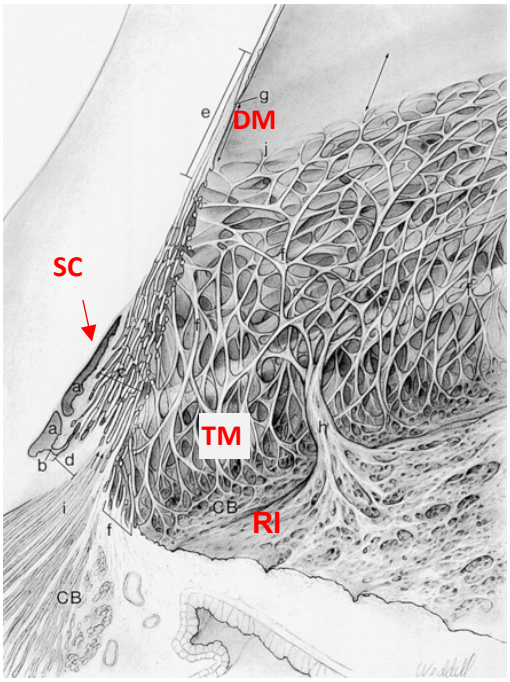


Figure 1. Anatomy of the iridocorneal angle. SC, Schlemm's canal; TM, trabecular meshwork; RI, root of iris; DM, transition region between the end of Descemet's membrane and start of TM. From (Hogan et al., 1971).

The relationship between the dynamics of aqueous humor and IOP can be explained by conservation of mass (Brubaker, 2004) where the inflow rate, or rate of AH production, equals the sum of outflows. At steady state, both the rate of AH production and unconventional outflow rate are generally assumed to be IOP-independent (Acott et al., 2014; Johnson et al., 2017). The conventional outflow pathway can be modeled as a hydraulic resistor, for which the pressure drop across the tissue equals the product of its hydraulic resistance and flow rate. The numerical inverse of this hydraulic resistance is a pressure-dependent parameter called outflow facility which is widely used in quantifications of IOP homeostasis (Brubaker, 2003).

### 1.3 Clinical treatment of glaucoma

Currently, reduction of IOP is the only clinical target for treating glaucoma. Aside from changes in the systemic blood pressure (Klein et al., 2005) or changes in the volume of the eye caused by internal or external factors, which are mainly transient and pulsatile in nature (van den Bosch et al., 2022), IOP can be lowered in several ways (Goel et al., 2010):

- A decrease in the rate of AH production,
- An increase in drainage rate via the uveoscleral outflow pathway, or
- A lowering of the flow resistance of the conventional outflow pathway tissues.

All clinical treatments for glaucoma focus on either medicinal suppression of AH production (e.g. beta blockers, alpha agonists), increasing unconventional outflow rate (e.g. prostaglandin analogs, alpha agonists), or reducing the hydrodynamic resistance of the conventional outflow pathway using drugs (e.g. miotics, rho kinase inhibitors, prostaglandin analogs) or surgical procedures such as trabeculectomy and MIGs (Tsai and Kanner, 2005; Weinreb et al., 2014). Despite these treatments, the disease continues to progress in 25-45% of patients (Heijl et al., 2002; Noecker, 2006). This poor outcome is due to a combination of low adherence to the self-administration of the eye drops by patients, and to low success rates of surgical methods (Barnebey and Robin, 2017; Reardon et al., 2011). New treatment strategies are thus required, and such novel treatments should combine long-term effectiveness with good repeatability, a high success rate and a low risk profile.

## 1.4 The TM in POAG

The TM is an anatomically complex connective tissue, consisting of an intricate filtration system that, in the human eye, can be broken down into three main layers. The first of these is the uveal meshwork, which lies innermost within the TM. It is comprised of large flow passages created by beam-like extracellular matrix (ECM) covered with TM cells (Fig. 2). Further exteriorly, the beams become more condensed to create the second layer (the corneoscleral meshwork), which contains narrower flow passages. Finally, the third (outermost) layer is the juxtacanalicular tissue (JCT), in which cells are embedded in a porous connective tissue gel.

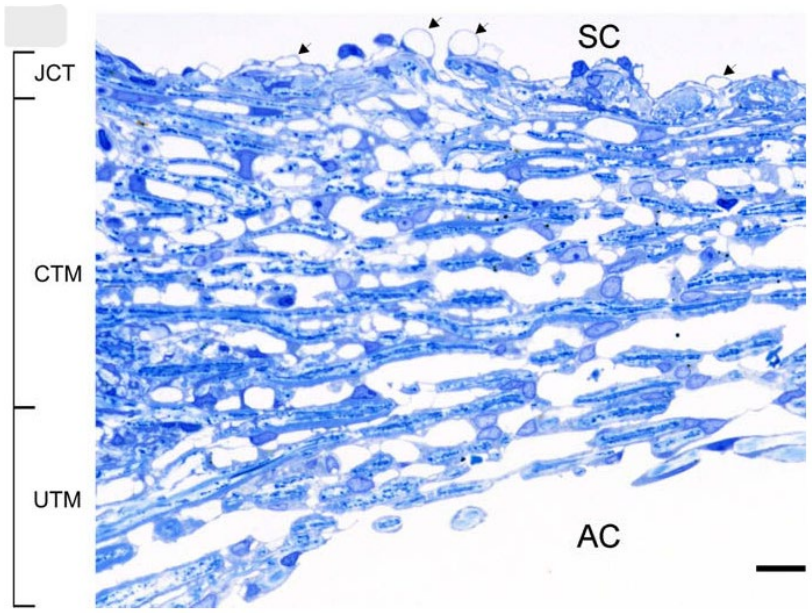


Figure 2. Various layers of trabecular meshwork. Light micrograph shows three regions of the TM in a human eye: the innermost uveoscleral (UTM), the corneoscleral (CTM), and the juxtacanalicular tissue (JCT). Scale bar is 5 μm (Tamm, 2009).

The innermost TM cells are highly phagocytic and tend to collect larger debris from the AH to avoid occlusion of the narrower downstream passages (Abu-Hassan et al., 2014). The JCT, along with the adjacent inner wall endothelial cells of SC, provides the

majority of flow resistance in the conventional outflow pathway (Ethier et al., 1986; Goel et al., 2010). This pressure drop is not constant — instead, it is actively regulated by the JCT cells and inner wall cells, likely through exertion of contractile forces and ECM turnover as well as other structural changes (Acott et al., 2014).

The conventional outflow pathway, particularly the TM, undergoes significant changes in POAG, while the rate of AH production and uveoscleral outflow rates remain largely unchanged (Alm and Nilsson, 2009; Gong and Swain, 2016a). Importantly, TM cellularity reduces with age so that nearly half of the TM cells are lost by 80 years of age; further, this rate of cell loss is ~30% greater in POAG patients (Alvarado et al., 1984). Such a pathological decline in cell number seems to only impact the inner layers of the TM, while the JCT instead experiences an abnormal deposition of inner wall basement membrane and “plaque material” derived from the sheath of the elastic-like fibers (Gong and Swain, 2016b; Lütjen-Drecoll et al., 1986). The abnormal ECM deposition is not limited to the JCT and significant accumulations of fibronectin, laminin, and collagen can be observed throughout the TM in POAG (Gong and Swain, 2016a; Vahabikashi et al., 2019). Interestingly, the deposition of type VI long-spacing collagen in TM beams has been associated with TM cell loss (Hirano et al., 1989; Lütjen-Drecoll et al., 1989). This abnormal deposition of ECM may be correlated with an increase in transforming growth factor-β2 (TGF-β2) in the AH, which promotes ECM formation and suppresses its degradation thus leading to increased tissue stiffness (Tripathi et al., 1994; Vahabikashi et al., 2019).

While a complete understanding of the mechanisms of IOP homeostasis by TM cells remains elusive, the aforementioned pathological changes including increased ECM deposition, tissue stiffening, and TM cell loss which likely leads to the fusion of denuded TM beams (Gong and Swain, 2016b), are consistent with an increase in pressure drop

across the conventional outflow pathway tissues and the consequent elevation of IOP which is a hallmark of POAG (Tamm and Fuchshofer, 2007).

## 1.5 Why consider stem cell therapy?

The loss of TM cellularity, and the complications linked to this loss, motivate regeneration/refunctionalization of the TM as a potential treatment for POAG. A common approach to tissue regeneration/refunctionalization is implantation of stem cells or stem cell derivatives (Bianco and Robey, 2001; Polak and Bishop, 2006), and similar ideas have been considered to treat POAG, as described in detail below (Manuguerra-Gagné et al., 2013; Roubeix et al., 2015; Yun et al., 2018; Zhou et al., 2020; Zhu et al., 2017, 2016). Such a cell therapy-based approach for POAG has the potential to outperform conventional treatments by meeting the key requirements mentioned earlier: the integration of new cells with the native tissue could enable long-lasting therapeutic benefits, while the minimally invasive nature of stem cell delivery into the eye could increase the repeatability and success rate with low risk profile.

## 1.6 Previous work on TM cell therapy

Several studies have shown the effectiveness of TM cell therapy in restoring or partially restoring TM function and IOP homeostasis. Three different types of cells have previously been used for TM cell therapy: TM stem cells (TMSC), mesenchymal stem cells (MSC) and induced pluripotent stem cell (iPSC) derivatives. We consider each of these in turn.

### *1.6.1 TM stem cells (TMSC)*

TMSCs are naturally present in the healthy eye, being located in the “insert” (non-filtering anterior) region of the TM. They have been successfully isolated and characterized by

several groups (Castro and Du, 2019; Du et al., 2012; Kelley et al., 2009; Yun et al., 2018). Interest in the regenerative capacity of this stem cell population grew after observing a multifold increase in TM cell proliferation in response to laser trabeculoplasty, a common treatment for POAG (Samples et al., 1989). The Du lab has previously investigated the therapeutic effects of human TMSC intracameral injection (performed through the periphery of the cornea into the AC) in mice with laser-damaged TM, and in transgenic mice carrying the Y437H mutation in the myocilin protein (Xiong et al., 2021; Yun et al., 2018). Tg-MYOC$^{Y437H}$ mice, as this latter model is named, are a model of myocilin-associated glaucoma in humans, expressing human myocilin with a pathogenic mutation which leads to TM cell loss as well as IOP elevation, reduction in outflow facility (inverse of outflow pathway hydraulic resistance) and retinal ganglion cell (RGC) loss (Xiong et al., 2021; Zode et al., 2011). The studies of Du and colleagues together suggested that TMSC treatment led to a reduction in IOP, an increase in outflow facility, improved TM structure, increased TM cellularity and neuroprotection, as compared to the saline-injected (sham) controls. While therapeutically beneficial, due to their scarcity, consisting of only 2-5% of the entire TM cell population (Braunger et al., 2014; Yun et al., 2018), and the invasiveness of the cell collection procedure, TMSC therapy is not an appealing target for clinical translation.

### *1.6.2 Mesenchymal stem cells (MSCs)*

The precursor of TM cells is neural crest cells that undergo epithelial to mesenchymal transition (Johnston et al., 1979; Tripathi and Tripathi, 1989). This fact makes multipotent MSCs an attractive choice for TM cell therapy. Manuguerra-Gagné et al. used laser photocoagulation of the TM in rats as a model to test the regenerative capacity of mouse bone marrow-derived MSCs (Manuguerra-Gagné et al., 2013). Similar to the TMSC studies, the authors reported a short-term (2-3 weeks) decrease in the IOP of MSC-

injected eyes compared to sham control eyes. Notably, a fast-decaying survival rate for the injected MSCs was observed, with only 0.2% of the originally injected cells detectable in the anterior segment after 4 days. Bone marrow MSCs have also been used to treat rats with ocular hypertension induced by cauterization of episcleral veins (Roubeix et al., 2015). The MSC treatment resulted in a reduction in IOP which was gradually lost after two weeks. Neuroprotection was also evidenced by the preservation of RGCs in the treatment group vs. sham control. These results, together with the ease of sourcing autologous cells, and the established safety of MSCs for stem cell therapy in clinical trials, make these stem cells a strong candidate for clinical cell therapy for POAG.

### *1.6.3 Induced pluripotent stem cell (iPSC) derivatives*

iPSC derivatives have also been used for TM regeneration (Abu-Hassan et al., 2014; Zhu et al., 2017, 2016). In particular iPSCs can be differentiated into a phenotype similar to adult TM cells known as iPSC-TM cells (Ding et al., 2014). Abu-Hassan et al. used human and porcine anterior segment perfusion systems and induced cell death in the TM by saponin perfusion. Intracameral injection of iPSC-TMs into this POAG model restored the homeostatic response of the outflow pathway and resulted in increased outflow rate (Abu-Hassan et al., 2014). Zhu et al. delivered iPSC-TMs into the eyes of Tg-MYOC$^{Y437H}$ mice and reported a marked decrease in IOP and an increase in outflow facility for up to 9 weeks after injection as compared to sham control eyes. The treatment also increased TM cellularity through promoting the proliferation of endogenous cells (Zhu et al., 2017, 2016). These qualities of iPSC-TM cells put them on par with MSCs as a promising clinically-relevant cell type for TM cell therapy.

## 1.7 What are the challenges?

Despite the previous studies showing the potential usefulness of TM cell therapy as a treatment for POAG, there is much room for improvement. One area needing improvement is the delivery method. All the studies mentioned above rely on hydrodynamic forces generated by the flow of AH to passively carry cells injected into the anterior chamber to the TM, resulting in considerable undesirable delivery to the surrounding tissues, such as the lens and the iris (Wang et al., 2022). These off-target deliveries increase the risk of tumorigenicity (Lamm et al., 2016; Sun et al., 2015; Vitale et al., 2017) and immunogenicity (Zhou et al., 2020). In particular, Zhou et al. injected wildtype mice with adipose-derived MSCs, and even though the treatment did not alter IOP, they reported an increase in cells on the iris and the cornea showing the inflammatory markers CD45, GR1, CD4, and CD3, likely due to off-target delivery of MSCs (Zhou et al., 2020). The efficiency and desirability of this “passive” delivery method is further challenged by the segmental (spatially non-uniform) nature of AH outflow. It has been shown that only one-third of the circumference of the conventional outflow pathway is actively filtering AH at any time (Chang et al., 2014a; Vranka and Acott, 2017), and that the flow becomes even more segmental in glaucomatous eyes (de Kater et al., 1989). This means that only a fraction of the TM receives passively-transported injected cells, which is very undesirable. All these factors substantially limit the therapeutic potential of passive delivery and thus justify the need for a more targeted, “active” method of TM cell therapy.

The data on more targeted delivery methods is scarce. Our lab has previously utilized a magnetic labeling approach to deliver MSCs to the TM in a post mortem porcine anterior segment perfusion model (Snider et al., 2021, 2018). For this purpose, the MSCs were labeled with superparamagnetic iron oxide nanoparticles (SPIONSs) to enable their steering inside the AC by an external magnetic field created by a ring magnet placed

externally at the circumference of the cornea. While this method showed effectiveness in terms of increasing the proportion of cells delivered to the angle tissues adjacent to the TM, the anterior segment perfusion model used in this study did not allow for full quantification of relevant therapeutic outcomes (Snider et al., 2018). Wang et al. also tested magnetic delivery of iPSC-TMs using a ring magnet in the more standard Tg-MYOC$^{Y437H}$ mouse model, but the study was mainly focused on the *in vivo* tracking of the cells using MRI and near-infrared imaging and did not quantify much of the therapeutic benefits of cell transplantation (Wang et al., 2022). Nevertheless, they showed that even though using the ring magnet increased the number of cells delivered to the iridocorneal angle by 4-fold, more than two-third of the cells were delivered to other to off-target tissues in the AC.

To develop and to test a more targeted TM cell therapy, it is imperative to evaluate the safety and effectiveness of such method in an animal model of POAG. While several POAG models exist in larger animals such as monkeys, cats, and rabbits these models do not capture as many pathological changes in the TM as does the myocilin mutant Tg-MYOC$^{Y437H}$ mouse model. For example, the monkey photocoagulation model, in which the TM is damaged by laser irradiation, produces ocular hypertension and is prized for its anatomical resemblance to humans in the posterior segment (Wang et al., 1998). However, the laser-induced damage to the TM is very unlike changes seen in POAG. Notably, there are changes in TM ECM structure and promotion of endogenous cell regeneration, both of which are confounding factors when evaluating the effects of TM cell therapy. The same can be said of laser models in other species (Candia et al., 2010; Gelatt and Mackay, 1998; Gerometta et al., 2004), and of microbead and hypertonic saline models (Morrison et al., 1997; Sappington et al., 2010). In addition to these larger animals, commercially available DBA/2 inbred mice exhibit IOP elevation and RGC loss within 9

months of age. However, this strain experiences significant systemic and ocular complications such as corneal calcification which can result in inaccurate IOP measurements by rebound tonometry (Turner et al., 2017).

On the other hand, Tg-MYOC$^{Y437H}$ mice undergo normal TM development, with pathology emerging slowly as the animal ages, as in POAG (Zode et al., 2011). Together, normal TM development, loss of TM cellularity, and a gradual increase in the IOP makes this model more suitable for testing TM cell therapy than other options. However, this model has a downside–the ocular volume is a nearly 400-fold smaller than in human eyes, requiring extensive training and skills for performing ocular surgeries (Bekerman et al., 2014). The small (~150 μm) length of the TM and its location deep in the iridocorneal angle further complicates targeted cell delivery.

In summary, the clinically proven merits of cell therapy for regenerative medicine in other disease contexts, and the promising results observed in previous TM cell therapy studies, motivate the further development of this method as a potential treatment for POAG. However, the translation of this treatment to clinical practice requires better characterization of the technique and its therapeutic benefits, focusing on appropriate combinations of the glaucoma model, choice of cell type, and delivery method.

# CHAPTER 2. SPECIFIC AIMS

**Central hypothesis:** An optimized magnetically-driven TM cell therapy can restore IOP homeostasis while minimizing unwanted off-target cell-delivery effects.

Current treatments for POAG suffer from low success rates. While TM cell therapy has shown promise as an alternative treatment strategy, previously-developed cell delivery techniques have resulted in poor cell delivery efficiency which elevates the risk of tumorigenicity and immunogenicity and attenuates therapeutic potential. Even though more targeted magnetic delivery techniques have recently been developed, a lack of comprehensive characterization of the treatment effects using these methods in an appropriate POAG model hinders clinical translation (Coulon et al., 2022). The overall objective of this study is to develop and test a novel magnetic TM cell therapy method in a standard POAG animal model and to comprehensively characterize its therapeutic benefits as a treatment for POAG.

## 2.1 Specific Aim 1: Design, develop, and test a surgical approach to improve the delivery quality of TM cell therapy in mice

Most of the studies on TM cell therapy directly inject the cells in the AC for them to be carried to the iridocorneal angle by the flow of AH. Yet, when using this technique, less than 10% of cells reach the target tissue and their circumferential distribution is limited by the segmental nature of aqueous humor outflow (Chang et al., 2014b; Wang et al., 2022). In an alternative approach, some studies have labeled cells with magnetic nanoparticles and used a ring-shaped magnet to drag them to the angle after injection. This method also proved inefficient as less than 30% of cells reached the target in the mouse eye. We proposed a magnetic delivery method with a focused magnetic field (called the “point

magnet" henceforth) for improved targeting of the cells to the TM. To rigorously test this approach, we created a specific surgical setup and developed a standardized surgical protocol.

**Approach**: An integrated surgical platform was designed and fabricated which allowed for:

- Precise positioning of the injection apparatus, the steering magnet and the IOP measurement equipment with respect to the mouse eye.
- Spatiotemporal control over delivery of cells to the iridocorneal angle.

This surgical setup was then be used to compare the uniformity and specificity of cell delivery using three candidate steering methods: a point magnet, a ring magnet, and passive delivery (control). Cells were fluorescently labeled prior to injection into the eyes of wildtype (WT) mice, and histological sections were morphometrically analyzed in relevant tissues post-delivery.

**Impact**: The results of this aim were instrumental in determining the preferred magnetic delivery technique to be used in Specific Aim 2, and can be additionally insightful for determining the risk of unwanted off-target cell deliveries.

### *2.2* Specific Aim 2: Perform magnetic TM cell therapy in a standard mouse model of POAG followed by comprehensive analysis of the therapeutic benefits

Previous studies have mainly focused on characterizing the therapeutic benefits of passive TM cell delivery and more targeted approaches were not fully studied.

**Approach**: A colony of Tg-MYOC$^{Y437H}$ mice was established. Experimental groups received injections with saline (control), magnetically-labeled MSCs, or magnetically-labeled iPSC-TMs using the point magnet method, optimized in Specific Aim 1. Outcome measures (IOP, outflow facility, TM ECM density, TM cellularity, and cell retention) were obtained at baseline, short-term, and long-term time points.

**Impact**: These results will help determine the following: 1) The extent and longevity of treatment effectiveness in lowering the IOP as the main clinical target of POAG treatment, 2) the degree of correlation between IOP lowering and refunctionalization of the conventional outflow pathway, particularly the TM, and 3) a comparison of the performance of MSC and iPSC-TM cells as the cell types with potential for clinical translation.

# CHAPTER 3. A COMPREHENSIVE PROTOCOL FOR MICROBEAD-INDUCED OCULAR HYPERTENSION IN MICE

This chapter is adapted from a book chapter accepted for publication at Glaucoma:

Methods and Protocols by Springer Protocols.

M Reza Bahrani Fard, Nina Sara Fraticelli Guzmán, Jessica Chan, A Thomas Read, Andrew Feola, W Daniel Stamer, Simon WM John, C Ross Ethier, Rebecca M. Sappington (2023). “A comprehensive protocol for microbead-induced ocular hypertension in mice” In: *Glaucoma: Methods and Protocols*, in Press.

* Some figures are repositioned (without changing content) and lists are reformatted in this chapter compared to the accepted manuscript for consistency across the dissertation.

## 3.1 Abstract

Glaucoma is a common optic neuropathy characterized by degeneration of retinal ganglion cells (RGCs). Elevated intraocular pressure (IOP), i.e. ocular hypertension, is the primary modifiable risk factor for glaucoma and the primary characteristic of most preclinical glaucoma models. Extensive genotype and phenotype diversity at relatively low cost and high accessibility makes laboratory mice an excellent preclinical model for glaucoma. The microbead occlusion model was introduced in 2010 (Sappington et al., 2010) as an inducible model of ocular hypertension in mice and is now one of the most extensively utilized models of rodent glaucoma. Subsequent modifications of the microbead model increased the magnitude and duration of IOP elevation, primarily through modification of injection materials (Chen et al., 2011; Cone et al., 2010; Frankfort et al., 2013; Samsel et al., 2011). Despite its popularity, the accessibility of the model may

be hindered by procedural inconsistencies between users. Here we outline an updated and comprehensive protocol for the execution of the microbead model that is focused on improving surgical and outcome measure consistency and on enabling single experimenter execution.

**Key Words**: intraocular pressure, glaucoma, mouse model, ocular hypertension, rodent, microbead

**Running Title**: Murine Microbead-induced Glaucoma

The glaucomas are a family of optic neuropathies which together are the most common cause of irreversible blindness worldwide. Loss of visual function in glaucoma is due to dysfunction and degeneration of retinal ganglion cells (RGCs), and many features of this pathologic process remain poorly understood, necessitating the need for animal models of the disease.

Ocular hypertension (OHT) is the primary modifiable risk factor for glaucoma and the primary characteristic of most preclinical glaucoma models. Many groups have described various methods for inducing OHT in various species, including mice, rats, tree shrews, rabbits, cows and non-human primates. Here we focus on the microbead model in mice, for several reasons. First, mice offer extensive genotype and phenotype diversity at relatively low cost and high accessibility. Second, the microbead occlusion model of OHT, first introduced in 2010 (Sappington et al., 2010), is now widely used in mice. The basic premise of the model is that normal aqueous humor drainage can be artificially impeded by physical blockade at the iridocorneal angle (Sappington et al., 2010).

The initial protocol for microbead-induced OHT relied upon hydrodynamic forces of aqueous humor flow to passively deposit injected microbeads in the outflow pathway

(Calkins et al., 2018; Sappington et al., 2010), which typically resulted in a 20% elevation in IOP that lasted for 4 weeks (Sappington et al., 2010). Subsequently, the protocol was adjusted to increase the duration and magnitude of IOP elevation (Chen et al., 2011; Cone et al., 2010; Samsel et al., 2011). The most widely-utilized modification is the use of magnetic microbeads, in which magnetic microbeads are injected intracamerally and then manually "steered" by an externally applied magnetic field to deposit the microbeads in the iridocorneal angle (Ito et al., 2016; Samsel et al., 2011). This active process reduces errant deposition of microbeads elsewhere in the anterior chamber (Samsel et al., 2011) –important for optical imaging of posterior ocular tissues–and produces a stable IOP elevation of ~85% over 6 weeks (Ito et al., 2016). Selection of the passive or active method of microbead deposition should primarily consider the desired magnitude and duration of IOP elevation.

Although it is a popular model, the laboratory use of the microbead model is hindered by variable outcomes, which in our experience is primarily due to inter-user variability in two procedural elements–intracameral microbead injection and IOP measurement, as discussed below.

1. *Intracameral microbead injection:* Both passive and active versions of the microbead model require delivery of microbeads into the anterior chamber via intracameral injection. Historically, this has required two well-trained experimenters working together to achieve successful and consistent intracameral injections: one to position the injector and one to administer the injection (Calkins et al., 2018). This process makes the procedure laborious and increases the potential for variability between end-users. These drawbacks are more severe in the magnetic microbead model due to its more complex and time-consuming protocol.

2. *IOP measurement.* Accurate, non-invasive, longitudinal measurement of IOP, typically performed by tonometry in rodents, is important in OHT models (Filippopoulos et al., 2006; Hu and Danias, 2018; Morris et al., 2006). Accurate and consistent measurement of IOP in mice is challenging, including in the microbead model of OHT (Hu and Danias, 2018), and depends on precise alignment of the tonometer with the center of the cornea and proper calibration and operation of the tonometer.[8] The TonoLab tonometer, which is specifically calibrated for rodents, has improved the accuracy of non-invasive IOP measurement in mice (Pease et al., 2011; Saeki et al., 2008). However, even with this device, successful and consistent alignment of the tonometer with the center of the cornea, while possible, is technically challenging in awake mice (Calkins et al., 2018). Sedation immobilizes the mouse and thus greatly facilitates proper alignment of the tonometer, but can artificially lower IOP in a time-dependent manner (Qiu et al., 2014; Tsuchiya et al., 2021). The window of time in which IOP is reliable under anesthetized conditions is variable and must be empirically determined for each laboratory. Thus, the methodology for IOP measurement is complex and requires considerable skill and experience.

Here, we outline an updated protocol for the microbead model of OHT that utilizes a novel, integrated platform for surgical procedures and hands-free IOP measurements. This protocol enables a single experimenter to carry out all procedures while improving consistency in microbead delivery and IOP measurements. We include details for the use of both magnetic and non-magnetic microbeads, as well as procedures for accurate IOP measurements under anesthesia. These updated protocols require custom manufacturing of equipment, thus, access to machining and 3D printing facilities is necessary. We note that the use of a manual injection apparatus does not require access to such manufacturing capabilities and that protocols for execution of the non-magnetic and

magnetic microbead models using a manual injection apparatus are described by Calkins et al., 2018 (Calkins et al., 2018) and Ito et al., 2016 (Ito et al., 2016). However, our experience is that custom manufacturing is well worthwhile to obtain better long-term results with the microbead model of OHT.

This protocol is intended to provide a comprehensive starting guide for the execution of the microbead model of OHT. If difficulties are experienced in establishing the model, hands-on training with an experienced lab is highly recommended. Variables such as micropipette preparation and injection angle can have a profound effect on the success of the model and are readily identified by observation and training.

## 3.2 Materials and Assembly

Appropriate sterilization protocols should be used throughout this protocol, including the utilization of single-use or sterilized instruments and aseptic preparation of solutions. The procedure below requires approval by an Institutional Animal Care and Use Committee and its practice should adhere to applicable animal welfare codes and regulations.

### *3.2.1 General*

1) Micropipette puller (see Note #1)
2) Microelectrode beveler (BV-10, Sutter Instruments)
3) (Optional) Coarse diamond abrasive plate (104C, Sutter Instruments)
4) Rebound tonometer and disposable probes (TONOLAB, iCare). We modified our tonometer, so that it can be actuated by a separate foot switch, thereby avoiding hand motion when acquiring IOP measurements.
5) Focal light source for surgery (dual gooseneck LED recommended)

6) Non-serrated, straight or curved forceps (approximately 2mm) for eye positioning. The use of curved vs. flat forceps is a matter of individual preference and comfort.
7) Magnetic Microbead Protocol only: 0.25" cubic N52 neodymium magnet connected to a thin stainless-steel Allen key.

### *3.2.2 Anesthesia and Animal Support*

1) A gas anesthesia system for use in mice, including an induction chamber and nose cone (see Note #2).
2) Animal temperature controller – low voltage (TCAT-2LV, Physiotemp; see Note #3)
3) Heat plate (HP-4M, Physiotemp; see Note #3)
4) Rectal temperature probe (RET-3, Physiotemp; see Note #3)

### *3.2.3 Integrated Surgical and IOP Platform*

1) CAD drawings for platform assembly (see Supplemental Material)
2) Threaded connecting rod (6516K121, McMaster-Carr)
3) Threaded connecting rod (6516K4, McMaster-Carr)
4) Round aluminum rod, ½” OD x 12” long (83048, K&S)
5) M3 x 50mm screws and compatible nuts
6) Manual rotation stage (Thorlabs, RP01)
7) Manual rotation stage (Thorlabs, RP03)
8) Linear stage (Newport, TSX-1D)
9) Optical breadboard plate (Newport, SA2-08x08)

10) Knob (McMaster-Carr, 6479K35)

11) Foot-long Aluminum 90-degree angle for part 2 (McMaster-Carr, 8982K145)

12) Aluminum slab for part 3 (McMaster-Carr, 1651T7, 6”x6”)

13) Aluminum disk for part 4 (McMaster-Carr, 1610T12, Ø 0.5”)

14) Stainless steel plate. All the components of the integrated surgical and IOP platform will be ultimately placed on this plate, which will serve as the base for the magnetic stands. Thus, plate dimensions should be chosen accordingly. Use a type of stainless steel with magnetic properties.

15) Velcro straps

16) Breadboard mounting feet (Newport, SA2-FT-70)

*3.2.4 Injection Apparatus*

1) Stereo microscope (see Note #4))

2) Syringe pump (Harvard Apparatus, PHD ULTRA 70-3006)

3) Foot switch for syringe pump (Harvard Apparatus, 702215)

4) Injection assembly (World Precision Instruments, MMP-KIT)

5) Gastight 25 µl syringe (Hamilton, 1702LT)

6) Manual micromanipulator (World Precision Instruments, M3301) with magnetic base

### *3.2.5 Consumable Materials*

1) Charcoal canisters (isoflurane waste container)

2) 4-inch thin-wall glass capillaries with filament (1.5 OD/1.12 ID)

3) 0.6ml Microcentrifuge tubes, autoclaved

4) 1.5ml Microcentrifuge tubes, autoclaved

5) Sterile vacuum filter units (250ml, pore size = 0.22µm) for sterilization of solutions

6) 5cc disposable syringe

### *3.2.6 Reagents*

1) 70% ethanol (for sterilization)

2) 95% $O_2$/5% $CO_2$-EM Compressed Gas (in cylinder)

3) Isoflurane

4) Mineral Oil, Light (NF/FCC)

5) Polystyrene Microspheres (see Note #5):

   a) Non-magnetic: 15µm (1 x $10^6$ beads/mL stock solution; ThermoFisher Cat#F8844). Store at 4° C.

   b) Magnetic: 1:1 mixture of 2 µm (1.2 x $10^{10}$ beads/mL) and 6 µm (4 x $10^8$ beads/mL) magnetic polystyrene microbeads with PEG-COOH surface groups (micromer-M, Micromod, Rostock, Germany). Store at room temperature.

6) Phosphate-buffered saline (PBS) without sodium azide

7) 1% tropicamide ophthalmic solution (dilation drops)

8) 0.5% proparacaine hydrochloride ophthalmic solution (anesthetic drops). Store at 4°C.

9) 0.5% moxifloxacin hydrochloride ophthalmic solution (antibiotic drops)

### *3.2.7 Anesthesia Apparatus Assembly*

1) Follow manufacturer's instructions for assembly of the anesthesia apparatus. Assembly occurs only once at initial setup of the equipment (Figure 3A,B).

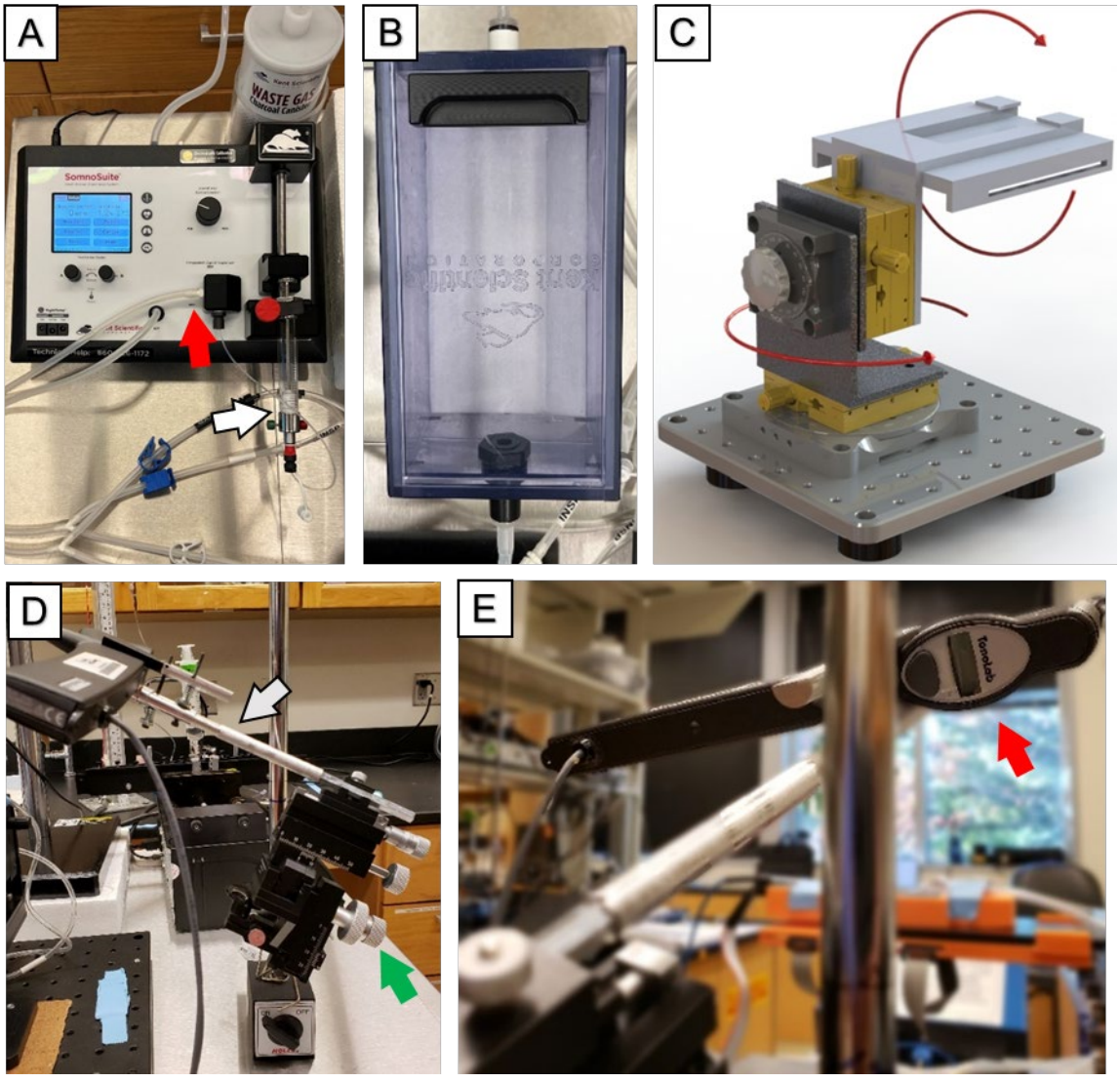

Figure 3. Anesthesia and Platform Assemblies. A. Photographs of SomnoSuite anesthesia system. The glass syringe (white arrow) is mounted on a syringe pump that delivers anesthetic liquid to the vaporizer. Red arrow indicates gas anesthetic outlet from the vaporizer to both the induction chamber and the nose cone. Color coded clips are used to redirect the gas. Waste is purged into a charcoal filter canister (top right corner of the photograph). B. Induction chamber. C. Custom-made surgical platform. Refer to the assembly files for complete instructions. This platform allows for linear movement in three-dimensions and rotation, with axes shown in the rendered image as red arrows. The heat plate can be slid into the groove on the white top surface. D,E. IOP measurement setup which includes TonoLab tonometer (red arrow), a micromanipulator (green arrow) and a custom-made mounting apparatus (white arrow).

### *3.2.8 Injection and Tonometry Apparatus Assembly*

The preparation of this equipment requires access to 3D printers (part 1) and machining facilities (parts 2-4). CAD files for parts 1-4 are provided in the supplementary materials. A commercial device was incorporated in the original prototype of our injection platform but is no longer available on the market. Therefore, we have re-designed the platform to include only parts that can be easily procured.

1) Assemble the machined parts according to the “assembly CAD file” provided in the supplementary materials (Figure 3**C**).

2) Fabricate the tonometer holder using the instructions in the assembly CAD file. Attach the tonometer to a micromanipulator using the tonometer holder (Figure 3D,E).

3) Secure the heat plate by sliding it into part 1 of the assembly and tape the nose cone for the anesthesia assembly to the heat plate (Figure 4A).

4) Wire the heat plate to the controller according to the manufacturer’s instructions (Figure 4B).

5) Secure the needle side of the injection assembly on a micromanipulator (Figure 4C,D).

6) Connect the opposite side of the injection assembly to the Hamilton syringe using a 3-way valve (Figure 4C,E). Mount the Hamilton syringe on the syringe pump (Figure 4C).

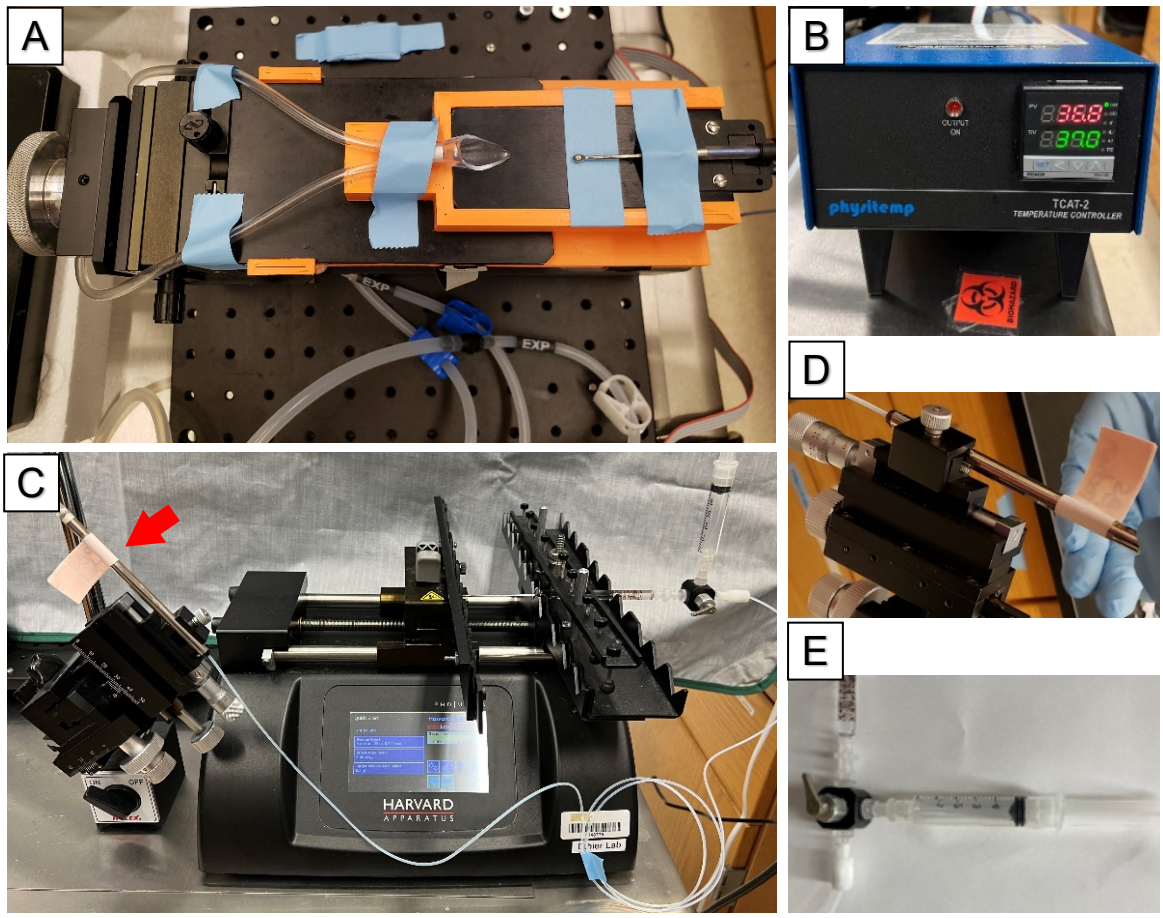


Figure 4. Injection Assembly. A. Photograph showing a heat plate (black) installed on the 3D printed platform of the surgical set up (orange). Nose cone (on the left) is taped to the platform. B. Animal temperature controller. C. Injection assembly and syringe pump. Black arrow indicates the 3-way valve connected to a 5 ml syringe filled with mineral oil on the top and a Hamilton microsyringe to the left. The remaining outlet from this valve is connected by tubing to the commercial injection assembly (red arrow). D. Closer view of the commercial injection apparatus in panel C (red arrow). E. Closer view of the 3-way valve in panel C (black arrow).

7) Place the stereomicroscope (if using) in a position that allows easy observation of the rotational platform.

### *3.2.9 Micropipette Preparation*

1) Use a glass micropipette puller to create micropipettes for microbead and saline injection (Figure 5A). Determine appropriate settings for your instruments (see Note #6)).

2) Insert a glass capillary into the holder and secure with screws. Press the “pull” button to heat the filament (Figure 5B).

3) When the glass electrode separates into two micropipettes, loosen screws and remove (Figure 5C).

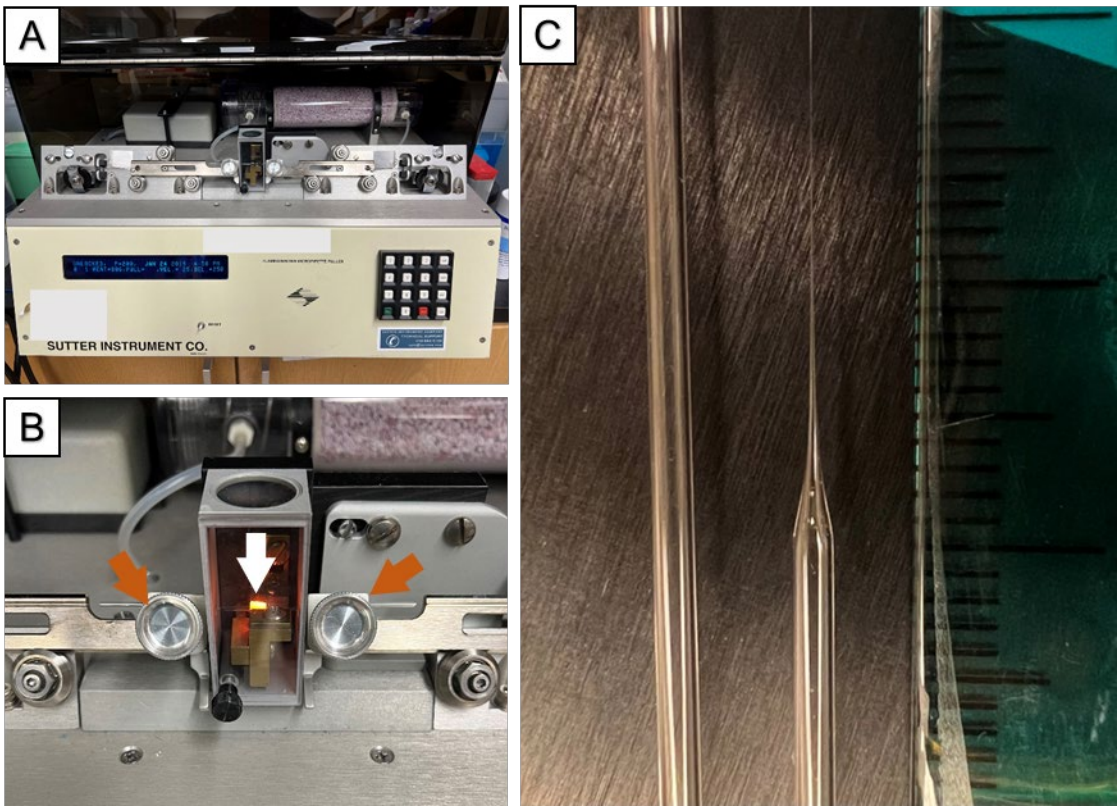


Figure 5. Production of Glass Micropipettes. A. Photograph of microelectrode puller. B. Photograph of a glass capillary secured in the puller. White arrow indicates location of the heating element. Red arrows show the micropipette clamped on both sides to the pulling arms. C. Photograph of the pulled (right) and original (left) micropipettes. Ruler subdivisions are in millimeters.

4) Tri-beveling of the micropipette tip increases the repeatability and efficiency of injections.

    a) Mount the coarse diamond abrasive plate on the microelectrode beveler's rotational platform, according to the manufacturer's instructions. Add a few drops of deionized water on the abrasive surface as lubricant.

    b) Use a pair of fine scissors with thin blades to score and break the tip of the micropipette (Figure 6A). The exact distance of the break point to the tip depends on the profile and taper length of the pulled micropipette but a final lumen diameter of ~100 µm is desired.

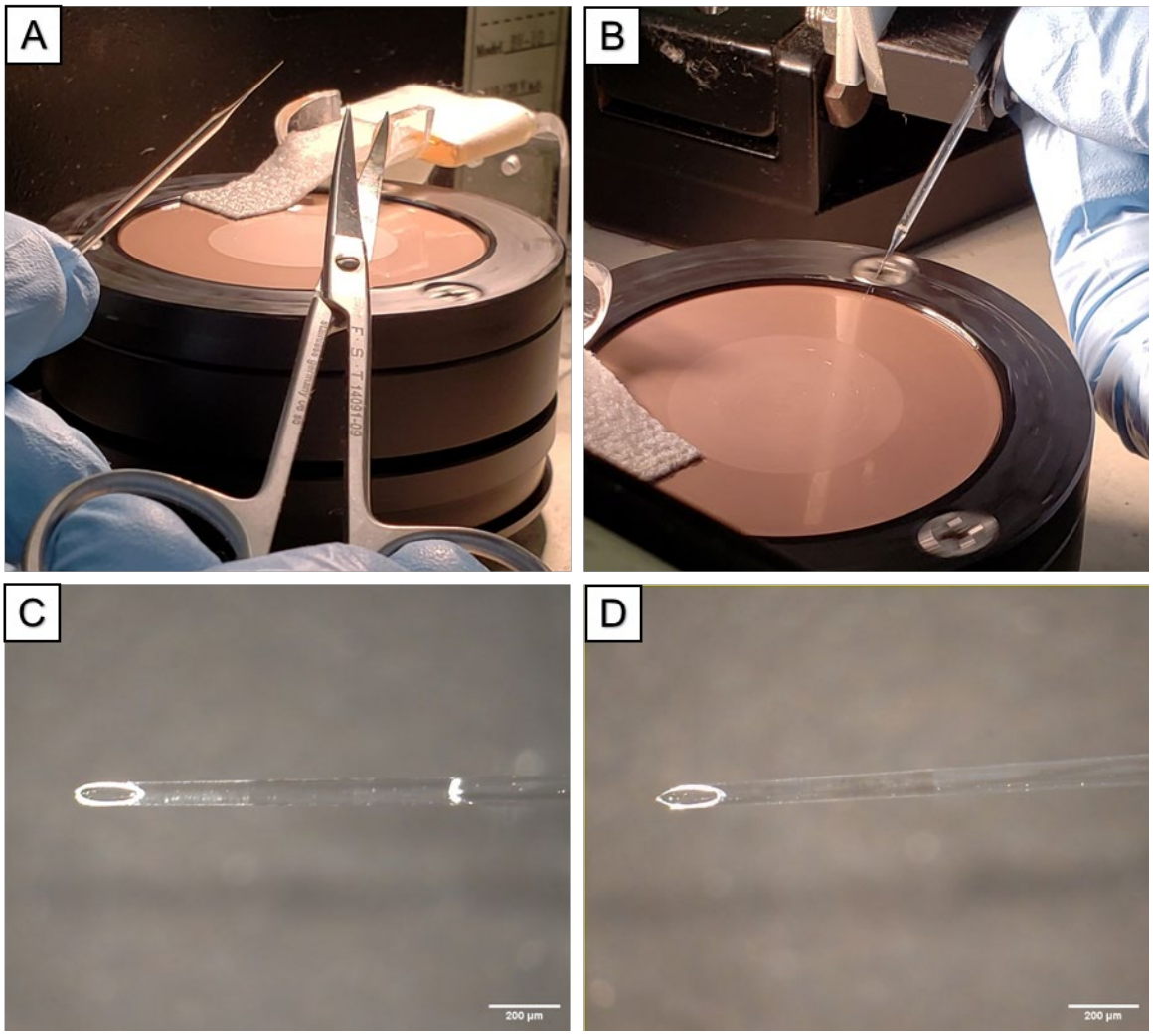


Figure 6. Micropipette Trimming. A. Photograph of a trimmed micropipette and the fine scissors used to break it. B. The beveling setup, including the diamond abrasive plate, the beveler rotational system, and the trimmed micropipette approaching the surface at 25° angle. C. A micropipette after beveling on the main side (part “b” of the tri-beveling approach). The appearance of elliptical cross-section signals the completion of this step. D. Micropipette after tri-beveling. The cross-sectional profile should be free of jagged surfaces and have a fine pointed tip.

c) Bring the micropipette tip in contact with the plate at 25 degrees. Allow for a smooth surface to develop (see Note #7**,** Figure 6B). Once the lumen shows an elliptical cross section visible under the microscope, the micropipette is ready for the next step (Figure 6**C**).

d) Axially rotate the micropipette by approximately 70 degrees to expose the side of the beveled surface to the abrasive plate. Once half of the rounded tip is ground down, return to the original position, and then rotate 70 degrees in the opposite direction. Grind down the glass until the rounded tip turns into a sharp pointed tip (see Note #8**,** Figure 6D).

*3.2.10 Reagent Preparation - Microbeads*

1) For polystyrene microbeads, proceed to step 3.

2) For ferromagnetic microbeads, sterilize by autoclaving (Gerberich et al., 2022) for 20 minutes at 121 °C and 3500 mbar pressure followed by rinsing 5 times using sterile HBSS (see Note #9).

3) Using aseptic technique, aliquot microbeads into a 0.6 ml microcentrifuge tube. Aliquot volume should be slightly more than the volume needed for total number of injections performed. Solution remaining in the aliquot at the end of the surgical day should be discarded.

4) Sterilize PBS using vacuum sterilization filter units. Sterile solution can be stored at 4° C for 1 month. Using aseptic technique, transfer 300 µl of sterilized PBS to a 0.6 ml microcentrifuge tube.

5) Place 1ml of 70% ethanol in a 1.5ml microcentrifuge tube for sterilization of micropipettes after insertion in the injection apparatus.

## 3.3 Methods

### *3.3.1 IOP Measurements*

Baseline measurements of IOP should be obtained for all animals being studied (including naïve controls). To obtain reliable, hands-free IOP measurements under anesthesia**:**

1) Weigh the animal and input the corresponding value into the SomnoSuite anesthesia device. The device will automatically set the flow rates based on the animal weight (see Note #10)).

2) Position the tonometer horizontally to avoid any component of gravitational force affecting the measurements (the device will give an error otherwise). Ensure the working range of the micromanipulator allows the tonometer to be suitably placed, i.e., there is sufficient reach and adjustment over the animal's head when the animal is placed in the nose cone (Figure 7A).

3) Place the animal in the induction chamber and set 2% isoflurane to be delivered at 500 ml/min to the chamber. Monitor the animal closely and, once it is immobile, check for a loss of righting reflex by rotating it to the supine position (see Note #11).

4) Run "flush" to clear excess anesthetic from the tubing. Re-direct the flow to the nose cone and run the pre-programmed settings for the delivery of 1% isoflurane (see Note #12)). Take the animal out of the induction chamber and place over the heat pad with the head affixed to the nose cone. Secure the head with the velcro straps (see Note #13)).

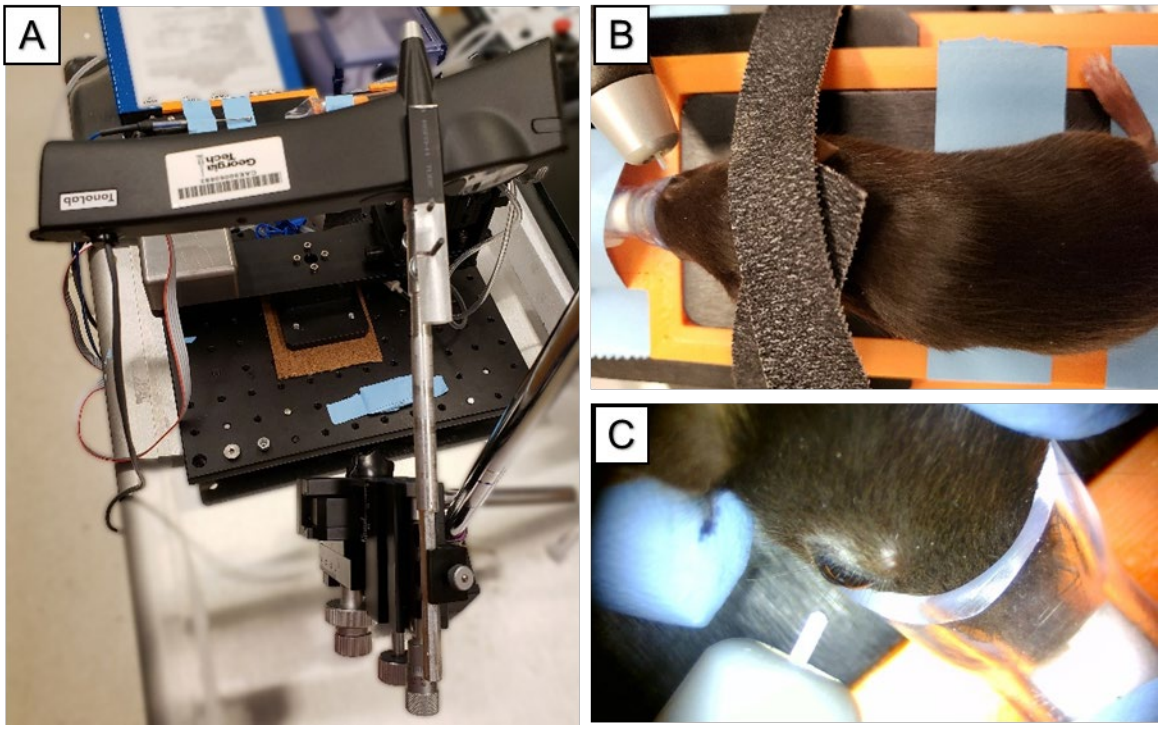


Figure 7. IOP Measurement. A. Horizontal orientation of the tonometer in the tonometer holder. B,C. Alignment of the tonometer probe perpendicular to the center of the cornea. Velcro straps attached to the surgical platform (hands-free; B) or a gentle, manual hold (C) may be used to immobilize the head in the desired position.

5) Position the tonometer tip perpendicular to the center of the cornea. Check from both the top and the side to ensure proper positioning, since the readings are sensitive to tip misplacement/misalignment (see Note #14, Figure 7B,C)

6) Read IOP (see Notes #14),-#16).

7) Quickly rotate the stage and repeat for the contralateral eye, if desired.

8) Turn off the anesthesia, unstrap the animal and place over a heated pad to recover.

### *3.3.2 Intracameral Injections*

The integrated surgical and IOP platform enables a single experimenter to conduct intracameral microbead injections by utilizing foot controls.

3.3.2.1 Injection Procedure for Non-magnetic Microbeads

1) Insert and tighten the prepared micropipette into the injection assembly mounted on the micromanipulator (see Note #17; Figure 8A).

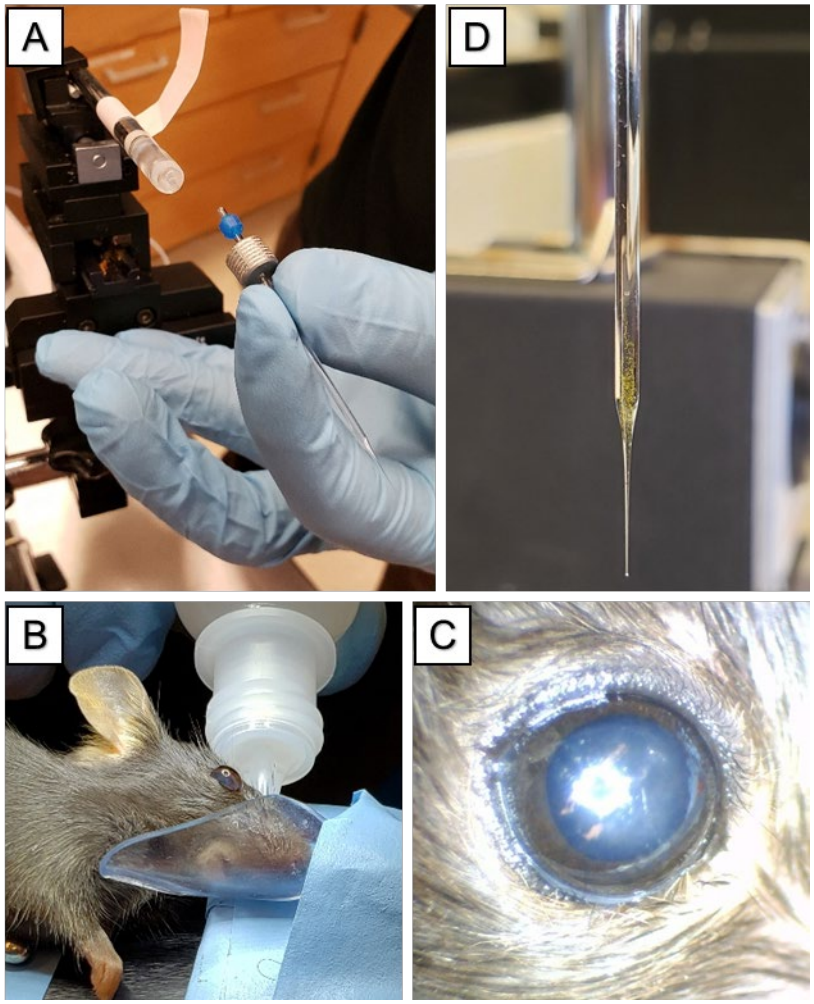


Figure 8. Pre-injection Preparations. A. Preparing the micropipette to be loaded into the injection apparatus, which is mounted on a micromanipulator. B. Proper placement of the mouse on the surgical platform. A drop of topical anesthetic is applied to the eye. C. The desired pupil dilation is achieved after application of 1% tropicamide. D. The desired volume of microbeads (yellow) loaded in the micropipette after rinsing the inner lumen with sterile PBS. White arrow indicates the meniscus formed at the interface between the mineral oil and microbead solution.

2) Fill the micropipette with mineral oil by depressing the plunger of the 5cc syringe attached to the side port of the 3-way valve (Figure 4C). Ensure no bubbles are present

throughout the line and that oil beads form at the tip of the micropipette. Use a Kimwipe to remove excess mineral oil from the tip.

3) Apply one drop of 1% tropicamide ophthalmic solution to each eye (see Notes #18)8 and #19).

4) Place the animal in the induction chamber and deliver 2.5% isoflurane via the anesthesia system until righting reflex is lost (see Note #20).

5) Divert isoflurane flow to the nose cone. Transfer the animal to the heat pad and affix the nose cone. Orient the animal on its side with the cornea to be injected facing up (Figure 8B). Secure the animal with Velcro straps.

6) Set syringe pump to zero (zero out) and sterilize the tip of the micropipette by submerging it in the microcentrifuge tube filled with 70% ETOH.

7) For bilateral microbead injections, wet the internal surface of the micropipette by submerging the tip of the micropipette in the microcentrifuge tube of sterile saline. Set the automatic syringe pump to load 2µl of sterile saline into the micropipette (see Notes #21 and #22). Eject and discard 1.5µl of the sterile saline from the micropipette.

8) Check dilation (Figure 8C) and reapply 1% tropicamide ophthalmic solution, if necessary (see Note #23).

9) Set the automatic syringe pump to the desired injection volume at a flow rate of 18µl/min. Load the solution for injection (sterile saline or microbeads), using the desired injection volume plus a volume of 0.5ul (see Note #24). Keep the tip of the micropipette submerged in the solution until the proper volume of solution is loaded.

Check the location of the meniscus where the injectable solution interfaces with the mineral oil to ensure the proper volume is loaded (Figure 8D).

10) Apply local anesthesia (0.5% proparacaine hydrochloride ophthalmic solution; one drop) directly to the eye and wait for 1 minute.

11) Proptose the eye with curved or flat-edge forceps (see Note #24; Figure 9A).

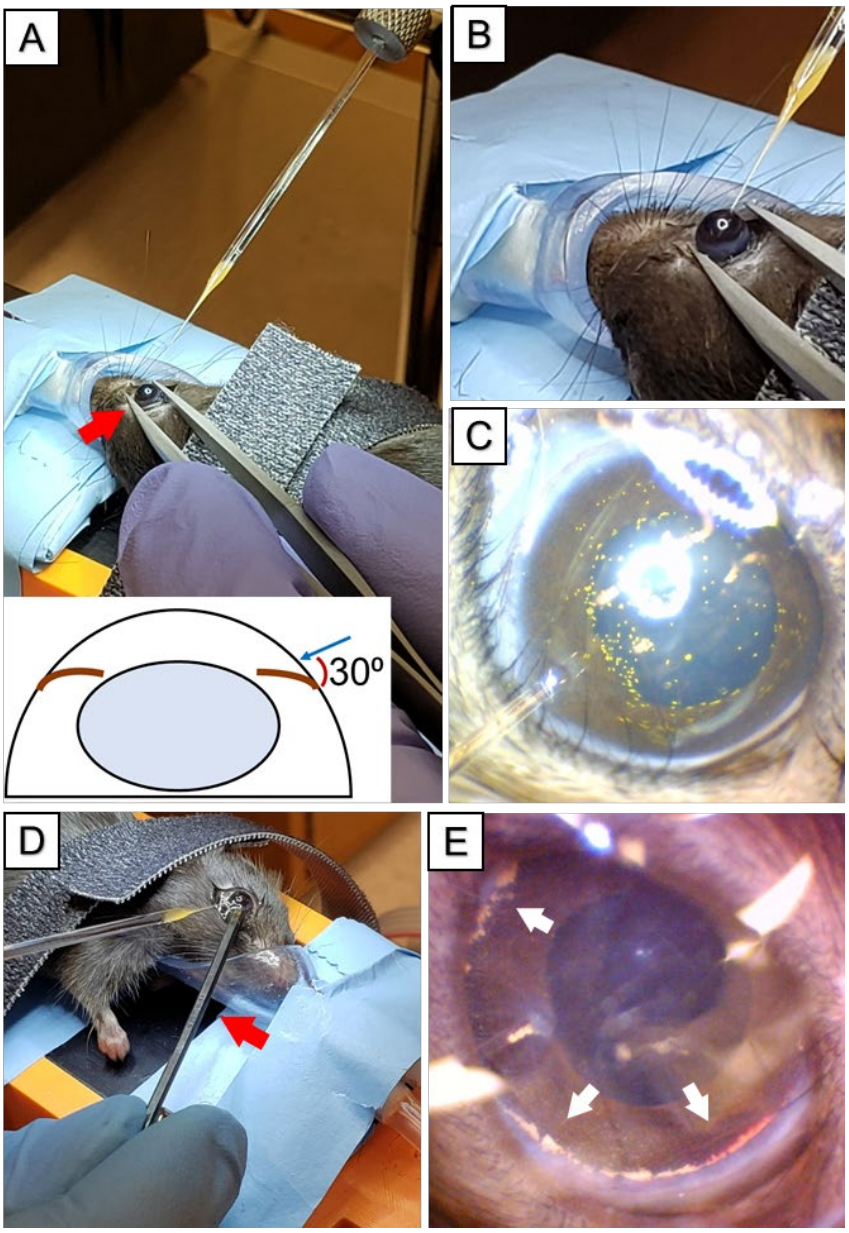


Figure 9. Microbead Injection. A. Photograph of eye being proptosed with forceps. Arrow indicates the “brace” position generated by the back arm of the forceps. Inset: Schematic illustrating the orientation of the micropipette with respect to the limbus. B. Photograph of the first 5-7 seconds of microbead injection. The eye is braced by forceps until the desired volume of microbead solution is delivered. Note that the micropipette is inserted in the cornea at an ~ 30º angle from the limbus. C. Photograph of the second 10-15 seconds of microbead injection. Forceps are removed and the micropipette remains until microbeads disperse. D. Magnetic apparatus (arrow) pointing at the limbus for delivery of magnetic microbeads. The experimenter encircles the limbus with the magnet in a fashion described in the main text, for a circumferentially uniform delivery. E. Accumulation of magnetic microbeads at the angle (arrows) upon the completion of delivery. Micropipette is kept

inside the anterior chamber until the microbeads are stabilized in place. Procedures in panels A-C incorporate non-magnetic microbeads while panels D-E are magnetic.

12) With the eye stabilized by the forceps, align the tip of the micropipette with the far edge of the dilated iris (Figure 9A,B). A 30º angle of approach with respect to the limbus is typically successful for smooth penetration of the cornea and clearance of the iris (Figure 9B). The five-axes design of this platform (linear XYZ movement and two rotational axes, Figure 3C) allows for free movement of the surgical bed in 3D space to achieve proper alignment of the eye with the micropipette tip while the latter remains stationary.

13) While stabilizing the eye with the forceps (see Note #25), advance the micropipette in a continuous motion until the cornea is punctured (see Note #26).

14) With the eye still proptosed, use the foot pedal control the automatic syringe pump to inject the desired volume. The eye should remain proptosed and gently supported by the forceps until the desired injection volume is delivered into the anterior chamber (see Notes #27 and #28).

15) With the micropipette still in the cornea, wait another 15-20 seconds to ensure dispersion of the microbeads in the anterior chamber (see Note #29)9; Figure 9C).

16) Slowly withdraw the micropipette from the cornea. Stabilize the eye using forceps as a brace to prevent the eye from traveling with the micropipette, applying gentle resistance in the opposite direction to that employed during corneal puncture.

17) Apply one drop of 0.5% proparacaine hydrochloride ophthalmic solution and one drop of 0.5% moxifloxacin hydrochloride ophthalmic solution (antibiotic) directly to the cornea.

18) If performing bilateral injections, use the rotational platform to flip the animal and repeat steps 8 – 17.

19) Upon completion of all injections, turn off anesthesia. Remove the animal from the nose cone and place on a heated pad and then in a clean cage for recovery. With isoflurane anesthesia, the animal will awake within minutes.

20) Monitor the animal for signs of distress, as per the approved IACUC protocol.

3.3.2.2 Injection Procedure for Magnetic Microbeads

The procedure for magnetic microbead injection is identical to that of non-magnetic microbeads, with the following exceptions:

Step # 9: Set the syringe pump to deliver an injection volume of 0.4 µl at 2.4 µl /min.

Step #14: Divide the eye into imaginary quadrants. Hold the magnetic steering apparatus (a permanent magnet attached to a thin stainless-steel Allen key) over the cornea in the targeted quadrant (see Note #30, Figure 9D). Press the foot pedal to inject 0.4 µl of the microbeads. “Collect” the injected microbeads on the cornea using the magnetic steering apparatus. Slowly drag the microbeads to the irideocorneal angle and distribute them uniformly to cover the entire circumference of the quadrant (Figure 9E). Repeat for each quadrant (total injection volume equals 1.6 µl).

*3.3.3 Monitoring and Model Maintenance*

1) The cornea may temporary become cloudy 24-48 hours after surgery. Beyond 48 hours, there should be no visible difference in the cornea between saline- and microbead-injected eyes. However, microbeads will remain visible in the anterior chamber of microbead-injected animals (Figure 10).

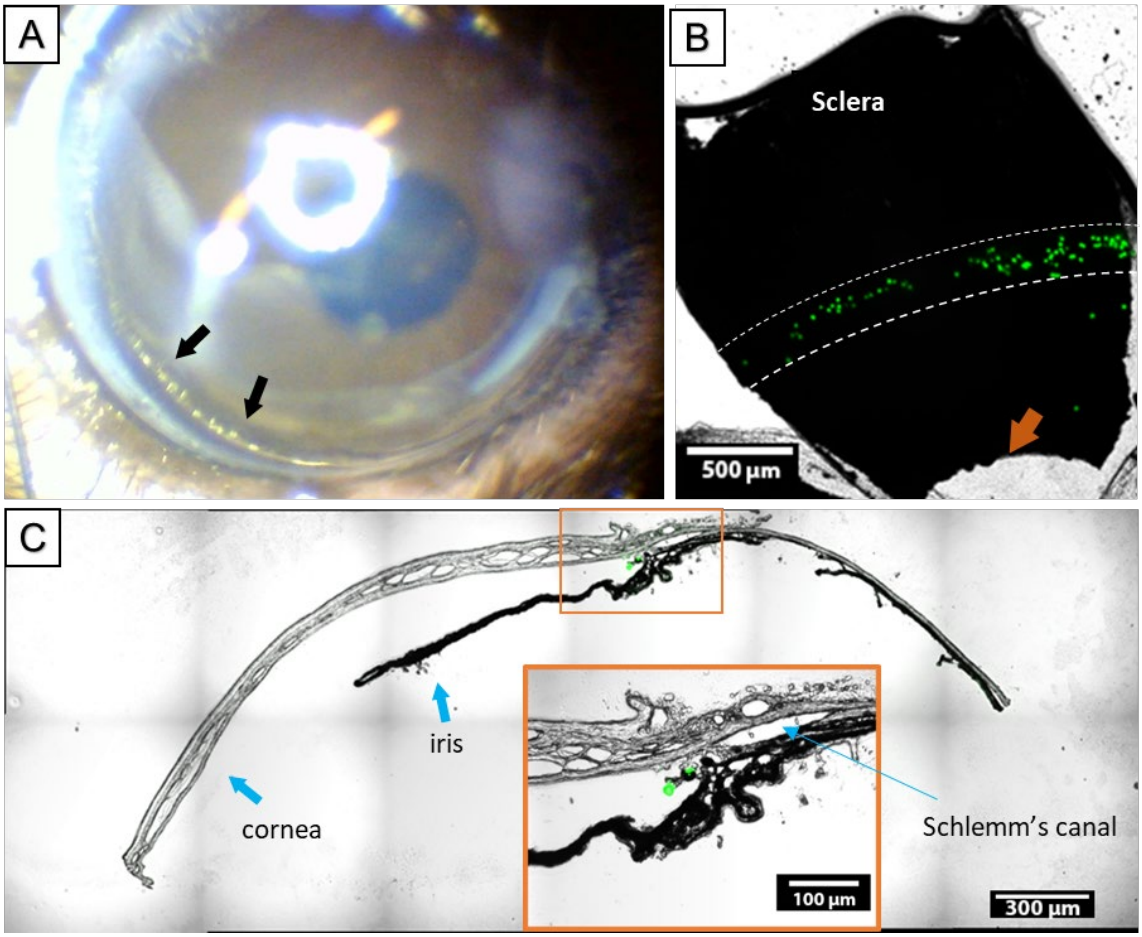


Figure 10. Post-op Evaluation of Microbead Delivery. A. Yellow non-magnetic microbeads are deposited at the angle (arrows). Image is taken using a surgical microscope 24 h after surgery. B. Fluorescent image of the non-magnetic microbeads located at the limbus. Eye was enucleated 24 h after surgery, fixed in 10% formalin, and four incisions were made resulting in an anterior segment flat mount. Fluorescent image is merged with a light micrograph for one quadrant; green pseudocolor shows the fluorescent microbeads. Red arrow indicates the pupillary margin and dashed lines show the putative limbal region. C. Cross-sectional (sagittal) view of the angle 24 h after non-magnetic microbead (green fluorescence) injection. Insert outlined by red box shows a magnified view of the angle.

2) To assess the efficacy of microbead injections and to monitor model progression, IOP measurements should be taken for at least 3 consecutive days following intracameral injection followed by 1-2 times per week for the remainder of the experiment (see Notes #31 and #32). IOP measurements should be taken as outlined in section 3.1.

3) The duration of IOP elevation can be extended by re-injection prior to the loss of ocular hypertension following the same procedures above (see Note #33).

### 3.4 Notes

1) A horizontal (i.e., P-97, Sutter Instruments) or vertical (i.e., PC-100, Narishige) electrode puller may be utilized.

2) Any gas anesthesia system with mouse nose cone adaptors is acceptable. Two systems that are compatible with microbead injection are:

   - Low-flow anesthesia system for mice including induction chamber and nose cones (SomnoSuite Starter Kit for Mice, Kent Scientific)

   - V-1 Tabletop Laboratory Animal Anesthesia System with an accessory kit containing a ten-foot oxygen hose, flowmeter, oxygen flush assembly, vaporizer, breathing circuit, chamber, nosecones, waste gas evacuation tubing and two VaporGuard filters. (901806; VetEquip)

3) A variety of materials, devices, and approaches are available to maintain core body temperature, monitor depth of anesthesia, and track vital signs. Any devices employed must allow for unobstructed access to eyes. All IACUC guidelines and standard procedures for animal monitoring during gas anesthesia must be followed.

4) In lieu of a stereoscope, the experimenter may wear a headband mount magnifier, such as OptiVISOR Headband Magnifier, 2X Magnification (Donegan, DA-4) or 3.5x Magnification, Optical Glass, Rectangular Magnifier-Headband Mount (Made in the USA, DA-10).

5) Frequently agitate the microbead solution by tapping to prevent aggregation and sticking, particularly just before use. Alternatively, the microbead sample can be vortexed prior to injection.

6) Protocols for pulling micropipettes should be optimized for the specific instrument utilized, as variation between pullers (i.e., position and type of filament) can influence settings. Refer to the manufacturer's directions for settings. As a guide, example settings from a horizontal pipette puller and a vertical pipette puller are provided below:

   a) P-97 Model from Sutter Instruments (shorter taper)

      P = 500 units

      Heat = 490 units

      Pull = 30 units

      Velocity = 120 units

      Time = 200 units

   b) P-97 Model from Sutter Instruments (longer taper)

      P = 200 units

      Heat = 806 units

      Pull = 0 units

      Velocity = 25 units

      Delay = 250 units

   c) PC-100 Model from Narishige

      P = 500 units

      Heat = 650 units

Pull = 30 units

Velocity = 120 units

Time = 200 units

7) For the BV-10 beveling system, Sutter Instruments recommends bubble formation over the abrasive plate as the best method for assessing progression of the beveling surface. However, we have found that monitoring the noise caused by grinding the glass to be an easier and more reliable technique. When the micropipette contacts the abrasive plate, noise is initially heard but slowly fades as the beveled surface smoothens.

8) It is recommended to increase the angle between the micropipette and the abrasive plate to 45° when sharpening the sides to engage only the very tip of the micropipette and keep the rest of the profile intact. Grind the sides just enough so that a pointed tip is achieved. Over-grinding can result in jagged surfaces which can prevent a clean puncture through the cornea.

9) When using magnetic microbeads, hold a strong magnet close to the microbead tube to avoid loss of beads during the rinse steps.

10) If the anesthesia equipment does not auto-regulate isoflurane flow, the optimal flow rate must be determined empirically based on depth of anesthesia and latency to anesthesia. If the animal shows sign of agonal breathing, increasing the flow rate may help alleviate the symptom.

11) The loss of righting reflex is an indicator of the start of unconsciousness or light anesthesia. With progression of anesthesia, the episcleral venous pressure drops, which leads to a decrease in the IOP. Therefore, the animal should be transferred to

the nose cone immediately after the loss of righting reflex and the measurements should be taken as quickly as possible. In our experience, the average measurement time (from the end of induction to the end of measurements) for both eyes is 2-3 minutes.

12) If isoflurane/$O_2$ mixing is performed manually, the optimal mix and duration for anesthesia induction may need to be optimized. The guidelines provided in this protocol for both induction and maintenance of anesthesia can be utilized to determine optimal mixing for manually regulated anesthesia.

13) The mouse's head should be immobilized, but Velcro straps should not be over-tightened. Excess force applied by the Velcro straps can artificially affect the IOP. The experimenter can alternatively choose to hold the animal's head with one hand. While this hand-grip method increases the control over the orientation of the center of the cornea with respect to the tonometer probe tip, caution must be taken not to apply excessive force which may result in an artificial spike in the IOP.

14) Proper maintenance of the TonoLab tonometer is critical for accurate IOP measurement. The instrument must be routinely cleaned, and probes replaced, as specified in the operating manual.

15) The TonoLab tonometer (iCare) is programmed to provide a final IOP measurement after 6 rebound readings. A long beep signals calculation of the "final" IOP measurement, which is an average of 4 rebound repetitions with the highest and lowest readings omitted. If the user prefers to record each IOP measurement and manually calculate the average IOP, it is important to note that only the IOP measurement from the first rebound (e.g. reading "1.15" on the display) is a pure measurement. IOP measurements displayed for rebounds 2-5 are a running average

based on the current reading and individual readings from the previous rebound(s). For example, the IOP measurement for rebound #3 (e.g. reading “3. 16” on the display) is an average of the individual measurements for rebounds 1, 2, and 3. To record only individual measurements, the IOP measurement displayed for reading 1. 15 should be recorded after the first rebound and the device cleared (00 on the display) for repeated measurement. For additional information and support, refer to the Tonolab User Manual (https://tonovet.com/products/icare-lab/lab-brochure/).

16) IOP in mice fluctuates diurnally (Aihara et al., 2003; Savinova et al., 2001). To reduce variability and ensure accurate, longitudinal assessment of IOP, it is critical that all IOP measurements be conducted at a specific time of the day within a limited time window, usually taken as 2 hours. Also, users should be alert to the possibility of IOP spikes after injection (see note #32).

17) Micropipettes are prone to breakage and become dull with repeated use. Use one micropipette per animal to reduce the risk of ocular injury and prevent contamination between animals.

18) To deliver eye drops to an awake mouse, scruff the mouse with your non-dominant hand, as you would for delivery of an intraperitoneal injection. Hold the animal upright and deliver the eye drop with your dominant hand, tilting the animal slightly to the left or right.

19) If performing injections in multiple animals on a single day, procedure times can be shortened by dilating several mice simultaneously. Covering the housing cage to darken the environment will also hasten dilation after application of the dilation drops.

20) Based on the depth of anesthesia required, a higher percentage (2.5%) of isoflurane anesthetic is utilized for intracameral injection than for IOP measurements (2.0%).

21) When performing bilateral saline injections, it is not necessary to pre-wet the micropipette. Load 0.5ul more than the desired injection volume of sterile saline and proceed with intracameral injection of the sterile saline.

22) When performing unilateral microbead and saline injections in a single animal, the saline should be injected first to avoid contamination of saline injections with microbeads. It is also not necessary to pre-wet the micropipette, as the saline injection will serve this purpose.

23) Intracameral injection with insufficient dilation can lead to iris injury and intraocular bleeding. Sufficient dilation is achieved when approximately 75% or more of the anterior chamber is free of iris.

24) Volumes anywhere from 1-4µl of microbeads have been utilized for this model (Chen et al., 2011; Cone et al., 2010; Frankfort et al., 2013; Sappington et al., 2010). The most common injection volume is 1.5µl.

25) During proptosis and stabilization, forceps should never squeeze the eye from both directions, which can cause ocular injury and impact aqueous fluid dynamics. Proptosis is achieved by applying slight, downward pressure to the eyelids on either side of the eye. Stabilization of the eye against rotation during cannulation is achieved by slight inward pressure on the back arm of the forceps, directly opposite the micropipette.

26) Advancement of the micropipette should be slow and steady. Stopping or intermittent motions, particularly at the point of puncture, can cause breakage of the micropipette

or corneal abrasion. Tri-beveling of micropipettes substantially improves ease of corneal puncture.

27) Ensure that the entire volume of microbeads is delivered prior to retraction of the micropipette. The microbead solution is a suspension, which often requires additional time to fully exit the micropipette after it is dispensed by the syringe pump.

28) If a clog of the micropipette is observed or suspected, the eye can be very subtly shifted (not squeezed) with the forceps to promote flow of the solution. If this is unsuccessful, the micropipette should be withdrawn from the eye and the surgery terminated. Reinjection can be attempted when anterior chamber volume returns to normal, typically 24-36 hours later.

29) Non-magnetic microbeads should disperse throughout the anterior chamber and begin collecting in the iridocorneal angle. If microbeads remain near the injection site for longer than 30 seconds, ensure that forceps are not applying pressure to eye, which can impede aqueous humor dynamics.

30) The magnetic steering apparatus provides a focused magnetic field for directed delivery of microbeads to the outflow pathway, which reduces off-target delivery. The strength of the magnetic force can be altered by changing the distance between the magnet and the tip of the Allen key. Ideally, the magnetic force should be enough to prevent the microbeads from falling onto the lens or the iris, but not so strong as to cause microbead clump formation.

31) To ensure proper sealing of the cornea and prevent corneal injury, wait 24 hours between intracameral injections and IOP measurements.

32) Intracameral injection of either microbeads or saline results in substantial changes in fluid volume of the anterior chamber. This is true for successful injections and for those resulting in significant efflux of aqueous humor, i.e. corneal puncture without solution delivery. These changes in anterior chamber volume can result in either a substantial increase or decrease in IOP in the first 24-36 hours after injections. Additionally, a rat model of ocular hypertension has previously been shown to experience significantly higher elevation in dark phase IOP as compared to the light phase. This phenomenon has been associated with the decrease in outflow facility in this hypertensive model which exacerbates the effect of increased aqueous humor formation rate during dark phase on IOP elevation (Jia et al., 2000).

33) Subsequent injections should puncture the cornea in a different area than the original injection. Corneal wound healing from a prior injection as well as subsequent IOP elevations will increase corneal stiffness, thereby making corneal puncture more difficult.

# CHAPTER 4. IMPROVED MAGNETIC DELIVERY OF CELLS TO THE TRABECULAR MESHWORK IN MICE

This chapter is adapted from a published journal article in *Experimental Eye Research*:

M. Reza Bahranifard, Jessica Chan, Marybeth Yonk, A. Thomas Read, Shreya R. Kuturu, Stanislav Y. Emelianov, Markus H. Kuehn, C. Ross Ethier (2023). “Improved magnetic delivery of cells to the trabecular meshwork in mice.” *Experimental eye research*, *234*, 109602.

* Some figures are repositioned (without changing content) in this chapter compared to the original paper for consistency across the dissertation. Additionally, the article is divided into various sections for improved navigation.

* Appendix B includes theoretical calculations of forces applied to injected cells, supplementary to this chapter.

## 4.1 Abstract

Glaucoma is the leading cause of irreversible blindness worldwide and its most prevalent subtype is primary open angle glaucoma (POAG). One pathological change in POAG is loss of cells in the trabecular meshwork (TM), which is thought to contribute to ocular hypertension and has thus motivated development of cell-based therapies to refunctionalize the TM. TM cell therapy has shown promise in intraocular pressure (IOP) control, but existing cell delivery techniques suffer from poor delivery efficiency. We employed a novel magnetic delivery technique to reduce the unwanted side effects of off-target cell delivery. Mesenchymal stem cells (MSCs) were labeled with superparamagnetic iron oxide nanoparticles (SPIONs) and after intracameral injection

were magnetically steered towards the TM using a focused magnetic apparatus ("point magnet"). This technique delivered the cells significantly closer to the TM at higher quantities and with more circumferential uniformity compared to either unlabeled cells or those delivered using a "ring magnet" technique. We conclude that our point magnet cell delivery technique can improve the efficiency of TM cell therapy and in doing so, potentially increase the therapeutic benefits and lower the risk of complications such as tumorigenicity and immunogenicity.

*Keywords:* Primary open angle glaucoma, trabecular meshwork, cell therapy, IOP, magnetic cell delivery, cell delivery efficiency

## 4.2 Introduction

With nearly 80 million cases worldwide, glaucoma is the leading cause of irreversible blindness. The most common subtype of the disease is primary open angle glaucoma (POAG) which is associated with an elevated intraocular pressure (IOP). IOP is governed by the rate of aqueous humor (AH) production and the dynamics of its subsequent drainage through the outflow pathways. A key component of the conventional outflow pathway, the main drainage route for AH, is the trabecular meshwork (TM) which undergoes significant changes in POAG, including a loss of cellularity (Alvarado et al., 1984; Coulon et al., 2022; Gong and Swain, 2016b). There has thus been great interest in recellularization and refunctionalization of the TM as a potential long-term treatment for ocular hypertension associated with POAG (Xiong et al., 2021; Yun et al., 2018; Zhu et al., 2017, 2016). To date, such work is at the pre-clinical stage and has been carried out by intracameral injection of stem cells into various glaucoma models.

Mice are useful model organisms for studying ocular hypertension, yet only a few reports exist on TM cell therapy in mice. Zhu et al. delivered iPSC-TM cells into the eyes of Tg-

MYOC$^{Y437H}$ mice and reported a marked decrease in IOP and an increase in outflow facility for up to 12 weeks after injection as compared to saline-injected (sham) controls. The treatment also increased TM cellularity through promoting the proliferation of endogenous cells (Zhu et al., 2017, 2016). Similarly, Du and colleagues suggested that delivering TM stem cells into Tg-MYOC$^{Y437H}$ mice led to a reduction in IOP, an increase in outflow facility, improved TM structure, increased TM cellularity and neuroprotection, as compared to the sham control eyes (Xiong et al., 2021; Yun et al., 2018).

Despite the promise of TM cell therapy, there is much room for improvement, specifically in the quality of cell delivery. All the studies mentioned above rely on hydrodynamic forces generated by the flow of AH to passively carry injected cells, resulting in only 8% of the cells being delivered to the relative proximity of the TM (Wang et al., 2022). Off-target delivery limits the therapeutic potential of the treatment, requiring more cells to be injected which in turn increases the risk of tumorigenicity and immunogenicity (Coulon et al., 2022; Zhou et al., 2020). A further concern arises when considering the cells that do reach the TM: due to the segmental nature of AH outflow in the conventional outflow pathway (Chang et al., 2014b), passively delivered cells will be spatially limited to only a part of the TM filtration area. Magnetic cell steering has previously been proposed to overcome these shortcomings (Snider et al., 2018). In mice in particular, Wang et al. labeled iPSC-TMs with magnetic nanoparticles and steered them towards the TM under the forces generated by a ring magnet. While they report a 4-fold increase in the proportion of cells delivered in proximity to TM, still about two-third of the cells were delivered off-target (Wang et al., 2022).

In this study we introduce a new delivery technique that uses a magnetic apparatus with a focused magnetic field (“point magnet”). We compare the performance of this technique with the previously used “no magnet” and “ring magnet” methods discussed above,

focusing on the circumferential uniformity of cell delivery and delivery specificity to the TM region.

### 4.3 Methods

Human adipose-derived mesenchymal stem cells (MSCs) were purchased commercially (Lonza Bioscience, Walkersville, MD) and maintained in α-MEM supplemented by 10% FBS and 1% penicillin and streptomycin and 2 mM L-glutamine at 37° C and 5% $CO_2$. Cells were passaged by treating with 0.05% trypsin (25-053-CI, Corning Inc., Corning, NY) and seeding at 5000 cells/$cm^2$ in cell culture flasks. MSCs at passages 5 or 6 and 80% confluency were magnetically labeled by incubation overnight with 50 µl of 150 nm amine-coated superparamgnetic iron oxide nanoparticles (SPIONs; SA0150, Ocean NanoTech, San Diego, CA; 5 mg/ml stock solution) in a T-25 culture flask. Successful labeling was confirmed by light microscopy in a preliminary study. After incubation, we trypsinized the cells for 5 minutes, followed by addition of cell culture media and centrifugation at 2100 g for 5 min. The cells were then resuspended in PBS and were labeled with 5 µM carboxyfluorescein succinimidyl ester (CFSE) to allow fluorescent tracking in the eye (65-0850-84, eBioscience, San Diego, CA). The cell solution was then transferred to a 1.5 ml tube (Figure 11A, left) and a 0.25” cubic N52 neodymium magnet was placed on the side of the tube, which resulted in the formation of a cell pellet adjacent to the magnet within seconds (Figure 11A, center). To ensure all injected cells were magnetized, any cells not in the pellet were then removed by aspirating the supernatant. The cell pellet was resuspended in PBS to a final concentration of 1k cells/µl, since higher concentrations resulted in cell clumping inside the injection needle and inferior adhesion to the TM after delivery.

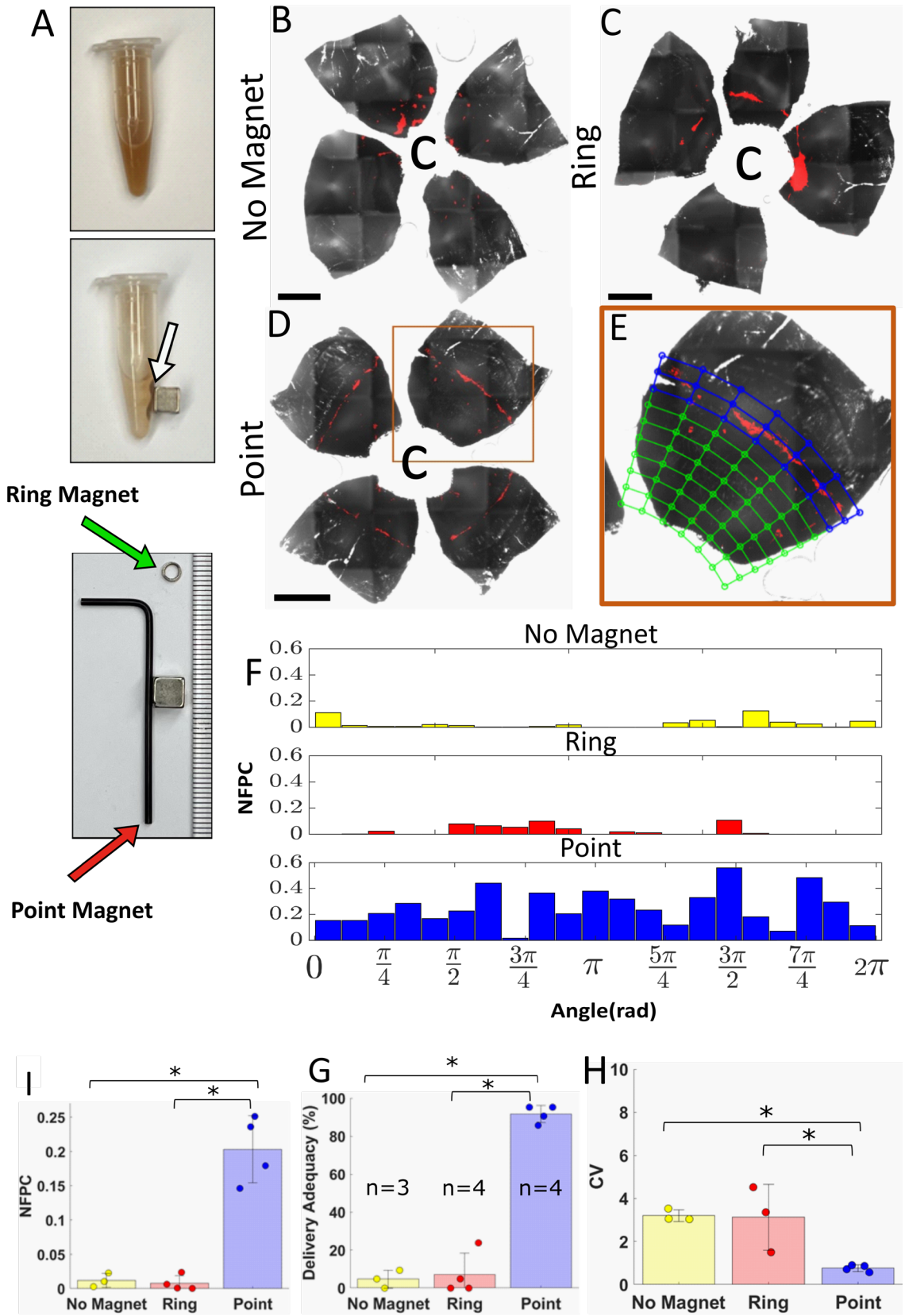
A
B
C
No Magnet
Ring
C
C
D
E
Point
C
Ring Magnet
Point Magnet
No Magnet
F
Ring
Point
NFPC
0.6
0.4
0.2
0
0
π/4
π/2
3π/4
π
5π/4
3π/2
7π/4
2π
Angle(rad)
I
G
H
NFPC
Delivery Adequacy (%)
CV
n=3
n=4
n=4
No Magnet
Ring
Point
*

Figure 11. Uniformity and specificity of cell delivery to the TM assessed from en face images. A) Preparatory steps, including MSC labeling with SPIONs (left), isolation of sufficiently magnetized cells with a magnet (center; white arrow indicates the cell pellet), and the magnets used for different delivery methods (right). B-D) Representative en face images of the delivered cells (red) using different methods. “C” marks cornea. E) A representative quadrant (zoomed region marked by orange box in panel D) subdivided both radially and angularly (green and blue meshes). Scale bars show 1 mm. Blue subregions show the region of interest (ROI) at the limbus. F) Representative plots of circumferential cell distributions using different delivery methods. The “normalized fluorescent pixel count” (NFPC) is calculated from the ROI in panel E. Note that each plot belongs to an individual eye. G-H) Metrics of circumferential delivery uniformity for each method, as described in text. A higher Delivery Adequacy (panel G) and a lower Coefficient of Variation (CV; panel H) correspond to a more uniform circumferential delivery of cells. I) Delivery specificity was evaluated by computing a circumferentially-averaged NFPC value for each delivery method. Higher values indicate more cells being delivered to the limbal region. In panels G-I, each point represents a single eye. In bar graphs, data shown as mean ± standard deviation. For details of methods and statistics refer to text. *$p<0.05$.

Injection needles were fabricated as follows. We pulled glass micropipettes with a pipette puller, then scored, broke, and beveled the micropipette tips on a revolving diamond abrasive plate. The resulting needles had an OD of 100 μm or less, and a bevel angle of 30°. To improve sharpness and ease of penetration into corneal tissue, we rotated the needle on both lateral sides of the beveled surface and continued grinding until a sharp pointed tip was achieved. To avoid cell adhesion to the needle lumen, the needles underwent plasma cleaning and trichlorosilane treatment, followed by coating with 0.02% Pluronic F-127 (P2443, Sigma-Aldrich, St. Louis, MO). The needle was then loaded into an injection assembly (MMP-KIT, WPI, Sarasota, FL) which itself was mounted on a micromanipulator and connected to a microsyringe pump (PHD Ultra, Harvard Apparatus, Holliston, MA).

All animal procedures were conducted following guidelines approved by the Georgia Tech institutional animal care and use committee and consistent with the ARVO Statement for the Use of Animals in Ophthalmic and Vision Research. Eleven eyes of 7 wildtype C57BL/6 mice (Jackson Laboratory, Bar Harbor, ME) aged 3-5 months were used. For

each injection, a tropicamide eyedrop was instilled and anesthesia was induced using isoflurane, after which anesthesia was maintained through a nose cone while the animal was strapped on a heated bed at 37°C. The micropipette was sterilized with 70% ethanol and was loaded with 3 µl of cell-containing solution. Topical anesthetic (tetracaine) was applied to the eye, and the eye was proptosed using a pair of non-magnetic forceps while the needle was advanced into the AC using the micromanipulator. 1.5 µl of cell solution was injected into each eye, with the specifics of delivery varying based on the candidate delivery method, as outlined below.

Non-magnetic (passive) delivery: the cell solution was injected into the eye over 5 seconds, corresponding to a flow rate of 18 µl/min, as reported in previous studies in which non-magnetic polystyrene microbeads were delivered to the mouse TM (Calkins et al., 2018). We chose this flow rate because the microbeads used in the above-referenced study had a diameter similar to MSCs (~15 µm), and because we could not find a reported flow rate in previous studies that attempted passive cell delivery to the TM. After a 15-20 second wait to minimize AH backflow, the needle was withdrawn, and injection was complete.

Ring magnet method: The approach was similar to the passive delivery approach, except that after removing the needle a commercial N52 ring magnet ($ID = 3\,mm$, $OD = 4\,mm$ and 1mm thickness; R0545-10, SM Magnetics, Pelham, AL; Figure 11A, right) was placed over the limbus for 15 minutes according to previous studies (Snider et al., 2018).

Point magnet: The needle was kept in the eye while the pump delivered the cell solution in 4 aliquots of 0.375 µl at 2.4 µl /min. This lower injection flow rate gave the experimenter enough time to steer the cells to the TM in small aliquots while avoiding clumping of the cells, thus yielding a more consistent delivery. The experimenter triggered the injection of

each aliquot through a foot pedal and gradually dragged the injected cells towards the TM by placing the tip of the point magnet (consisting of a cubic N52 neodymium magnet connected to a thin stainless-steel rod; Figure 11A, right) on the limbus and slowly moving the tip along the circumference of one quadrant of the cornea. The same procedure was repeated for the remaining quadrants, and the needle was kept in the eye for an additional 15 minutes, for reasons discussed in detail below.

For all methods, the injected eye received topical antibiotic ointment (neomycin, polymyxin, and bacitracin ophthalmic combination) and the animal was allowed to recover on a heated pad.

The injected animals were euthanized by intraperitoneal injection of sodium pentobarbital 48 hrs after injection, and the eyes were carefully enucleated and immersion fixed in 10% formalin (Fisher Healthcare, Waltham, MA) overnight at 4°C, after which the anterior segments were dissected into 4 leaflets for wholemount fluorescent imaging. To visualize cell distribution around the circumference of the eye, fluorescent *en face* tile scans of the anterior segment wholemounts were taken using the 20X objective on a Leica DMB6 epifluorescent microscope (Leica Microsystems, Wetzlar, Germany). Next, at least two of the leaflets from each wholemount were cryoprotected by sequential immersion (15 min each) in 15% sucrose (Sigma) in PBS, 30% sucrose, and a 1:1 solution of 30% sucrose and optimal cutting temperature (OCT) media. The specimens were then embedded in OCT and were flash frozen in a 100% ethanol bath cooled by dry ice. A CryoStar NX70 cryostat (ThermoFisher Scientific, Waltham, MA) was used to cut 10 µm-thick sagittal sections. Tile scans of the sagittal sections were taken using the same microscope as above.

## 4.4 Results

We considered two metrics of cell delivery: the uniformity of cells around the entire anterior segment circumference (“uniformity of cell delivery”), and the proximity of cells to the TM (“specificity of cell delivery”), as follows.

### *4.4.1 Uniformity of cell delivery*

*En face* images (Figure 11 B-D) were analyzed using a semi-automated MATLAB v2020 (MathWorks, Natick, MA, USA) algorithm, as follows.

We manually marked the cut edges of the iris for each quadrant (Figure 11E).

We subdivided the marked region into subregions, such that the entire eye (assembly of the four marked regions) was made up of 10 radial “rings” and 21 “wedges” (Figure 11E, green grid shown for one quadrant). This meant that the number and the size of subregions in each quadrant depended on the size of the marked area in that quadrant compared to the others. For example, if the length of the arc that marked the limbus in quadrant A was half of that of quadrant B, quadrant A was assigned half the number of wedges as quadrant B.

We picked the two most exterior rings (Figure 11E, blue grid) to be the approximate location of the limbus and thus our region of interest (ROI). A normalized fluorescent pixel count (NFPC) for each of the subregions in the ROI was calculated by counting the number of fluorescent pixels in the subregion divided by the total number of pixels in the subregion.

Inside the ROI, each wedge was assigned the maximum NFPC of its two ring subregions, resulting in a single NFPC value for each of the 21 wedges.

This process was repeated for all the injected eyes (3 no magnet, 4 ring magnet, and 4 point magnet) providing an angular distribution of NFPCs for each eye (Figure 11F). We then derived two metrics of circumferential uniformity from such plots.

#### 4.4.1.1 Delivery adequacy

Even if cell delivery is not perfectly uniform, all wedges in an eye should ideally receive an "adequate" number of cells. To determine a threshold for this "delivery adequacy" we first calculated the mean NFPC over the 21 wedges of each eye. We found that the eyes in which cells were delivered using the point magnet method had, on average, the largest mean NFPC value (0.20), and we assumed any wedge that had an NFPC value less than 20% of this value to have had inadequate delivery, i.e. threshold NFPC = 0.04. "Delivery adequacy percentage" for each eye was then reported as the ratio of adequately delivered wedges over the total number of wedges.

#### 4.4.1.2 Coefficient of variation (CV)

We calculated the CV for each eye by dividing the standard deviation of NFPC distribution over all the wedges in an eye by the mean NFPC for that eye.

For the above analyses, we tested the assumption of normality for each group using the Shapiro-Wilk test, and then performed one-way ANOVA followed by Tukey's multiple comparison to compare various delivery methods.

We found that cell distributions in *en face* images of anterior segments were less uniform for the no magnet and ring magnet groups vs. the point magnet group (Figure 11B-D). This qualitative observation was confirmed by the NFPC distributions for each eye (Figure 11F) and delivery adequacy percentage for each method (Figure 11G). More than 90% of the wedges received "adequate" cells using the point magnet, whereas less than 10% did

for the other methods (point magnet vs. no magnet or ring: $p < 10^{-5}$). Statistical comparison between the coefficient of variation for the point magnet method ($0.8 \pm 0.2$) vs. both the ring magnet ($3.1 \pm 1.5, p = 0.02$) and no magnet ($3.2 \pm 0.3, p = 0.02$) methods showed that the point magnet method had significantly less spatial variability (Figure 11H).

By using the point magnet method, we expected to see a more uniform distribution of cells around the circumference of the limbus compared to both the no magnet case (due to segmental outflow) and the ring magnet method (which required the cells to be injected exactly in the center of the ring to spread evenly – a condition that was almost impossible to achieve experimentally). Consistent with our expectations, the point magnet approach yielded a lower CV and higher ratio of subregions with adequate cell concentration, indicating a significant improvement in the uniformity of delivery. This observation is contrary to the findings of Snider et al., who previously reported a significant improvement in uniformity using a ring magnet compared to passive delivery in a porcine anterior segment perfusion model (Snider et al., 2018). This might be due to size differences between the mouse and porcine eye, or because the porcine anterior segment preparation used by Snider et al. lacked most of the anterior segment structures that can interfere with cell delivery, such as the iris. The fact that *en face* images for the ring magnet method show a strong signal in the form of a ring closer to the pupil than the limbus is consistent with the existence of a "blocking" effect by the iris (Figure 11C).

### *4.4.2 Specificity of cell delivery (proximity to the TM)*

Circumferential uniformity is an important metric, but not the only measure of cell delivery quality. We also evaluated delivery specificity (proximity of cells to the TM), using two approaches. In the first, we simply evaluated the magnitudes of previously calculated mean NFPC values for our three delivery methods (Figure 11I). In the second, we

analyzed images of sagittal sections of the anterior segment for each injected eye (Figure 12A-C), using a custom image processing algorithm in MATLAB v2020. The algorithm quantified the specificity of delivery by calculating an "off-target index (OTI)" that we defined as in equation (1):

$$\mathrm{OTI} = \sum A\,B \tag{1}$$

$$A = \frac{\text{distance of pixel from TM measured along iris}}{\text{total length of iris contour}} \qquad B = \frac{\text{fluorescent intensity}}{\sum \text{fluorescent intensity}}$$

In order to calculate A, the boundary of the iris was marked by the user as a continuous contour (Figure 12D) starting from the TM and ending at the posterior side of the iris at the ciliary processes (Figure 12E). Next, the projection of each fluorescent pixel, representing labeled cells, onto the closest location on the iris contour was found (Figure 12D). The length of the contour segment bounded in between this projection point and the TM formed the numerator in quantity A.

The quantity B was the normalized fluorescent intensity for each pixel (note that the denominator in the definition of B is the sum of intensity for all pixels), which accounted for the cell concentration through the depth of the cryosections. The value of OTI, by construction, lay in the range from 0 to 1, with lower OTI values meaning more specific delivery to the TM for that section. We calculated the OTI for at least two quadrants per eye and at least one sagittal section per quadrant in all the injected eyes.

For statistical analysis, we confirmed the assumption of normality for each delivery method using the Shapiro–Wilk test. A linear mixed-effect model was then used to compare OTI values, with the fixed effect being the delivery method (ring magnet, focused magnet, or no magnet) and nested random effects being the eyes and sagittal sections (replicates) within each eye.

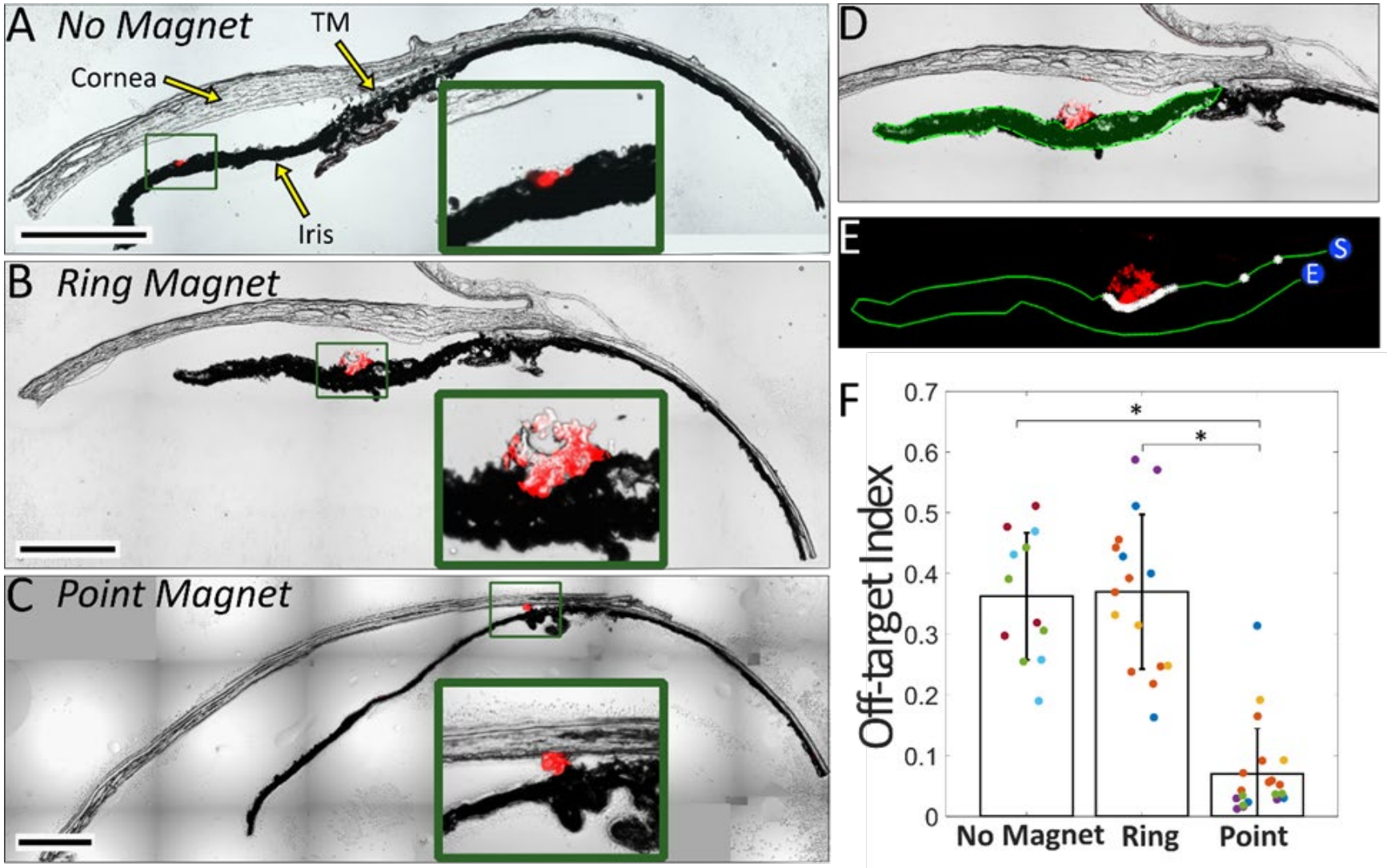
A No Magnet
TM
Cornea
Iris
B Ring Magnet
C Point Magnet
D
E
S
E
F
Off-target Index
0.7
0.6
0.5
0.4
0.3
0.2
0.1
0
*
*
No Magnet
Ring
Point

Figure 12. Specificity of cell delivery to the TM evaluated in sagittal sections. A-C) visualization of fluorescent cells (red) delivered to the AC using different methods. Insets show magnified view of cell-containing regions (red). D) Manual segmentation of the iris (green). E) Calculation of normalized distances by the algorithm. White asterisks show the projection of red fluorescent pixels (cells) onto the nearest point on iris contour. S and E mark the start of the iris contour at the TM and its end at the posterior side of the iris where the ciliary processes emerge, respectively. F) Off-target index (OTI) for different delivery methods. Each dot is one sagittal section, grouped by color for each eye. Lower OTI values mean better delivery specificity of injected cells. $* p < 0.05$. Scale bars: 300 μm.

We found that the delivery method NFPC, a measure of the concentration of cells in the limbal region, was nearly 20-fold higher for point magnet compared to either of the other methods (Figure 11I). In a more direct evaluation of delivery specificity, sagittal sections of injected eyes showed very different cell distributions between the various injection methods (Fig. Figure 12A-C). Calculation of OTI showed that the point magnet approach gave a ~5-fold improvement in the specificity of cell delivery: $0.07 \pm 0.07$ (mean ± SD) vs. ring magnet ($0.37 \pm 0.13$) or vs. no magnet ($0.36 \pm 0.10$) ($p < 10^{-10}$; Figure 12F). We also observed a smaller OTI standard deviation in point-magnet steered eyes, indicating improved delivery repeatability using the point magnet.

The specificity of cell delivery to the TM has important implications for safety of TM cell therapy, since, depending on the delivered cell type, off-target events can cause immunogenicity and tumorigenicity. Improved specificity can also mean more therapeutic benefit from fewer injected cells and potentially better cell retention after delivery, since delivered cells will reside in the correct niche. The improved specificity of cell delivery to the TM region using the point magnet was judged by several outcomes. First, histological assessment of *en face* images of the ACs containing fluorescently labeled MSCs showed a clear-cut ring at the limbus with little observable signal outside this ring. In line with these observations, we discovered that the point magnet gave a nearly 20-fold higher cell concentration in the limbal region vs. other methods, with delivered cells positioned 5 times closer to the TM, as indicated by the NFPC and OTI values, respectively. As

mentioned earlier, Wang et al. reported an increase in the percentage of cells delivered to the “anterior chamber angle” using a ring magnet vs. no magnet (Wang et al., 2022), while we saw no difference between these two methods using any of our cell delivery specificity parameters. However, their study did not specify important injection parameters (e.g. flow rate) or details of image processing and quantification, particularly the exact selection criteria for “anterior chamber angle” and its boundaries, which preclude a direct comparison with our results.

### 4.5 Limitations and conclusions

Our study has some limitations. In quantifying delivery specificity, we used sagittal images of the AC in which the lens had been removed, so that potential off-target delivery to the lens was not included in the calculations of specificity. We did, however, inspect the lenses of dissected eyes and observed minimal fluorescent signal (data not shown). Additionally, we report normalized parameters in all our results which, while useful for removing the effect of biological variations (such as iris length), dissection artifacts, cell fluorescent labeling efficiency variations etc., does not give much information about the total number of cells delivered using each method. One of the major sources of difference in the number of delivered cells may be the back-flush of cells through the corneal puncture site at the time of needle removal; such cell loss can undesirably reduce the therapeutic benefits of the treatment. Even though we have not quantified the total number of delivered cells, the point magnet method allowed for an extended cell incubation time inside the anterior chamber before removing the needle and thus is expected to experience the least cell loss of all three methods. Of course, the different needle retention times in the eye (15 minutes for the point magnet vs. < 1m for the other two methods) could itself be considered a limitation of our work due to its impact on cell retention inside the anterior chamber. However, this difference was an unavoidable aspect of the different delivery methods: in

the no magnet case, we attempted to keep the cannula in the eye for an extended duration, but most of the cells fell onto the lens (results not shown) and so this approach was abandoned in favor of the approach developed by previous studies as described earlier. In the ring magnet case, attempting the injection with the magnet in place was extremely challenging due to limited maneuvering space on the cornea as well clumping of the cells inside the needle due to magnetic attraction. Thus, we were forced to withdraw the needle before placing the ring magnet over the eye.

In summary, we have established a protocol for a new magnetic TM cell delivery method that is potentially safer, more effective, and more repeatable than previously reported methods. It is noteworthy that the point magnet delivery approach is relatively easy to carry out and cell placement is under direct control of the operator, suggesting potential for future translatability.

*Funding:* This work was supported by the National Institutes of Health R01 EY030071 (CRE, SYE, MHK) and the Georgia Research Alliance (CRE).

# CHAPTER 5. MAGNETICALLY-STEERED CELL THERAPY FOR TRABECULAR MESHWORK REFUNCTIONALIZATION IN OPEN ANGLE GLAUCOMA

This chapter is a manuscript to be submitted to *Nature Biomedical Engineering* with the following author list:

M. Reza Bahrani Fard, Jessica Chan, A. Thomas Read, Guorong Li, Lin Cheng, Babak N. Safa, Seyed Mohammad Siadat, Stanislav Y. Emelianov, W. Daniel Stamer, Markus H. Kuehn, C. Ross Ethier.

And title:

“Magnetically-steered cell therapy for trabecular meshwork refunctionalization in open angle glaucoma.”

## 5.1 Abstract

Trabecular meshwork (TM) cell therapy has been proposed as a next-generation treatment for elevated intraocular pressure (IOP) in glaucoma, the most common cause of irreversible blindness. Using a magnetic cell steering technique with excellent efficiency and tissue-specific targeting, we delivered two types of cells into a mouse model of glaucoma: either adipose-derived mesenchymal stem cells (hAMSCs) or induced pluripotent cell derivatives (iPSC-TM cells). We observed a 27% reduction in intraocular pressure (IOP) for nine months after a single dose of only 1500 magnetically-steered hAMSCs, associated with refunctionalizing the conventional outflow pathway, as judged by increased outflow facility and TM cellularity. iPSC-TM cells were also effective, but less

so, showing only a 13% IOP reduction and unacceptable tumorigenicity. In both cases, injected cells remained detectable in the iridocorneal angle three weeks post-transplantation. Based on the locations of delivered cells, the mechanism of IOP lowering is most likely paracrine signaling. We conclude that magnetically-steered hAMSC cell therapy has potential for long-term treatment of ocular hypertension in glaucoma.

## 5.2 Introduction

Glaucoma, an optic neuropathy, is the leading cause of irreversible blindness, with more than 80 million cases worldwide (Tham et al., 2014). Primary open angle glaucoma (POAG), the most common subtype of the disease, is characterized by a gradual loss of retinal ganglion cells and a corresponding loss of vision. While the exact mechanism underlying retinal ganglion loss is not well understood, elevated intraocular pressure (IOP) is a major risk factor (Coleman and Miglior, 2008), consequently, all current clinical treatments seek to lower IOP, whether by medical or surgical means. However, the success of such IOP-lowering treatments is reduced by low patient adherence to medical therapies (Reardon et al., 2011), by post-surgical complications, and/or by patients becoming refractory to originally successful treatments (Heijl et al., 2002). Thus, there remains a major unmet public health need for methods that offer sustained IOP control in glaucoma patients.

The trabecular meshwork (TM; Figure 13A) is an ocular tissue that drains the majority of aqueous humor from the human eye, and its function is a major determinant of IOP. There are a number of age- and glaucoma-associated changes in the TM, including an age-associated loss of TM cells which is accelerated in POAG (Alvarado et al., 1984). This cell deficiency has been identified as a therapeutic target for IOP control in glaucoma patients, with multiple groups attempting to re-functionalize the TM by injection of stem cells into

the eye to restore normal IOP homeostasis (Manuguerra-Gagné et al., 2013; Roubeix et al., 2015; Abu-Hassan et al., 2015; Zhu et al., 2016, 2017; Yun et al., 2018; Zhu et al., 2020; Zhou et al., 2020; Xiong et al., 2021).

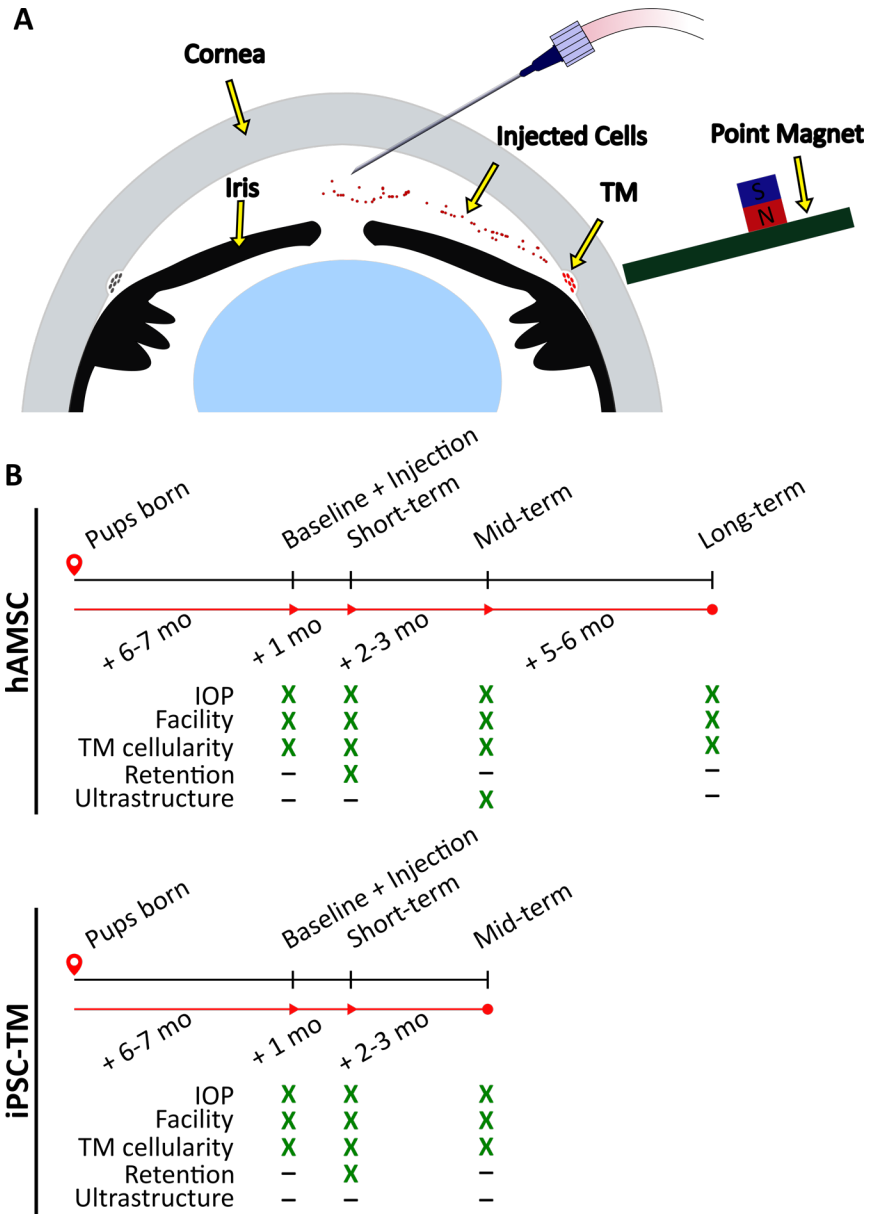


Figure 13. Experimental schematic and design. A) Schematic of magnetically-steered cell delivery to the TM. As cells are injected into the anterior chamber at a low flow rate, the experimenter places the “point magnet” (Bahrani Fard et al., 2023) on the limbus and carefully drags the cells towards the iridocorneal angle, targeting the trabecular meshwork (TM). Features of the figure are not to scale. B) Time-line of the experiments. An ultrastructural analysis, specifically the quantification of inner wall basement membrane

fenestrations, was not undertaken for eyes receiving iPSC-TMs due to their inferior performance. Additionally, cell retention in the anterior chamber was only investigated at the short-term. Note that baseline measurements were taken for WT and transgenic animals that did not necessarily receive an injection afterwards. Refer to Methods for a description of various experimental groups and further details.

Despite the potential of stem cell treatment for IOP control, there remain several critical barriers to translation. For example, cell injection into the anterior chamber typically relies on passive transport of cells to the TM, leading to extremely low delivery efficiencies (Wang et al., 2022). A more efficient delivery method is desirable, which would be expected to both increase the therapeutic benefit of the treatment and reduce immunogenicity; for example, Zhou et al. reported an increase in the inflammatory markers CD45 and GR1 and T-cell markers CD4 and CD3 in the iris and the cornea after mesenchymal stem cell injection, likely due to off-target cell delivery (Zhou et al., 2020). We have recently introduced a magnetically-steered cell delivery technique which significantly outperformed previously-used magnetic and non-magnetic delivery techniques (Bahrani Fard et al., 2023); here we characterize the efficacy of stem cell delivery using this technique on IOP lowering and aqueous humor dynamics.

A second barrier to translation is lack of knowledge about which cell type should be delivered to refunctionalize the TM. Three types of cells have previously been used in this context: native TM stem cells (TMSC), mesenchymal stem cells, and induced pluripotent stem cell (iPSC) derivatives. TMSC therapy lowers IOP and increases TM cellularity (Xiong et al., 2021; Yun et al., 2018), and is theoretically attractive. However, the scarcity of TMSCs, constituting of only 2-5% of the entire TM cell population (Braunger et al., 2014), and the invasiveness of the required cell collection procedure significantly reduce the translational potential of this cell source. Alternatively, mesenchymal stem cells have been used in several studies, showing a transient IOP reduction as well as neuroprotection (Manuguerra-Gagné et al., 2013; Roubeix et al., 2015). For example, Manuguerra-Gagné

et al. injected bone-marrow derived mesenchymal stem cells in a rat model of IOP elevation, observing a reduction in IOP for three weeks (Manuguerra-Gagné et al., 2013), These results, together with the ease of sourcing autologous cells, and the established safety of mesenchymal stem cell therapy in clinical trials (Lalu et al., 2012; Rodríguez-Fuentes et al., 2021), make these stem cells a strong candidate for clinical POAG cell therapy. Finally, iPSCs can be differentiated into iPSC-TM cells, with the differentiated cells displaying phenotypic similarity to adult TM cells (Ding et al., 2014). Intracameral injection of iPSC-TMs into a perfused porcine anterior segment POAG model restored the IOP homeostatic response (Abu-Hassan et al., 2015). Additionally, Zhu and colleagues delivered iPSC-TMs into the anterior chambers of ocular hypertensive mice and reported increased TM cellularity due to proliferation of endogenous cells and a corresponding decrease in the IOP for up to 12 weeks after cell delivery (Zhu et al., 2017, 2016). Here we compare the benefits of mesenchymal stem cells vs. iPSC-TM cells.

An additional barrier to translation is the choice of an appropriate animal model for preclinical testing, since no animal model replicates all the pathological phenotypes of POAG. For example, although non-human primate models show high anatomical and functional resemblance to humans and are the gold standard for certain pre-clinical studies (Friedman et al., 2017), induction of ocular hypertension requires laser photocoagulation of the TM, which is very unlike TM changes seen in POAG (Acott et al., 1989; Manuguerra-Gagné et al., 2013), Microbead (Sappington et al., 2010) and hypertonic saline (Morrison et al., 1997) models of ocular hypertension are similarly non-fidelic to human POAG. Commercially available DBA/2 mice show TM cell loss and IOP elevation but are associated with undesirable systemic and ocular complications (Turner et al., 2017). Thus, in this work we chose to use transgenic $MYOC^{Y437H}$ mice, a model of

myocilin-associated POAG, which have been reported to show an accelerated loss of TM cellularity and gradually developing ocular hypertension (Zode et al., 2011).

In summary, we here evaluate the effectiveness of TM cell therapy, using a magnetic cell steering method and two clinically relevant cell choices, namely human adipose-derived mesenchymal stem cells (hAMSCs) and iPSC-TM cells, in MYOC$^{Y437H}$ mice. We judged effectiveness by the extent and longevity of IOP reduction, improvement in outflow facility, and increase in TM cellularity, among other outcome measures, and performed experiments using animal cohorts at different time points (Figure 13 B, detailed in Methods section). Our data demonstrate a sustained IOP lowering and a significant benefit of magnetic stem cell steering in the eye.

## 5.3 Results

### *5.3.1.1 Stem cell transplantation lowered IOP and improved aqueous humor dynamics*

We delivered and magnetically steered either hAMSCs or iPSC-TMs to the TM in the eyes of MYOC$^{Y437H}$ mice (Figure 13 A), measuring IOPs and outflow facilities at short-, mid- and long-term time points, corresponding to ~1 month, 3-4 months, and 9 months after stem cell delivery (Figure 13 B). Outflow facility is the numerical inverse of the hydraulic resistance to aqueous humor drainage from the eye, and is a key functional metric of the TM. Our high-level goals were to: (i) elucidate the impact of hAMSC or iPSC-TM delivery on IOP; and (ii) quantify the portion of IOP change due to changes in outflow facility.

We expected transgenic MyocY437H mice to show elevated IOP by 6-7 months of age, when baseline IOP measurements were taken (Zhu et al., 2017, 2016; Zode et al., 2011). However, we surprisingly saw no meaningful IOP difference between Tg-MYOC$^{Y437H}$ mice (Tg group) vs. wild-type littermates (Figure 14; Table 1 and Table 2). Despite this lack of

IOP elevation in the transgenic model, magnetically-steered delivery of hAMSCs led to a marked IOP decrease in Tg animals as compared to sham injection of saline at short-, mid-, and long-term time points. The IOP reduction was sustained in hAMSC-treated eyes over all three time points, with no statistically significant difference between any combination of these time points. iPSC-TM treatment also led to a reduction in IOP compared to sham (phosphate-buffered saline, PBS) injection controls at both the short- and mid-term time points, although this difference did not reach statistical significance at the latter time. The IOP reduction due to iPSC-TM cells was approximately half that due to hAMSC treatment at both short- and medium-term time points (short term: $-4.3\ [-5.6, -2.9]\ mmHg$ for hAMSC vs. $-2.3[-3.6, -1.0]\ mmHg$ for iPSC-TM, $p < 0.021$; mid-term: $-4.5[-5.8, -3.1]\ mmHg$ for hAMSC vs. $-1.9[-3.3, -0.4]\ mmHg$ for iPSC-TM, $p < 0.005$; all data reported as means and 95% confidence intervals).

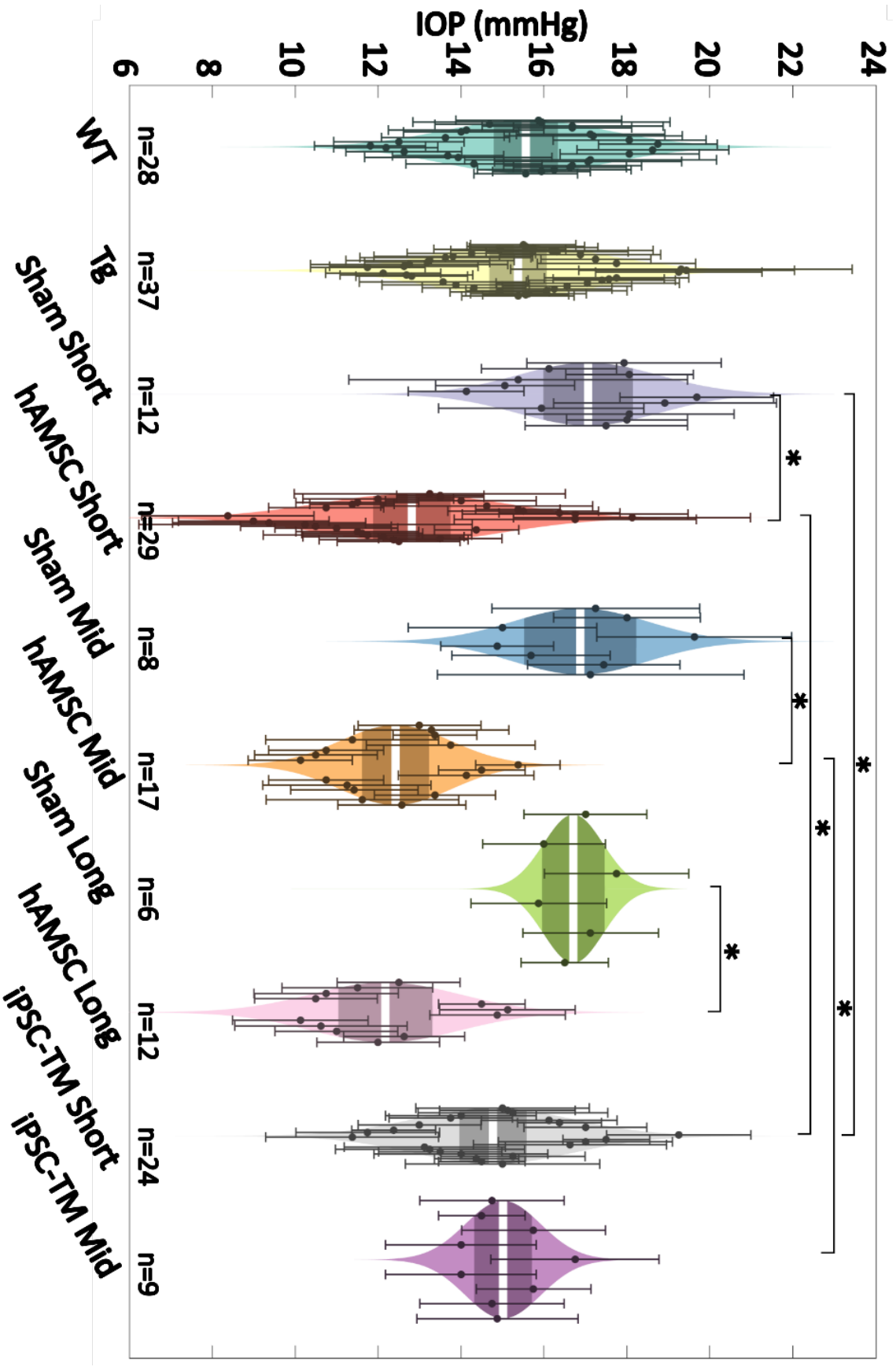
IOP (mmHg)
6
8
10
12
14
16
18
20
22
24
WT
Tg
Sham Short
hAMSC Short
Sham Mid
hAMSC Mid
Sham Long
hAMSC Long
iPSC-TM Short
iPSC-TM Mid
n=28
n=37
n=12
n=29
n=8
n=17
n=6
n=12
n=24
n=9
*
*
*
*
*
*

Figure 14. IOP measurements for experimental cohorts. In each group, the central white strip indicates the mean, while the darker region represents the 95% confidence interval on the mean. The colored region shows the distribution. Dots represent individual eyes, with error bars demarcating the 95% confidence intervals. For further information on experimental groups and statistical analysis refer to text. *$p < 0.05$ before Bonferroni correction. WT: wildtype hybrid mice (naïve control), Tg: Tg-MYOCY437H mice, Sham: Tg mice receiving saline injection, hAMSC: Tg mice receiving magnetically-steered hAMSCs, iPSC-TM: Tg mice receiving magnetically-steered iPSC-TMs. “Short”, "Mid”, and “Long” refer to time points.

Table 1. Outcome measures, shown as means and [95% confidence intervals].

| Group | IOP (mmHg) | Facility (nl/min/mmHg) | Cellularity (nuclei/μm) |
|---|---|---|---|
| WT | 15.6 [14.8,16.3] | 4.4 [3.7,5.2] | 0.24 [0.15,0.33] |
| Tg | 15.4 [14.7,16.1] | 3.8 [3.3,4.4] | 0.28 [0.23,0.32] |
| Sham Short | 17.1 [16.0,18.1] | 3.2 [2.3,4.3] | 0.27 [0.20,0.34] |
| MSC Short | 12.8 [11.9,13.8] | 8.4 [6.3,11.2] | 0.58 [0.42,0.73] |
| Sham Mid | 16.9 [15.5,18.2] | 3.0 [2.1,4.3] | 0.24 [0.18,0.31] |
| MSC Mid | 12.4 [11.6,13.2] | 8.4 [7.1,9.9] | 0.40 [0.34,0.47] |
| Sham Long | 16.7 [16.0,17.5] | 3.4 [2.8,4.2] | 0.23 [0.17,0.28] |
| MSC Long | 12.2 [11.0,13.3] | 8.0 [5.9,10.9] | 0.37 [0.31,0.43] |
| iPSC-TM Short | 14.8 [14.0,15.6] | 4.3 [3.0,6.2] | 0.36 [0.27,0.45] |
| iPSC-TM Mid | 15.0 [14.3,15.7] | 4.3 [3.6,5.1] | 0.34 [0.21,0.47] |

Table 2. Result of multiple comparison for various groups and variables, with statistically significant comparisons highlighted in orange*.

| | Compared groups | | p-values | | |
|---|---|---|---|---|---|
| | Vs. | | IOP | Facility | Cellularity |
| 1 | WT | Tg | 0.3579 | 0.1353 | 0.6264 |
| 2 | Tg | Sham Short | 0.0070 | 0.0901 | 0.9214 |
| 3 | Tg | Sham Mid | 0.0311 | 0.0614 | 0.2879 |
| 4 | Tg | Sham Long | 0.0652 | 0.1865 | 0.2442 |
| 5 | Sham Short | hAMSC Short | 0.0000 | 0.0001 | 0.0000 |
| 6 | Sham Short | iPSC-TM Short | 0.0006 | 0.0692 | 0.0535 |
| 7 | hAMSC Short | hAMSC Mid | 0.2786 | 0.4838 | 0.0000 |
| 8 | hAMSC Short | hAMSC Long | 0.2111 | 0.4045 | 0.0000 |
| 9 | hAMSC Short | iPSC-TM Short | 0.0013 | 0.0019 | 0.0000 |
| 10 | Sham Mid | hAMSC Mid | 0.0000 | 0.0000 | 0.0001 |
| 11 | Sham Mid | iPSC-TM Mid | 0.0047 | 0.0210 | 0.0072 |
| 12 | hAMSC Mid | hAMSC Long | 0.3497 | 0.3719 | 0.5595 |
| 13 | hAMSC Mid | iPSC-TM Mid | 0.0001 | 0.0000 | 0.2751 |
| 14 | Sham Long | hAMSC Long | 0.0000 | 0.0000 | 0.0020 |
| 15 | iPSC-TM Short | iPSC-TM Mid | 0.3597 | 0.4877 | 0.8516 |

* Post-hoc comparisons were performed after ANOVA (for IOP and outflow facility) or linear mixed-effect model (for TM cellularity). Bonferroni correction was used to adjust the critical p-value from 0.05 to 0.0033 (based on the 15 reported comparisons).

We observed increases in outflow facility for eyes receiving stem cells which were consistent with those observed for IOP (Figure 15 A-B; Table 1 and Table 2). Specifically, no significant difference in facility was found between the naïve wildtype (WT) and transgenic groups, while hAMSC treatment led to a marked increase in outflow facility vs. injection (sham) controls at short-, mid- and long-term time points. Further, the percentage increases in facility due to hAMSC delivery vs. sham injection controls were similar at all time points. Groups receiving iPSC-TMs also showed an increase in facility, but these differences did not reach statistical significance. Specifically, hAMSC delivery led to a significantly higher percentage increase in facility compared to iPSC-TM delivery (short-term: $170\ [70{,}310]\%$ for hAMSC vs. $40\ [-10{,}110]\%$ for iPSC-TM, $p < 0.011$; mid-term: $180\ [110{,}280]\%$ for hAMSC vs. $40\ [0{,}110]\%$ for iPSC-TM, $p < 0.003$; data reported as percent increase in treatment group compared to relevant (sham) injection control).

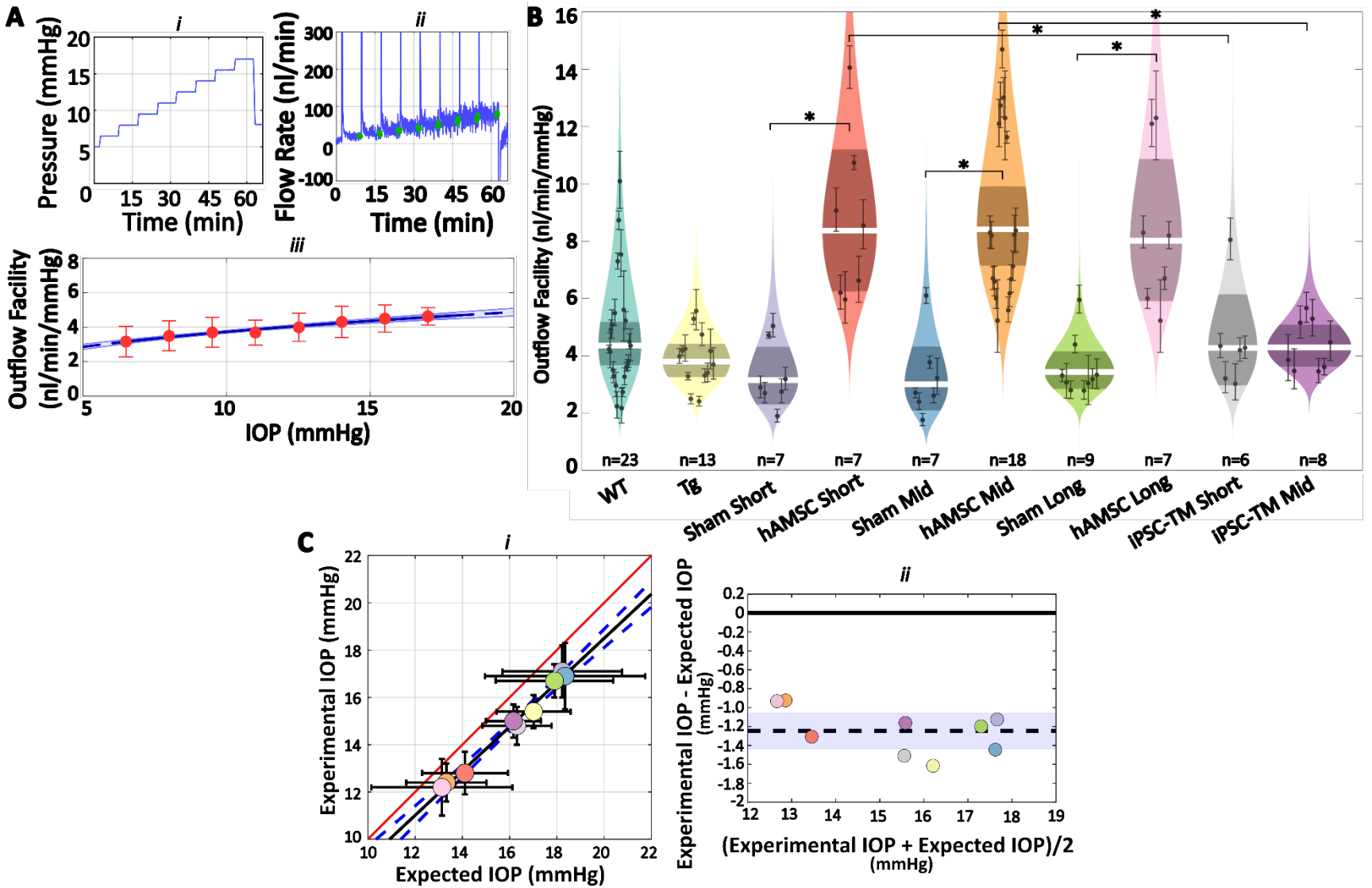
A
i
Pressure (mmHg)
Time (min)
ii
Flow Rate (nl/min)
Time (min)
iii
Outflow Facility (nl/min/mmHg)
IOP (mmHg)
B
Outflow Facility (nl/min/mmHg)
n=23
n=13
n=7
n=7
n=7
n=18
n=9
n=7
n=6
n=8
WT
Tg
Sham Short
hAMSC Short
Sham Mid
hAMSC Mid
Sham Long
hAMSC Long
iPSC-TM Short
iPSC-TM Mid
C
i
Experimental IOP (mmHg)
Expected IOP (mmHg)
ii
Experimental IOP - Expected IOP (mmHg)
(Experimental IOP + Expected IOP)/2 (mmHg)

Figure 15. Outflow facility measurements. **A** i-iii) show data for a representative eye. A i-ii) IOP and flow rate vs. time for multiple pressure steps during the perfusion experiment. After each pressure step, the system automatically waits for a steady state inflow rate to be achieved, based on a criterion of the rate of change in the inflow rate falling below 3 nl/min/min. The steady intervals for each step are shown in green. Data has been trimmed to not include preparatory and pre-loading phases. A iii) Calculated outflow facility (red dots) vs. IOP. The line shows the fitted model and the shaded region is the 95% confidence interval on the regression line. Error bars are 95% confidence intervals on individual steps. **B)** Outflow facility measurements across different experimental cohorts. Refer to Figure 14 for interpretation details. Note that outflow facilities in mice follow a log-normal distribution. **C)** Cross-validation of experimentally-measured and expected IOP, calculated from measured facility values. i) Regression plot of experimental vs. expected IOPs. Solid black fitted line ($y = 0.94x - 0.21,\ R^2 = 0.99$) is shown along with its confidence bounds in dashed blue. Error bars show 95% confidence interval on both experimental (vertical) and expected (horizontal) IOPs. The unity line is shown as a solid red line. ii) Bland-Altman plot of residuals (difference between experimental and expected IOPs) vs. average of experimental and expected IOPs. Individual experimental groups are indicated by colors matching those in panel B. Dashed line is shows the mean and is shown along with its 95% confidence interval (shaded). Solid line shows zero difference between the two parameters, i.e. the null hypothesis. For further information on experimental groups and statistical analysis refer to text. $*\ p < 0.05$ before Bonferroni correction.

We then asked whether the measured decreases in IOP were quantitatively consistent with the experimentally-measured increases in outflow facility. To answer this question, we used the modified Goldmann equation, which relates IOP to facility and other variables, computing an "expected" IOP from the facility measurements for each cohort of mice. Comparison of this expected IOP with the actual (measured) IOP showed a close correlation (Figure 15 C*i*), determined by linear regression (slope of fitted line was not statistically different than 1, $p = 0.22,\ R^2 = 0.99$). Still the outflow facility measurements overestimated the actual IOP by a small amount ($1.2\ [1.1, 1.3]\ mmHg,\ p < 10^{-6}$, null hypothesis: average difference between experimental and expected IOPs equals zero, Figure 15 C*ii*). Despite this "shift" between the experimentally-measured and expected IOP, the horizontal error bars in Figure 15 C*i*, derived by a propagation of error analysis, include the unity line for all groups, suggesting that the small discrepancy between the two experimental and expected values falls within the error of measurements (see Discussion).

### *5.3.2 Cell delivery increased TM cellularity*

The observed reductions in IOP and increases in outflow facility after delivery of both stem cell types suggested some refunctionalization of the conventional outflow pathway. We therefore asked whether these changes were associated with alteration of the cellular density in the TM by evaluating cell counts in histological sections of the iridocorneal angle tissues in eyes receiving stem cells and (sham) injection control eyes (Figure 16; Table 1 and Table 2). We observed more nuclei in eyes receiving cell transplantation, with a striking 2.2-fold increase in TM cellularity (normalized to the anterior-posterior length of the outflow tissues) after hAMSC treatment at the short-term time point vs. the corresponding (sham) injection control (Figure 16 C). Interestingly, this spike in TM cell density was followed by a decline over time, reaching a 1.6-fold increase at the mid-term time point, and apparently plateauing at 1.6-fold at the long-term time point. Despite this modest decline, hAMSC-treated eyes showed significantly higher cellularity vs. their injection controls at both mid-term and long-term time points.

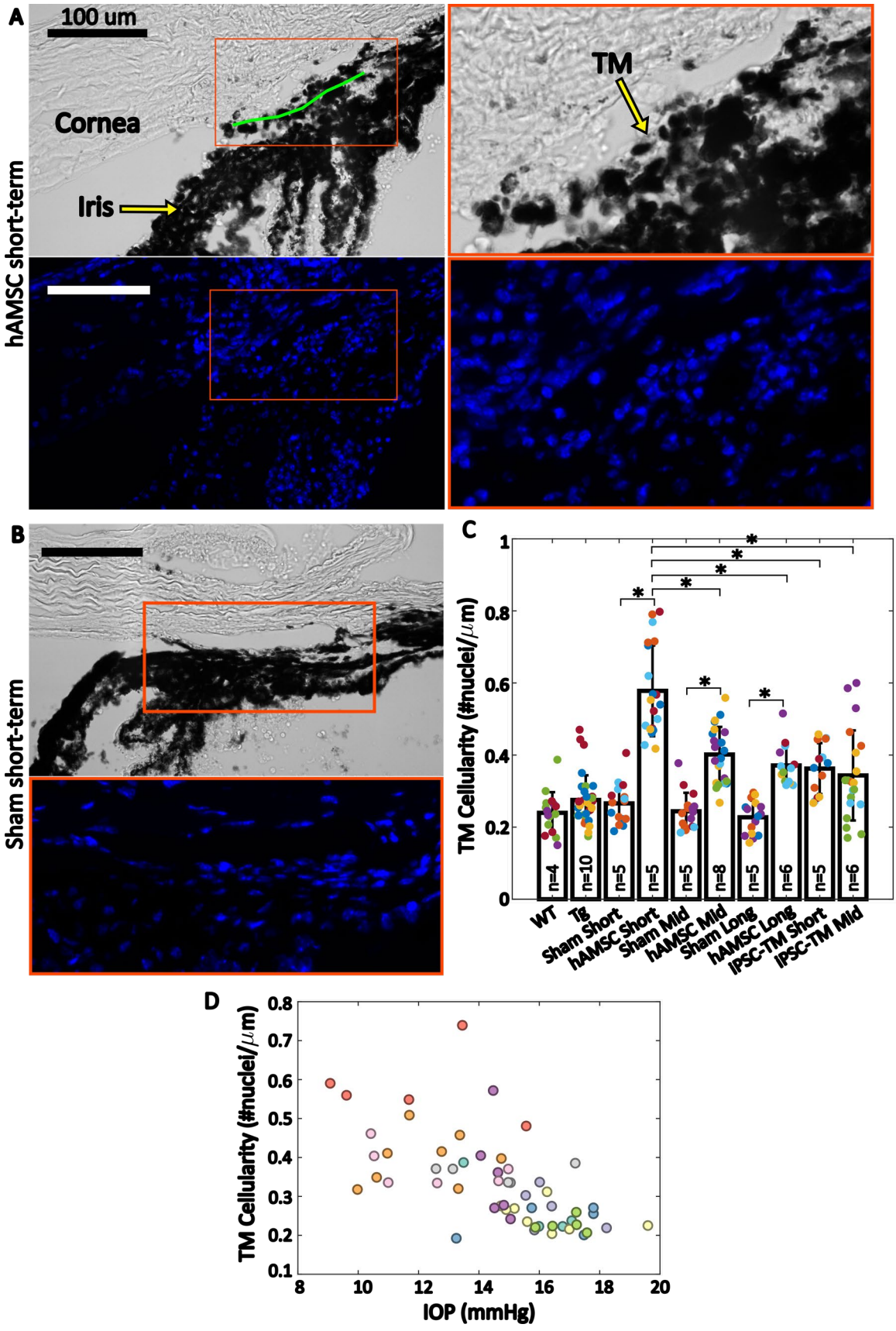
A
100 um
Cornea
Iris
TM
hAMSC short-term
B
Sham short-term
C
TM Cellularity (#nuclei/$\mu$m)
n=4
n=10
n=5
n=5
n=5
n=8
n=5
n=6
n=5
n=6
WT
Tg
Sham Short
hAMSC Short
Sham Mid
hAMSC Mid
Sham Long
hAMSC Long
IPSC-TM Short
IPSC-TM Mid
D
TM Cellularity (#nuclei/$\mu$m)
IOP (mmHg)

Figure 16. Quantification of TM Cellularity. A and B) Brightfield and fluorescent micrographs of the irideocorneal angle (sagittal view) taken from a representative eye from the iPSC-TM short-term (A) and sham short-term (B) experimental groups. Green line shows the contour of the TM along the inner wall of Schlemm's Canal used for normalizing nuclei count. DAPI-stained nuclei in the fluorescent image are shown in blue. Insets show a magnified view of the angle. C) Comparison of normalized TM cellularity for various experimental cohorts. Bars show mean and standard deviation. Multiple sections analyzed from each eye are coded with the same color. n = number of eyes. Linear mixed-effect model, *$p < 0.05$ before Bonferroni correction. D) Cross-comparison of TM cellularity vs. IOP for the eyes shown in panel C. The strong negative trend of the data has a Pearson correlation coefficient of $-0.63$ and $p < 10^{-7}$. Each color represents one eye and different colors are matched to the experimental groups shown in Figure 14.

Delivery of iPSC-TMs also led to an increase in TM cellularity vs. their (sham) injection controls at both short-term and mid-term time points, although these differences were more modest than seen in hAMSC-injected eyes and did not reach statistical significance. Interestingly, the TM cellularities in iPSC-TM-treated eyes at both time points were comparable to those at the mid-term and long-term time points in hAMSC-treated eyes, but were significantly different than hAMSC-treated eyes at the short-term time point.

Cross-plotting normalized TM cellularity vs. IOP for pooled data from all the experimental groups (Figure 16D) showed a strong negative correlation between these two parameters (Pearson correlation coefficient = $-0.63$, $p < 10^{-7}$).

### *5.3.3 hAMSC transplantation significantly increased basement membrane fenestrations*

An increased deposition of ECM, and in particular basement membrane material (BMM), in the TM immediately adjacent to the inner wall (IW) of Schlemm's canal has been associated with ocular hypertension (Li et al., 2021; Overby et al., 2014). Since this region within the TM accounts for the majority of AH outflow resistance (Ethier et al., 1986), we

asked whether the BMM profile was altered by stem cell treatment by comparing the mid-term hAMSC transplanted group vs. its corresponding injection control (Figure 17).

Reduced amounts of BMM adjacent to the inner wall of Schlemm's canal were evident in transmission electron micrographs from eyes receiving hAMSCs compared to sham-injected controls at the mid-term time point (Figure 17A). Quantification showed that stem cell treatment significantly decreased the amount of BMM, as determined by the ratio of cumulative BMM length adjacent to the inner wall to total inner wall length; specifically, this ratio was 0.76 [0.59, 0.93] in sham-treated eyes vs. 0.39 [0.16, 0.62] in hAMSC-treated eyes ($p < 10^{-10}$).

Measurements of basement membrane fenestrations performed here would benefit from repeated measurements by at least one additional individual to reduce subjective error.

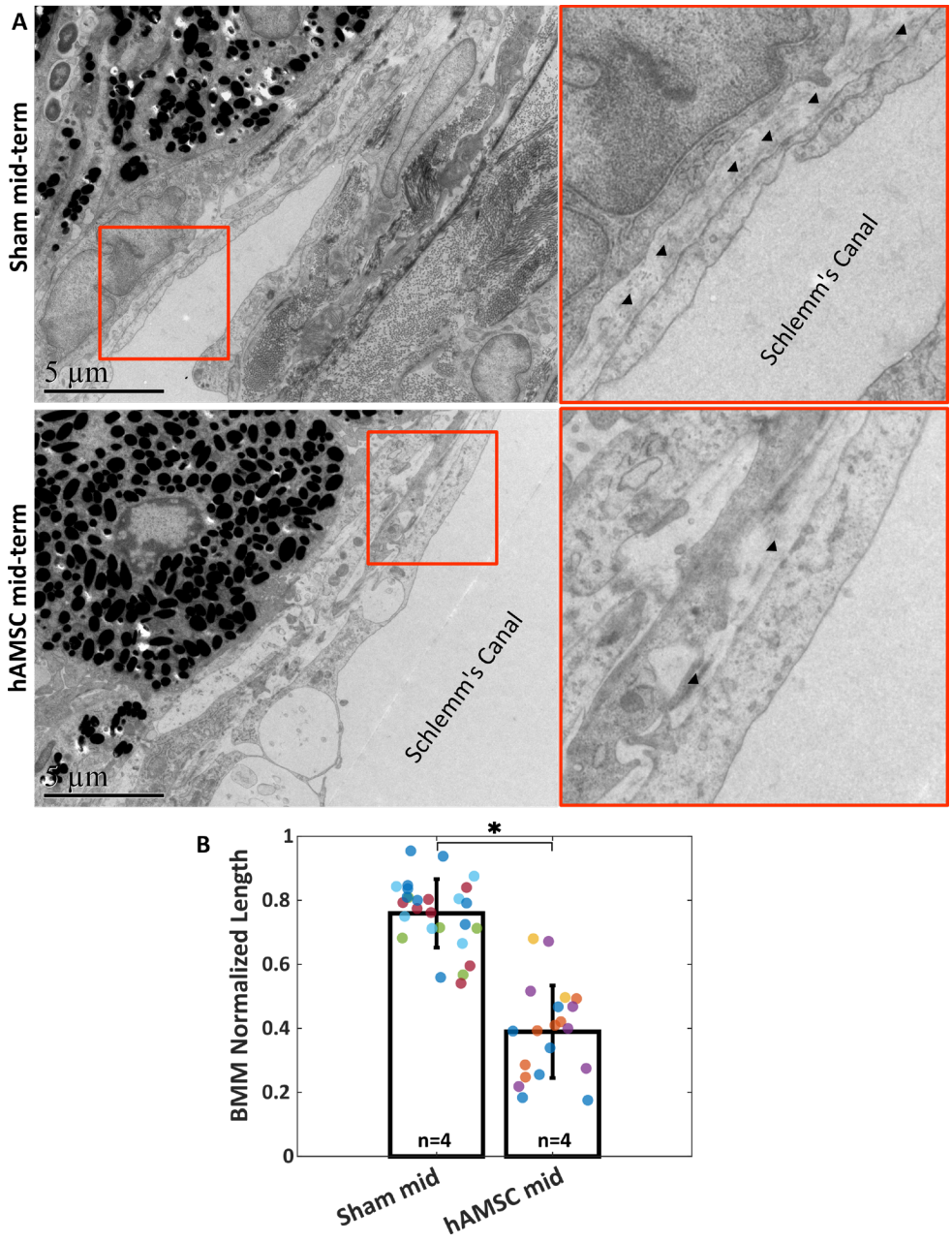


Figure 17. Ultrastructural analysis of ECM underlying the inner wall of Schlemm's canal (basement membrane material, or BMM). A) Greater amounts of BMM are evident immediately adjacent to the inner wall of Schlemm's canal (arrowheads) in a saline-injected eye (top row) vs. in a hAMSC-treated eye (bottom row) at the mid-term time point. The images at right are a zoomed view of the orange boxed areas in the left panels. B) The normalized length of BMM directly in contact with the IW plotted for the experimental groups represented in panel A. Multiple sections analyzed from each eye are coded with the same color. n = number of eyes. Linear mixed-effect model. $* p < 0.05$.

### *5.3.4 Exogenous cells were retained for multiple weeks in the TM*

Manuguerra-Gagné et al. previously reported a surprisingly low retention duration for hAMSCs injected into rat eyes, with virtually no fluorescently labeled exogenous cells being present in histological sections four days after injection (Manuguerra-Gagné et al., 2013). We therefore pre-labelled injected cells with PKH26 fluorescent dye, which allowed us to track cells for up to 3 weeks after injection. *En face* images showed a relatively uniform distribution of cells over the entire circumference of the eye (Figure 18A), similar to previous results with magnetically steered cells (Bahrani Fard et al., 2023). Sagittal sections (Figure 18B) showed an accumulation of exogenous cells deep within the iridocorneal angle. Interestingly, strong fluorescent signal was observed within the TM in iPSC-TM-injected eyes, indicating cell integration with the target tissue; in contrast, most hAMSCs accumulated close to the TM (within $\sim 50\ \mu m$), but did not enter the TM as did the iPSC-TM cells. Note that fluorescent signals observed in the posterior part of the eye and outside the eye near the limbus were caused by autofluorescence (supplementary Figure 43).

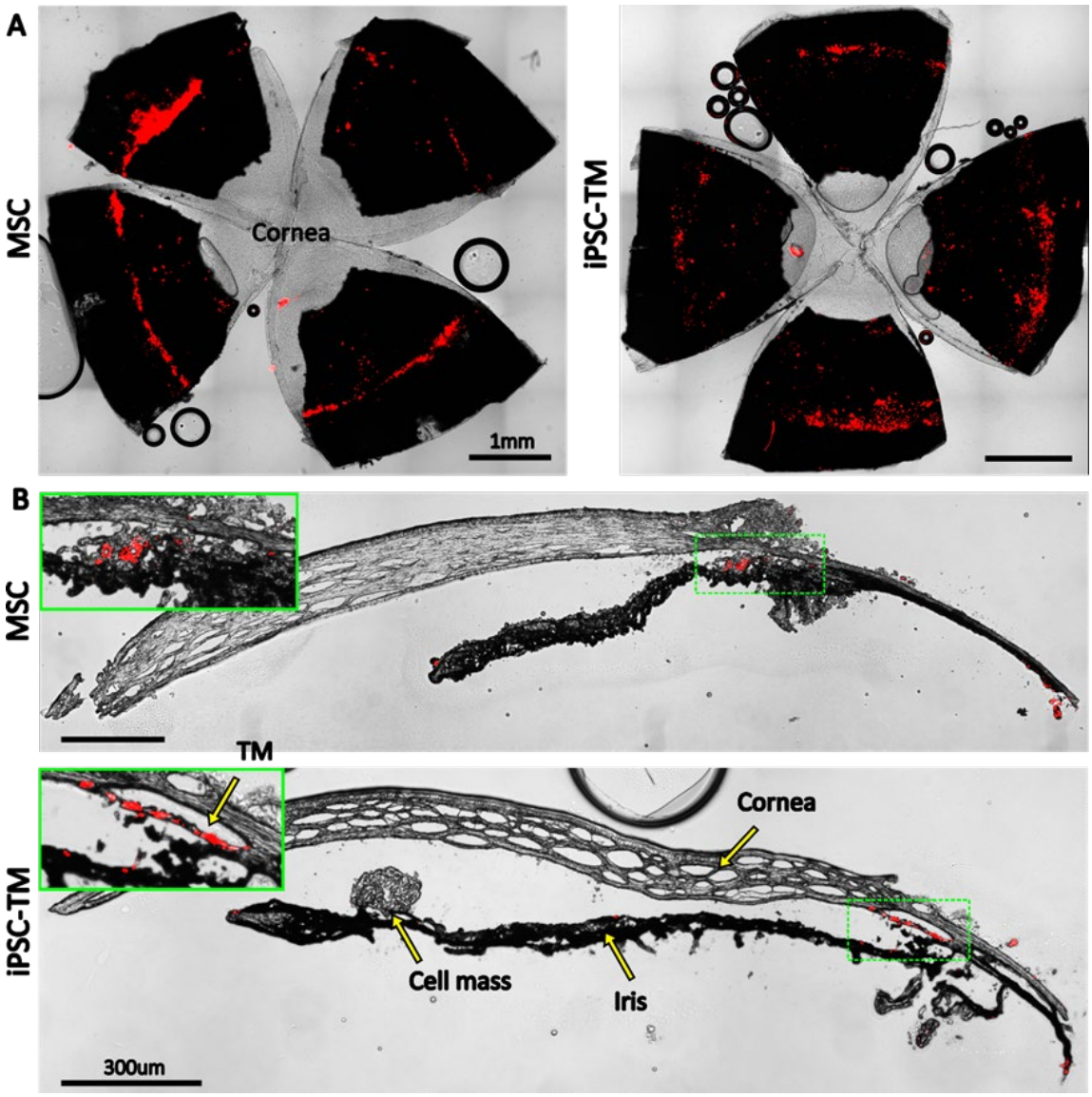


Figure 18. Retention of exogenous cells inside the anterior segment 3 weeks after injection. Distribution of both hAMSC and iPSC-TM cells (red) are shown in A) en face images of the anterior segments and B) sagittal sections. In panel B), insets show a magnified view of the sites with the most intense fluorescent signal. Autofluorescence can be seen in the posterior chambers as well as outside the corneoscleral shell. A cell mass, possibly a growing tumor, can be seen over the iris in the iPSC-TM injected eye.

### *5.3.5 iPSC-TM transplantation led to significant incidence of tumor formation*

Unfortunately, there was a very high rate of tumorigenicity in eyes receiving iPSC-TMs, with more than 60% of eyes showing large intraocular masses within a month of cell

injection, typically on the iris (Figure 18B). In most cases these tumors left the eyes unusable for IOP or outflow facility measurements. Examination of select iPSC-TM transplanted sections by a board-certified pathologist (HEG) confirmed the presence of tumors (Figure 19), based on the observation of rosettes and neuroectodermal phenotype, characteristics also found in various tumor types, including retinoblastoma (Wippold and Perry, 2006). Additionally, a high nuclear-cytoplasmic ratio, a hallmark of tumor malignancy (Moore et al., 2019), and rarefaction due to tissue necrosis were noted. No signs of tumor growth were observed in the eyes injected with hAMSCs at the long-term time point (Figure 19).

Since histology was only performed on a subset of the eyes after outflow facility measurements, it is possible that there may also have been tumors in the iPSC-injected eyes reported in the IOP and outflow facility plots.

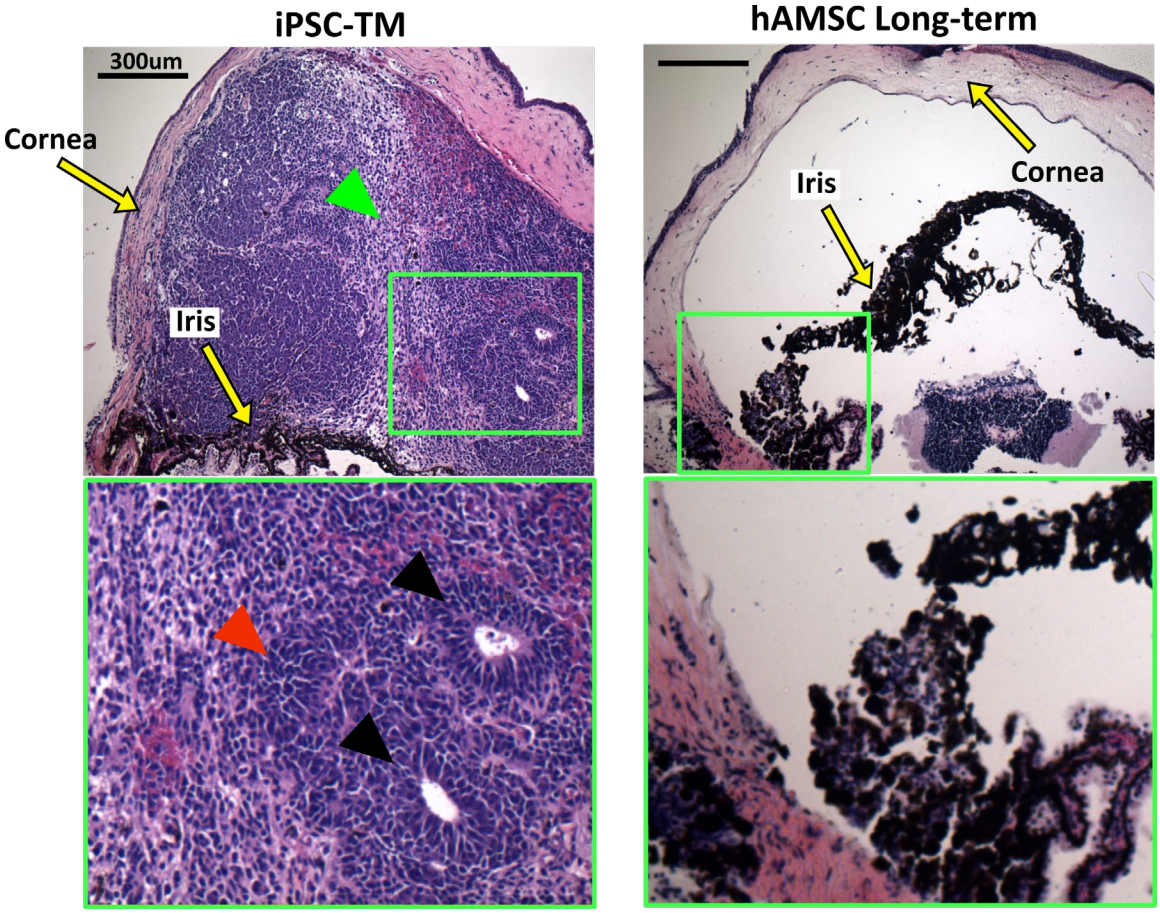


Figure 19. Histopathological assessment of tumors in eyes receiving transplanted cells. iPSC-TM- and hAMSC-transplanted eyes were stained with hematoxylin and eosin (H&E) or periodic acid–Schiff stain (supplementary Figure 44). iPSC-TM sections show distinct tumor characteristics in the anterior chamber, including the presence of rosettes (black arrowheads), a high nuclear-cytoplasmic ratio (red arrowhead), and tissue rarefaction (green arrowhead). Note that eyes were collected immediately after showing visible signs of tumor growth (usually within a month post-transplantation) and not at a pre-defined time point. B) hAMSC eyes at long-term time point showed no sign of tumor growth. In all panels, the green boxes provide a magnified view of the areas where tumor growth or the accumulation of exogenous cells occurred.

### 5.4 Discussion

The overarching goal of this study was to evaluate the effectiveness of a magnetic TM cell delivery technique we previously developed (Bahrani Fard et al., 2023). Specifically, by delivering stem cell types into the eyes of a mutant myocilin mouse model of POAG and observing the effects on IOP and aqueous humor dynamics for an extended period of

time, we wished to evaluate the potential of this treatment for eventual clinical translation (Coulon et al., 2022). We hypothesized that our highly targeted magnetic delivery approach would prove efficacious. A secondary goal was to compare the efficacy of two clinically relevant stem cell types: human adipose-derived mesenchymal stem cells (hAMSCs) and iPSCs that had been differentiated towards a TM cell phenotype (iPSC-TMs).

### *5.4.1 hAMSC delivery led to long-term IOP reduction*

Our major finding was that magnetically steered delivery of hAMSCs led to a significant and sustained lowering of IOP, which could be almost entirely explained by improved function of the conventional outflow pathway. Specifically, we saw a ~27% (4.5 mmHg) IOP reduction in eyes receiving hAMSCs vs. saline (sham) injection control eyes, which was sustained for 9 months after cell delivery. This lowering of IOP was closely related to a stable ~2.8-fold increase in outflow facility in the hAMSC treatment group vs. saline injection controls. Moreover, our measured IOPs were close to “expected IOPs” calculated from facility measurements, strongly suggesting that the majority of the IOP lowering effect after hAMSC delivery was due to an improvement in the function of the conventional outflow pathway.

### *5.4.2 There was a slight offset between measured and expected IOPs*

Despite the very close correlation between measured and expected IOPs noted above, there was a small but consistent offset between these two quantities, which may be due to several factors. First, cell delivery could theoretically cause a decrease in the rate of AH formation or an increase in the rate of uveoscleral outflow, which would lower experimentally-measured IOP. However, according to Equation 3, a change in the pressure-independent flow rate (Q) would disproportionately affect the IOP in groups with

lower facility. For example, if we conservatively assume that the 1.2 mmHg average residual (Experimental IOP - Expected IOP) was caused by a difference in inflow rate for transgenic animals vs. wild-type animals, which we used as the reference for calculating inflow rate (see Methods), the 95% confidence interval on the mean of the residuals would have been ~5 times larger than what we actually calculated. The second explanation is that the mismatch was caused by an error in rebound tonometry, for example due to tonometer miscalibration or an anesthesia-induced drop in IOP (Qiu et al., 2014). However, if we assume that all groups, including WT animals, have an experimentally-measured IOP that is artifactually lower than true IOP, the pressure-independent flow rate (Q) calculated for WT animals would incorporate this effect. Thus, when this Q is used to calculate expected IOPs for groups other than WT animals, there should not be an offset between the experimental and expected IOPs, at least for groups with facilities similar to WT animals. We therefore suggest that the most plausible explanation is an inherent difference between the transgenic and WT animals, such as in the biomechanical properties of the cornea (leading to an error in the IOP read by the tonometer), in the episcleral venous pressure, or in the amount of IOP reduction due to anesthesia.

Despite some uncertainty about the minor offset between the expected and measured IOPs, the data strongly suggests that the IOP lowering caused by stem cell therapy is mainly due to a refunctionalization of the conventional outflow pathway.

### *5.4.3 hAMSC treatment led to increased TM cellularity and reduced BMM*

One of the hallmarks of POAG is loss of TM cells (Alvarado et al., 1984), which was an early motivation for TM cell therapy as a potential treatment for this disease. We found that hAMSC delivery led to a striking 2.2-fold increase in TM cellularity 3-4 weeks after treatment vs. saline-injected controls, which showed cellularities similar to eyes from WT

mice. This increased cellularity declined somewhat by 3-4 months after cell injection, but then stabilized for up to 9 months after injection. Additionally, the increase in cellularity was strongly correlated with a decrease in IOP for pooled data from all the experimental groups. This correlation more directly highlights the potential of TM cell therapy in treating ocular hypertension, where TM cellularity is reduced and IOP is elevated (Alvarado et al., 1984). Interestingly, Alvarado et al. showed that humans at birth have ~2.3-fold higher TM cellularity compared to a 40 year-old individual, and that this cellularity reduces sharply within the first five years of life (Alvarado et al., 1984). This trend in human eye cellularity resembles, both qualitatively and quantitatively, our observations after hAMSC treatment when the ~27-month average lifespan (Graber et al., 2013) of the mouse is taken into account. Further studies of factors controlling TM cellularity after hAMSC delivery are indicated but lie beyond the scope of the current study.

Another feature of POAG is an accumulation of ECM within the juxtacanalicular tissue (Fuchshofer et al., 2003). The mechanism(s) underlying this ECM accumulation are not entirely understood. Nevertheless, increased levels of transforming growth factor-β2 (TGF-β2) in the AH of POAG patients (Tripathi et al., 1994) and its role in decreasing the activity of matrix metalloproteinases (MMPs) suggest that the abnormal ECM deposits may be due to decreased ECM turnover (Fuchshofer et al., 2003; Tamm and Fuchshofer, 2007). Thus, after detecting the significant increase in TM cellularity and reduction in IOP using hAMSCs, we wondered whether transplanted cells would also affect ECM levels in the TM. Our quantification showed that this was indeed the case: hAMSC-transplanted eyes at the mid-term timepoint had only about half the basement membrane material (BMM) under the inner wall of Schlemm's canal as seen in saline-injected control eyes. This finding is consistent with the general theme of TM refunctionalization seen throughout this study. A future study to analyze the levels of TGF-β2 in the AH as well as the ratio of

active form to proform of MMPs in hAMSC-transplanted eyes would be of interest to better understand the mechanism through which exogenous cells modulate ECM turnover.

### *5.4.4 Comparison with previous work*

Unfortunately, it is not feasible to directly compare the results of this study with those of previous studies that have successfully demonstrated the efficacy of non-magnetic cell therapy in MYOC$^{Y437H}$ mice (Zhu et al., 2017, 2016). This is due to the unexpected lack of a POAG phenotype in our transgenic mice (discussed in detail below). Yet in our study, we found a stable IOP lowering and increase in outflow facility over 9 months (corresponding to one-third of the animals' lifespan) which for the first time attests to the possible longevity of TM cell therapy. In addition, because of the targeted nature of our delivery technique, we could achieve these reported therapeutic outcomes by injecting a total of only ~1,500 cells, which is significantly lower than 50,000 cells used in previous studies (Zhu et al., 2017, 2016).

### *5.4.5 hAMSCs outperformed iPSC-TMs*

This study for the first time compared the IOP-lowering performance of hAMSCs vs. iPSC-TMs – two of the most clinically relevant cell types for future TM cell therapy (Coulon et al., 2022). Surprisingly, we found that the performance of iPSC-TMs was significantly inferior to that of hAMSCs, as quantified by several outcome measures; most notably, the IOP reduction after iPSC-TM cell delivery was only half that seen after hAMSC delivery. The beneficial effect of iPSC-TM treatment on TM cellularity was also significantly lower than hAMSC at the short-term time point (1.4-fold vs. 2.2-fold increase), although this difference declined at the mid-term time point (1.4-fold vs. 1.6-fold increase). In addition to their IOP-reducing efficacy, another major drawback of the iPSC-TMs was the high incidence of ocular tumorigenicity. More than 60% of the eyes injected with iPSC-TM cells

developed tumors, requiring termination of the experiment. A body of previous literature, including a systematic review of 1000 clinical trials involving mesenchymal stem cell transplantation, finds no incidence of tumorigenicity in tissues receiving mesenchymal stem cells, suggesting an intrinsic resistance to tumor formation once positioned in the correct niche (Lalu et al., 2012; Rodríguez-Fuentes et al., 2021). On the other hand, tumorigenicity remains a concern for iPSC-derivatives due to transfection with oncogenic factors, genetic aberrations during *in vitro* cultures, and contamination of transplants with undifferentiated cells (Lamm et al., 2016; Neri, 2019; Yamanaka, 2020). Despite following a protocol to isolate differentiated iPSC-TM cells, including using a non-integrating viral vector for transfection of reprogramming factors and a commonly-used magnetic activated cell sorting approach (Yamanaka, 2020), there unfortunately remains a chance for contamination and reprogramming of these cells post-transplantation. Interestingly, the iris is reported to be a favorable location for organ culture and tumor formation, with 5-fold faster growth compared to subcutaneous injection, and thus has previously been considered for tumorigenicity safety studies, emphasizing the importance of iPSC processing in any future treatments involving iPSC-TM cell injection into the anterior chamber (Boone and DuPree, 1968; Inagaki et al., 2022; Olson and Seiger, 1972).

### *5.4.6 Cell retention profiles differed between the two cell types*

Both cell types were detectible in the anterior chamber three weeks after injection (Figure 18B), with iPSC-TM cells tending to better integrate with the TM tissue whereas the hAMSCs mostly accumulated close to, but not within, the TM. This phenomenon, which was consistently observed, may be due to the widely-reported aggregation of mesenchymal stem cells immediately post-transplantation (Burand Jr et al., 2020) which consequently prevented them from entering the deeper aspects of the TM which are characterized by narrow flow channels. Note that exogenous iPSC-TMs more directly

contributed to increasing TM cellularity than did hAMSCs due to the better integration of iPSC-TM cells into the TM. This finding complicates the interpretation of the relationship between increased TM cellularity and IOP reduction. In addition, loss of signal in long-term *in vivo* fluorescent cell tracking is inevitable (Progatzky et al., 2013) so the fluorescent signal in Figure 18 may not be marking all the exogenous cells retained in the anterior eye.

### *5.4.7 A likely role for paracrine signalling underlying TM cell therapy*

The lack of specific hAMSC homing into the TM also provides important insight about the mechanism(s) by which these cells lowered IOP and improved aqueous humor dynamics. Several hypotheses exist as to how injected cells affect TM refunctionalization: exogenous cells can either integrate with the TM and differentiate into TM-like cells, or can promote endogenous TM cell proliferation through direct contact or through their secretome. Du and colleagues, in two studies using mice, showed that TMSCs that reach the TM co-express AQP1 and CHI3L1, indicative of their differentiation into TM cells, although quantification was not performed (Xiong et al., 2021; Yun et al., 2018). Zhu et al. reported a 114% increase in TM cellularity after iPSC-TM injection in $MYOC^{Y437H}$ mice compared to saline-injected controls, yet TM-residing exogenous cells account for only 23% of this increase (Zhu et al., 2016). This finding is consistent with several studies that report the proliferative effect of exogenous cells on the TM in terms of higher Ki-67 expression and BrdU signal, as well as an increased prevalence of Nestin+ progenitor cells (Manuguerra-Gagné et al., 2013; Zhu et al., 2020, 2016). How this proliferation is mediated, however, is a matter of controversy. In two studies, Zhu et al. showed that iPSC-TMs induce significant proliferation of both cells from the TM5 cell line (an immortalized TM cell line) or primary TM cells carrying Ad5RSV-myocilinY437H when in co-culture, yet did not when they were co-cultured in the presence of a physical (membrane) separation between

iPSC-TMs and TM cells (Zhu et al., 2020, 2016). Interestingly, Xiong et al. conducted similar experiments with TMSCs and MyocY437H primary TM cells and observed no proliferative effect with or without contact between the cells (Xiong et al., 2021). On the contrary, two studies have reported the beneficial effect of injecting conditioned media from bone marrow MSCs in hypertensive rat eyes, including a significant reduction in IOP, neuroprotection, and elevated proliferation markers in the TM (Manuguerra-Gagné et al., 2013; Roubeix et al., 2015). In our study, the significant lowering of IOP seen after delivery of hAMSCs and their accumulation near, but not within, the TM supports the notion that injected cells act upon the TM through their secretome. Thus, a proteomic comparison of the secretome of hAMSCs and iPSC-TMs may provide significant insight into their paracrine effect on TM refunctionalization.

### *5.4.8 Limitations*

The main limitation of this study was the lack of a POAG phenotype in our transgenic mouse colony. Even though $MYOC^{Y437H}$ mice have previously been shown to exhibit an elevation in IOP and a decrease in both outflow facility and TM cellularity, our colony did not show any difference in those parameters compared to WT animals. While we are not certain of the cause, it is likely that the transgene was silenced in the original breeders of this colony. Unfortunately, this only became evident after the 6-7 month wait time required for the expected onset of the phenotype. Despite the strong effectiveness of our novel TM cell therapy technique (even in the absence of ocular hypertension), the main concern is whether cell therapy would work as effectively in a glaucomatous eye. Raghunathan et al. showed that when healthy TM cells are cultured on the ECM derived from glaucomatous TM cells, they experience differential stiffening and altered expression profiles similar to the glaucomatous phenotype (Raghunathan et al., 2018). Therefore, a glaucomatous ECM may negatively impact the exogenous cells and curtail their therapeutic potential.

Fortunately, since in our study hAMSCs did not seem to need to integrate into the TM to lower IOP, they may also not be affected by glaucomatous changes in the TM. Additionally, Goldmann's equation (Equation 3) shows that the same percentage increase in outflow facility produces a greater magnitude of IOP lowering in a hypertensive eye vs. in a normotensive eye. Therefore, evaluation of magnetically-steered hAMSC cell therapy in an alternative pre-clinical glaucoma model is indicated.

In summary, this work shows the effectiveness of our novel magnetic TM cell therapy approach for long-term IOP reduction through refunctionalization of the conventional outflow pathway. The comparison between hAMSCs and iPSC-TM cells strongly suggested the inferiority of the latter cell type in this treatment paradigm, as judged by tumorigenicity and less effective IOP lowering. The localization of injected hAMSCs deep in the iridocorneal angle, but not full integration into the TM, supports the hypothesis that exogenous cells promote TM refunctionalization through their secretome. Therefore, even though the mouse model used in this study did not show a POAG phenotype, this treatment approach merits further study with the eventual goal of clinical translation.

## 5.5 Materials and Methods

### *5.5.1 Overview of experimental design*

We conducted experiments in several cohorts of mice, as follows:

- WT: wildtype hybrid mice (naïve controls)
- Tg: Tg-MYOCY437H mice, a model of POAG (see details below)
- Sham: Tg mice receiving phosphate-buffered saline (PBS, injection controls)
- hAMSC: Tg mice receiving magnetically-steered hAMSCs

- iPSC-TM: Tg mice receiving magnetically-steered iPSC-TMs

Our key outcome measures were IOP, outflow facility, TM cellularity, cell retention in the anterior segment, and ultrastructural analysis of TM ECM, with timelines as indicated in Figure 13 B. All measurements were made in *ex vivo* eyes, except for IOP, which was measured longitudinally in living mice.

After breeding and genotyping, mice were maintained to age 6-7 months, when transgenic animals were expected to have developed a POAG phenotype. We then made baseline measurements and performed stem cell (or sham) injections, and followed animals for various durations:

- Short-term: 3-4 weeks after cell injection
- Mid-term: 3-4 months after cell injection, and
- Long-term: 9 months after cell injection.

Exogenous cell retention in the anterior chamber was measured at only the short-term timepoint. This is because in our experience (data not shown) the tracer's signal was only faintly present two months after injection *in vivo,* while signal was maintained for a longer period *in vitro*, as advertised by the manufacturer. We are unsure whether this loss of signal was caused by a loss of cell integrity or by fluorescent bleaching *in vivo*. Further, due to the high incidence of tumorigenicity and inferior overall effectiveness in animals receiving iPSC-TM cells, long-term measurements as well as ultrastructural analysis were not pursued for this group. We chose to perform ultrastructural analysis for hAMSC group at the mid-term time point, as this is the longest timepoint previously studied (Zhu et al., 2017) and enables comparison with previous work.

### *5.5.2 Cell preparation*

hAMSCs were purchased commercially (Lonza Bioscience, Walkersville, MD) and were prepared for injection as described previously (Bahrani Fard et al., 2023). The cells were maintained at 37° C and 5% $CO_2$ in α-MEM supplemented by 10% FBS and 1% penicillin and streptomycin and 2 mM L-glutamine. Cells were passaged using 0.05% trypsin (25-053-CI, Corning Inc., Corning, NY) to detach cells, followed by resuspension and seeding at 5000 cells/$cm^2$ in T-25 cell culture flasks. hAMSCs at 80% confluence (passages 5 or 6) were magnetically labeled by overnight incubation with 150 nm amine-coated superparamgnetic iron oxide nanoparticles (SPIONs; SA0150, Ocean NanoTech, San Diego, CA) at 25 µg/ml, followed by inspection under light microscopy to verify sufficient SPION endocytosis. Cells were then trypsinized, resuspended by addition of cell culture media, and placed in a 1.5 ml microtube. To remove insufficiently magnetized cells, a 0.25” cubic N52 neodymium magnet was placed on the side of the tube, resulting in rapid formation of a cell pellet close to the magnet. Supernatant and non-magnetic cells were then removed.

In cells being used for exogenous cell retention studies, the cells remaining in the microtube were then labeled with the PKH26 lipophilic dye kit (Sigma-Aldrich, St. Louis, MO) according to the manufacturer’s instructions. In brief, a cell solution was prepared in the diluent component of the kit and was vigorously mixed with an equal volume of the 4 µM dye solution. After 3 minutes at room temperature, an equal volume of FBS was added to the cell solution to stop the reaction and cells were washed 3 times with cell culture media to remove any unbound dye. For all the experiments where animals received hAMSC, cells were then resuspended in sterile PBS to a final concentration of 1 k cells/µl.

Mouse iPSC-TMs have previously been developed and characterized (Zhu et al., 2016). In brief, mouse dermal fibroblasts are reprogammed through Sendai virus-mediated reprogramming with the transcription factors OCT4, SOX2, KLF4, and c-MYC. The pluripotency of reprogrammed iPSCs was confirmed using RT-PCR, immunocytochemistry, immunoblotting, and teratoma formation. iPSCs were then differentiated by culturing in conditioned media from primary human TM (phTM) cells. To prepare this conditioned media, phTM cells were extracted from donor eyes and cultured in α-MEM supplemented by 10% inactivated FBS and 2% primocin. Conditioned media was then collected from the cells and sterilized by passing through a 0.2 μm membrane filter. The iPSCs were maintained in conditioned media for 8 weeks to induce differentiation. It is important to remove any undifferentiated iPSCs from the iPSC-TM populations due to the risk of tumorgenicity associated with pluripotent stem cells. Therefore, the iPSC-TMs were incubated with CD15 antibodies (Miltneyi Biotec, Bergisch Gladbach, Germany) conjugated with magnetic microbeads to label the undifferentiated iPSCs. Then the cells were washed, loaded into a MACS LD column and were placed in a magnetic separator (Miltneyi Biotec).

### *5.5.3 Transgenic mice*

All animal procedures were approved by the Georgia Tech Institutional Animal Care and Use Committee and performed in conformance with the ARVO Statement for the Use of Animals in Ophthalmic and Vision Research. Breeder pairs of C57BL/6 Tg-MYOCY437H mice were shipped from Iowa to a quarantining facility (Charles River), underwent IVF rederivation, and were shipped to Atlanta after ~4 months. Breeders carrying one copy of the transgene on a C57BL/6 background were crossed with SJL mice (Charles River, Wilmington, MA) of similar age, with half of the hybrid offspring carrying the transgene. Pups were genotyped using human MYOC primers (forward:

CGTGCCTAATGGGAGGTCTAT; reverse: CTGGTCCAAGGTCAATTGGT). Only F1 animals were used in studies.

### *5.5.4 Cell Injections*

Cell injection needles were fabricated as described previously (Bahrani Fard et al., 2023). In brief, glass micropipettes were pulled using a pipette puller (P-97, Sutter Instruments, Novato, CA) and the tips were broken and beveled at a 30˚ on a microelectrode beveler (BV-10, Sutter Instruments, Novato, CA) followed by rotating to both sides for enhanced sharpness (tri-beveling). The resulting needle had a pointed tip and an outer dimeter of approximately 100 µm. Cell adhesion to the needle walls in the lumen can cause inconsistent cell delivery to the eye; thus, we plasma cleaned the needles, coated them with trichlorosilane and loaded them with 0.02% Pluronic F-127 (P2443, Sigma-Aldrich) for 1 hr at room temperature followed by vigorously rinsing with PBS. Needles were sterilized with 70% ethanol prior to injections.

Each animal was prepared for unilateral injection of cells by applying a tropicamide eyedrop (Bausch and Lomb, Bridgewater, NJ) to start pupil dilation before inducing anesthesia using an induction chamber receiving 2.5% isoflurane at 600 ml/min. Once toe-pinch reflex was lost, the animal was transferred to a heated bed and the head was immobilized with Velcro straps while anesthesia was maintained through a nose cone. A drop of tetracaine (Bausch and Lomb) was applied to the eye being injected while the contralateral eye received ophthalmic lubricant (SystaneUltra, Alcon, Geneva, Switzerland) to prevent drying. The needle, mounted on an injector assembly (MMP-KIT, WPI, Sarasota, FL), was attached to a micromanipulator and connected to a microsyringe pump (PHD Ultra, Harvard Apparatus, Holliston, MA). The needle was filled with 3 µl of the injection solution (either cells, or PBS for control (sham) injections), aligned at a 30°

angle with the eye, and advanced into the AC in a swift motion until the tip was located approximately in the center of the AC while the eye was held in a proptosed position using a pair of non-magnetic forceps (Figure 13 A). A total of 1.5 µl of the solution was injected at 2.4 µl/min and if the solution contained cells, a point magnet was used to magnetically steer the cells towards the TM in a continuous motion for the duration of cell ejection from the needle as previously described in detail (Bahrani Fard et al., 2023). Injected eyes received ophthalmic antibiotic combination ointment (neomycin, polymyxin, bacitracin) and were kept on a heated bed until recovery from anesthesia.

### *5.5.5 IOP measurements*

We measured the IOPs between 1 to 3 pm (to minimize diurnal variations) by first placing the mouse in an induction chamber until the righting reflex was lost and breathing slowed. The animal was then transferred to a heated platform, secured with straps, and a tonometer (TonoLab, iCare, Vantaa, Finland) mounted on a micromanipulator (M3301, WPI, Sarasota, FL) was aligned perpendicular to the corneal surface at the center of the cornea. Eight IOP measurements were taken from each eye and the reported IOP was the average of all 8 measurements. Even though some labs exclude the highest and lowest of the 8 measurements from the IOP average (McDowell et al., 2022), we did not observe a significant intra-measurement variability and thus included all the 8 replicates when determining the IOP. The entire duration of IOP measurement was typically 3 minutes or less, which is less than has been reported for the start of significant anesthesia-induced IOP reduction (Qiu et al., 2014; Tsuchiya et al., 2021).

### *5.5.6 Measurement of outflow facility*

Outflow facility, which quantifies the ease of fluid drainage from the eye, is defined as the ratio of steady-state outflow rate over intraocular pressure in an enucleated eye. We

measured facility in enucleated eyes using the previously established iPerfusion system (Sherwood et al., 2016). The system's sensors were calibrated before each measurement session to ensure reliability and the absence of bubbles or leaks, which can cause large errors in the mouse eye. Animals were euthanized by intraperitoneal injection of sodium pentobarbital and eyes were enucleated by sliding a pair of fine angled forceps behind the eye through the nasal side of the eye socket and pulling the eye out by grabbing onto the optic nerve and the surrounding retrobulbar tissues. The posterior eye was secured to a mounting post using a very small drop of cyanoacrylate adhesive (Superglue) inside a heated water bath (35°C) filled with DPBS supplemented with 5.5 mM glucose. A beveled micropipette, mounted on a micromanipulator, was then used to cannulate the eye at a 30° angle. The eyes were stabilized at an IOP of 8 mmHg for 30 minutes and then perfused at 8 evenly distributed pressure steps starting from 4.5 mmHg and finishing at 16.5 mmHg while flow rate and pressure data were acquired (Figure 15 Ai-iii). The resulting flow-pressure data were fit with an empirical power-law relationship (Sherwood et al., 2016)

$$C(P) = C_r \left(\frac{P}{P_r}\right)^{\beta} \quad (2)$$

where C is the steady-state outflow facility calculated for each pressure step, P is the steady state pressure for that step, and the subscript r refers to the parameter evaluated at the reference pressure of 8 mmHg which corresponds to the physiologic pressure difference across the conventional outflow pathway (Sherwood et al., 2016). β is a non-linearity parameter that is determined by data fitting along with $C_r$. A total of 114 eyes were randomly chosen for outflow facility measurements, of which, 9 were excluded due to failed perfusion (e.g. poor cannulation).

### *5.5.7 Comparison between experimental and expected IOP*

Steady-state AH dynamics can be described by the modified Goldmann equation (Brubaker, 2004):

$$Q = Q_{in} - Q_0 = C(IOP - P_e) \quad (3)$$

where $Q_{in}$ is the rate of AH humor formation, $Q_0$ is the uveoscleral (unconventional) outflow rate, and $P_e$ is the episcleral venous pressure. Since the left-hand side of Equation 3 is essentially pressure-independent, Q was assumed to be the same across all the experimental groups.

To cross-validate the IOP and outflow facility measurements, we calculated Q in wildtype animals by inserting the mean measured outflow facility and mean measured IOP from wildtype animals into Equation 3, assuming $P_e$ to be 7 mmHg (Sherwood et al., 2016). Average outflow facilities for all the groups were then adjusted using Equation 2 to account for the pressure-dependence of facility. Using these adjusted facilities and assuming Q to be the same for all groups, we calculated an "expected IOP" for each experimental group, which can be interpreted as the IOP that is consistent with the measured outflow facility.

### *5.5.8 Histology, histopathology, and morphometric studies*

Similar to the procedure used previously (Bahrani Fard et al., 2023), all experimental eyes were immersion fixed in 10% formalin (Fisher Healthcare, Waltham, MA) overnight at 4°C after the corresponding *in vivo* and *ex vivo* measurements (no measurements were performed on the eyes used for exogenous cell retention study). Of these eyes, a total of 59 were randomly selected from various group for TM cellularity quantifications. Eyes were then dissected under a surgical microscope and isolated anterior segments were cut into

four leaflets. This anterior segment wholemount was placed on a glass side with the cornea facing up and was sandwiched with a coverslip. A Leica DMB6 epifluorescent microscope (Leica Microsystems, Wetzlar, Germany) was used to create fluorescent *en face* tilescan images. Two quadrants of each wholemount were then prepared for cryosectioning. These quadrants received sequential 15 minute treatments in 15% sucrose (Sigma-Aldrich, St. Louis, MO), 30% sucrose, and a 1:1 solution of 30% sucrose and optimal cutting temperature (OCT) media. After embedding in OCT, samples were floated in a 100% ethanol bath cooled by dry ice to flash freeze. 10 µm-thick sagittal sections were cut using a CryoStar NX70 cryostat (ThermoFisher Scientific, Waltham, MA) and placed on superfrost gold plus slides (ThermoFisher Scientific, Waltham, MA). In an additional step specific to TM cellularity quantification, the samples were permeabilized with 0.2% Triton X-100 for 10 minutes and stained with DAPI (NucBlue fixed cell DAPI, Invitrogen, Waltham, MA) for 15 minutes followed by coverslipping with antifade media (Prolong Diamond antifade medium, Invitrogen, Waltham, MA). Sagittal sections were then imaged as tilescans.

To quantify TM cellularity, ideally all the cells in the TM should be counted. However, due to partial or complete collapse of the Schlemm's canal and the small separation between the TM and the iris in the murine iridocorneal angle (G. Li et al., 2019), identifying the boundaries of the TM can be challenging. Thus, to minimize error, we instead counted the DAPI-stained nuclei in the TM that we could identify as the TM with a high confidence and normalized this count by the length of the inner wall of Schlemm's canal adjacent to this segment (Figure 16 A). Note that morphological characteristics such as the autofluorescence in the corneoscleral shell, high degree of pigmentation in the iris, as well as the change in the density and orientation of the cells transitioning from the TM to iris helped with locating the TM cell nuclei.

Eyes of animals injected with iPSC-TMs showing anatomical signs of tumor growth were enculaeated and immersion fixed in 10% Formalin for histopathological studies. Three of these eyes were randomly chosen, dehydrated, and embedded in paraffin. Subsequently, sagittal sections were cut using a microtome and stained with hematoxylin and eosin (H&E). For periodic acid-Schiff (PAS) staining, sections were treated with a PAS staining kit. Paraffin sections were deparaffinized using xylene and a series of alcohol steps. Following an oxidation step with a 1% periodic acid solution for 10 minutes, the sections were treated with Schiff reagent in the dark for 20 minutes. Subsequently, they were rinsed under running water for 5 minutes and counterstained with hematoxylin. Finally, the sections were dehydrated using an ethanol gradient and sealed with a mounting medium. Three additional eyes from hAMSC long-term group underwent the same procedure for comparison.

### *5.5.9 Quantification of ECM underlying the inner wall of SC*

The amount of basement membrane material (BMM) in the hAMSC mid-term experimental group and in corresponding injection control eyes (four eyes in each cohort) were quantified using electron micrographs, using an approach similar to that previously described (Li et al., 2021; Overby et al., 2014). In brief, the two anterior segment quadrants not used for TM cell counting (described above) were immersion fixed overnight at 4°C in universal fixative (2.5% glutaraldehyde, 2.5% paraformaldehyde in Sörensen's buffer). The specimens were next embedded in Epon resin, and 65-nm sagittal sections were cut through iridocorneal tissues using an ultramicrotome (Leica EM UC6, A-1170; Leica Mikrosysteme GmbH) followed by staining with uranyl acetate/lead citrate. Sagittal sections were examined with a JEM-1400 electron microscope (JEOL USA, Peabody, MA) at 8000x magnification. At least one section per quadrant was included in the quantification of basement membrane material (BMM) deposits as described below.

The lengths of BMM segments directly in contact with the inner wall of Schlemm's canal (IW) and the total length of IW were measured from electron micrographs using ImageJ. The ratio of these two values were calculated, representing the extent of fenestration in the IW. Supplementary Figure 41 exhibits an example of the demarcations. Note that ECM deposits with a clear separation from the IW were not considered as BMM deposits.

### *5.5.10 Statistical analysis*

IOP, outflow facility, and TM cellularity index were tested for normality using the Shapiro-Wilk test for each treatment group. Since outflow facility is known to be log-normally distributed (Sherwood et al., 2016), facility data was first log-transformed prior to conducting any statistical tests. All outcome measures, except for TM cellularity and normalized BMM length, were analyzed by one-way ANOVA. For TM cellularity and BMM length, we used a linear mixed-effects model, treating the experimental group as the fixed effect while considering the eyes and various sections of each eye as replicates, i.e. as random effects. Following these analyses, we conducted *post hoc* comparisons with Bonferroni correction. However, we limited our comparisons to those chosen *a priori* to be relevant to the interpretation of our study to avoid an overly conservative adjustment of critical p-values as required by Bonferroni correction. To compare the impact of different treatments on IOP and outflow facility, we computed the difference between the treatment groups and their respective injection controls. Subsequently, we conducted two-tailed t-tests with Bonferroni correction. Given the log-transformation of facility data, the subtracted values became ratios upon inverse transformation. To check for consistency between IOP and outflow facility measurements, we calculated residuals as the difference between the expected and experimentally-measured IOPs. A two-tailed t-test was then performed on these residuals with $H_0$: $\mu = 0$.

# CHAPTER 6. CONCLUSIONS

Previous studies provide evidence of the promise that TM cell therapy holds as a treatment for POAG, as cell therapy has been shown to significantly lower IOP, increase outflow facility, increase TM cellularity, and provide neuroprotection in various animal models (Manuguerra-Gagné et al., 2013; Xiong et al., 2021; Yun et al., 2018; Zhu et al., 2020, 2017, 2016). Despite this evidence, significant room for improvement in terms of enhancing delivery efficiency, and thus improving treatment effectiveness and safety, is desirable and would bring this treatment closer to clinical translation. The overarching goal of this study was to develop an optimized TM cell therapy method and carefully quantify its therapeutic outcomes. To achieve this goal, two specific aims were defined and pursued: the first concerned the development and characterization of a magnetic cell delivery technique, and the second tested the efficacy of the method by comparing the function of two relevant choices of cell type in an animal model of POAG. The conclusions associated with each specific aim are summarized below.

## 6.1 Specific aim 1: Design, develop, and test a surgical approach to improve the quality of TM cell delivery in mice

The most intuitive way to deliver cells to the TM is to inject them into the AC and rely on the flow of AH to carry them to the iridocorneal angle. Yet this widely-used approach, (Xiong et al., 2021; Zhu et al., 2020, 2016) as well as more targeted delivery techniques developed later (Snider et al., 2018), result in the majority of cells being delivered off-target, rightfully raising concerns regarding the risk of side effects such as tumorigenicity and immunogenicity.

### *6.1.1 Achievements in this dissertation*

By labeling cells with SPIONs and using a magnetic apparatus with a focused force field, we developed a novel magnetic delivery technique that proved to have higher uniformity and specificity of cell delivery to the TM compared to previous methods. However, to enable the application of this technique to *in vivo* mouse eyes, sized ~400 times smaller than a human eye in volume, we had to develop a standardized surgical approach to increase the repeatability and success rate of such experiments. Our approach was to first fabricate a stereotaxic surgical platform enabling precise maneuvering of surgical and measurement equipment. Notably, this platform enabled a single operator to perform such operations compared to previous two-operator techniques (Ito et al., 2016). We coupled this surgical approach with a detailed procedure for cell preparation and injection. The performance of our proposed magnetic TM cell delivery technique using this surgical approach was quantified in terms of uniformity of cell delivery around the circumference of the TM and proximity of delivered cells to the target tissue, selected as two relevant parameters describing the avoidance of “off-target” delivery and uniformity of TM-targeted delivery. Our “point magnet” technique unequivocally outperformed the other two methods by delivering 20-times more cells 5 times closer to the TM, while the fraction of TM circumference receiving adequate cells was 10 times higher.

### *6.1.2 Expected performance of the point magnet technique in human eyes*

Even though we used mice as our animal model in this aim, motivated in part by our choice of glaucoma animal model in Aim 2, murine ocular anatomy is different than human. This naturally raises the question as to how our results will translate to human eyes. Thus, future *ex vivo* studies should be performed in human eyes to ensure that the point magnet technique is capable of high-quality cell delivery in human eyes. Nonetheless, the point

magnet technique has the advantage of much higher level of spatiotemporal control over the intraocular cell delivery compared to the other two methods, and its design allows for the incorporation of very strong magnets, whereas the ring magnet's thickness and radius (and hence its field strength) are both limited by the geometry of the eye. All these lead us to believe the point magnet will likely show satisfactory performance in larger human eyes.

Another concern may arise from the technical difficulty of performing the point magnet steering approach in human eyes. It should be noted that while point magnet TM cell delivery in mice requires a precise surgical approach and extensive training of the experimenter, in the larger human eye, TM cell therapy is expected to be less technically challenging and may be similar to cataract surgery which takes on average 15 minutes to perform (Davis, 2016).

## 6.2 Specific aim 2: Perform magnetic TM cell therapy in a standard mouse model of POAG and comprehensive analysis of the therapeutic benefits

We showed the improved performance of our "point magnet" technique in aim 1 and wanted to evaluate its therapeutic benefits in a mouse model of POAG. In particular, we were hoping that our novel treatment would lower the IOP by at least 20%, and preferable by 30% or more, which has previously been shown to be a threshold that significantly lowers the risk of disease progression in patients with ocular hypertension (Collaborative Normal-Tension Glaucoma Study Group, 1998; Heijl et al., 2002; Kass et al., 2002). Additionally, we identified mesenchymal stem cells and iPSC-TMs as the most clinically relevant cell types for TM cell therapy and a comprehensive comparison of their efficiency in reversing the course of POAG pathology was judged to be important for advancing potential clinical translation of TM cell therapy. Because of the previously reported fidelity

of the MYOC$^{Y437H}$ mouse model to the POAG phenotype (Zode et al., 2011) it was chosen as our POAG model.

### *6.2.1 Achieved in this dissertation*

After executing a complex experimental design incorporating all the above goals, we achieved a 27% decrease in IOP after hAMSC delivery vs. saline-injected (sham) controls; further, this decrease in IOP remained stable over the ~1-month, ~4-months, and 9-month time points after cell injection. This reduction in IOP was closely correlated with an increase in outflow facility, highlighting the role of refunctionalization of the conventional outflow pathway as the main factor causing the observed IOP reduction. Within the conventional outflow pathway, TM cellularity spiked to 2.2 times that of the injection control at the short-term time point after injection, but then gradually decreased to plateau at 1.6-fold higher than in control eyes at subsequent time points. The increase in TM cellularity and reduction in IOP resulting from our treatment are consistent with the potential of hAMSCs to reverse aspects of the course of pathology in ocular hypertension, where TM cellularity is reduced and IOP is elevated (Alvarado et al., 1984).

The longevity of our novel TM cell therapy, demonstrated by a sustained IOP lowering and TM refunctionalization throughout the 9-months-long course of this study (corresponding to about one-third of the mouse's lifespan), is more than twice that of the longest effect that has been previously reported (Zhu et al., 2017). Similarly, we found the injected cells to be present in the anterior chamber in large quantities three weeks after injection, while previous studies report the disappearance almost of all cells within four days of injection (Manuguerra-Gagné et al., 2013). This observation may be due to the point magnet being able to deliver injected cells more specifically to the TM (and in general closer to this tissue), which we hypothesize reduces the immunogenicity of exogenous cells and

subsequently reduces their clearance from the anterior chamber. However, as will be discussed below, investigating the safety of magnetically-steered TM cell therapy falls beyond the scope of this thesis and should be pursued in future.

Transplantation of iPSC-TM cells resulted in 13% reduction in IOP over four months, which was inferior performance vs. that seen after hAMSC delivery. TM cellularity after iPSC-TM cells was increased similarly to that seen after delivery of hAMSCs at later time points. It should be noted that injected iPSC-TMs integrated with the TM, whereas hAMSCs accumulated outside of, but in close proximity to, the TM. Therefore, exogenously injected iPSC-TMs had a higher direct contribution to the reported TM cellularity values compared to hAMSCs.

### *6.2.2 Cell homing to the TM, hAMSC secretome, and endogenous cell proliferation*

The lack of specific homing of hAMSCs into the TM in our study supports the long-debated hypothesis that these cells promote endogenous TM cell proliferation through their secretome (Manuguerra-Gagné et al., 2013; Roubeix et al., 2015). Interestingly, the antithesis, i.e. that exogenously transplanted cells need direct contact with TM cells to promote TM cell proliferation, has only been reported in studies using iPSC-TMs (Zhu et al., 2020, 2016), for which we observed a significant degree of homing to the TM. Therefore, it is possible that these two cell types have different modes of action.

It is of interest that MSC aggregates have been shown to have significant differences in their secretome, proteome, and metabolome as compared to hAMSC monolayers (Doron et al., 2020). This finding is relevant in the context of our work since we observed clumping of MSCs near the TM, perhaps due to “trapping" of these cells by the pectinate ligaments or outer TM. For example, VEGF secretion is increased by MSC aggregation, and is also known to increase outflow facility (Reina-Torres et al., 2017) and be present at decreased

levels in the AH of POAG patients (Kokubun et al., 2018). On the other hand, MSC aggregation also elevates secretion of factors known to be associated with ocular hypertension, including immunomodulatory factors such as IL-4, IL-8, IP-10, and MCP-1, which are also elevated in the AH of POAG patients (Freedman and Iserovich, 2013; Kokubun et al., 2018; Veranth et al., 2007). In particular, increased IL-8 is strongly correlated with ocular hypertension (Chono et al., 2018). Similarly, the proinflammatory cytokine IL-1α is also elevated in POAG while MSC aggregates have elevated levels of its inhibitor, IL-1ra (Volarevic et al., 2010). In addition, MSC aggregates show altered ECM synthesis pathways and lower proliferation activity compared to monolayers (Doron et al., 2020; Ito and Suda, 2014). Of particular note is the downregulation of type I collagen in aggregates which is an abundant type of collagen within TM beams and JCT (Acott and Kelley, 2008). In summary, analyzing the secretome of aggregated MSCs, rather than MSCs in monolayer, would be of interest to understanding MSC's mode of action in our studies.

### *6.2.3 Lack of disease phenotype in animal model*

A major limitation of this thesis was that the animal model of POAG we used unfortunately did not show a disease phenotype. The reason for this lack of phenotype is unknown, but it is possible that the transgene has been silenced through epigenetic changes. Two concerns stem from this issue regarding the interpretation of the results of this dissertation: first, whether this novel magnetic-steering TM cell therapy will be effective in a truly glaucomatous eye; and second, the inability to compare our current results with those of previous studies. As discussed in the Introduction, the TM undergoes significant changes in POAG and cells exposed to a glaucomatous extracellular matrix experience altered expression profiles and mechanical properties (Raghunathan et al., 2018). Therefore, if exogenous cells integrated with a truly glaucomatous TM, as did the injected iPSC-TMs

in our study, their behavior could be different than reported in mice lacking a POAG phenotype. However, as discussed, transplanted hAMSCs for the most part did not integrate with the TM and thus are less likely to be directly affected by the pathological changes of the glaucomatous TM. In addition, the extent of IOP reduction, given the same degree of increase in outflow facility, would be higher in a hypertensive eye compared to the normotensive eyes used in the current study, suggesting the possibility of even more IOP lowering of our TM cell therapy in a hypertensive eye.

Similarly, because of the possibility of variation in treatment effect between glaucomatous vs non-glaucomatous eyes, a comparison between the results of this dissertation and previous studies using hypertensive animals is not feasible. Nevertheless, one study reports that injecting hAMSCs in normotensive mouse eyes did not affect IOP or outflow facility (Zhou et al., 2020) as opposed to the significant IOP reduction we see in normotensive eyes using both hAMSCs and iPSC-TMs. This signifies the improved performance of our method compared to the study of Zhou et al., which used passive delivery of cells to the TM.

### *6.2.4 Treatment safety: tumorigenicity*

To enable clinical translation of TM stem cell therapy, additional preclinical studies are required to determine the effectiveness and the safety of any new treatment strategy. By design, the scope of this dissertation did not include a safety evaluation. However, we did observe a significant incidence of tumorigenicity using iPSC-TMs, even while employing a standard technique for separating pluripotent cells from the differentiated cell population using magnetic-activated cell sorting (Yamanaka, 2020). Several studies in the literature discuss the risk of tumorigenicity in iPSC derivatives due to the oncogenic factors used in the process of adult cell reprogramming and occurrence of genetic aberrations during

extended *in vitro* culture (Lamm et al., 2016; Neri, 2019; Yamanaka, 2020). The data on clinical trials involving iPSC derivatives is scarce and there have only been a few studies in ocular, cardiac, and spinal cord diseases and injuries (Cyranoski, 2019; Maeda et al., 2019; Mandai et al., 2017; Takagi et al., 2019). A recent systematic review of the published outcomes reports no sign of tumorigenicity in humans (Deinsberger et al., 2020).

Luckily, mesenchymal stem cells, which showed superior therapeutic outcomes in this study, are generally deemed safe and have been widely used in clinical trials without any reported incidence of tumor formation (Lalu et al., 2012; Lukomska et al., 2019; Neri, 2019; Rodríguez-Fuentes et al., 2021). In addition, our method uses a more targeted delivery method for TM cell therapy, which delivers the cells more precisely to their correct niche and more importantly uses much lower number of cells than what has been reported previously. Zhu et al., in two studies, showed a significant IOP reduction in MYOC$^{Y437H}$ mice by transplanting 50,000 iPSC-TMs in a single injection (Zhu et al., 2017, 2016) whereas we injected only 1,500 of either cell type in our study. Therefore, the TM cell therapy method developed in this study is likely to be much safer than those reported previously and merits further characterization in a more suitable model for safety studies such as non-human primates.

### *6.2.5 Treatment safety: iron oxide nanoparticles*

Another safety concern regarding magnetic TM cell therapy arises from the use of superparamagnetic iron-oxide nanoparticles (SPIONs) for cell steering. Generally speaking, SPIONs could cause toxicity by direct cytotoxicity, or by secondary mechanisms such as induction of oxidative stress, DNA damage through production of reactive oxygen species, and inflammation (Ha and J, 2006; Häfeli et al., 2009; Sadeghiani et al., 2005;

Stroh et al., 2004). In the context of our study, this toxicity can be caused by the systemic distribution of SPIONs but more likely as result of cell-encapsulated and targeted delivery.

#### 6.2.5.1 Systemic toxicity of SPIONs

Several iron oxide-based nanoparticles have been FDA-approved for systemic delivery (oral ingestion, intravenous injection), including Feridex, Gastromark, and Ferumoxytol. The latter is most relevant, since the others have been discontinued (Anselmo and Mitragotri, 2015). Ferumoxytol is FDA-approved as an iron supplement, delivered by intravenous injection in anemic patients with chronic kidney disease. It has also been used as an MRI contrast agent in several clinical trials as a less toxic alternative to gadolinium-based contrast agents (McDonald et al., 2015; Perazella, 2009). In Ferumoxytol, SPIONs are coated with polyglucose sorbitol carboxymethylether. When injected intravenously, the coating slows the release of free iron and helps to maintain a colloidal suspension, until nanoparticles are uptaken by the phagocytic cells in the reticuloendothelial system (Huang et al., 2022). Ferumoxytol has been shown to be well tolerated (even at the highest FDA approved dose of 510 mg per injection) with a serious adverse events frequency of less than 0.2% in large clinical studies (Finn et al., 2016; Provenzano et al., 2009; Schiller et al., 2014; Spinowitz et al., 2008).

Further, the safety of systemically-delivered SPIONs has been evaluated in pre-clinical models. For example, SPIONs were used to deliver growth factors to the retina (Marcus et al., 2018), where 20 mg/kg of SPIONs were injected intravenously in mice and a magnet was placed close to one eye, resulting in two-fold higher concentration of nanoparticles in this eye compared to a control with no external magnet. Histopathological analysis 18 days after injection showed no sign of damage caused by the nanoparticles. Kim et al. injected mice intraperitoneally with cobalt ferrite nanoparticles at 100 mg/kg and detected

the particles in various organs such as the brain, spleen, kidney, and liver. Even though the injection concentration was much higher than that approved for ferumoxytol at ~ 7 mg/kg (assuming an average human weight of 70 kg) they found no sign of toxicity or mutagenic potential after comprehensive evaluation (Kim et al., 2006). In view of the small amounts of SPIONs delivered into the eye in our approach, we therefore have few concerns about systemic toxicity.

Even though most of the concern regarding the toxicity of SPIONs revolves around their iron oxide content, we must also consider the effects of particle coating. The nanoparticles used in our study (SA0150, OceanNanotech) have an outer layer of $SiO_2$ with amine functional groups (Weerasuriya et al., 2021) vs. the polysaccharide coating used in Ferumoxytol,. Silica is generally considered biocompatible and amine-coated $SiO_2$ nanoparticles have shown no sign of toxicity even after intravenous injection at an extremely high concentration of 450 mg/kg (Murugadoss et al., 2017; Yu et al., 2012). Further, in contrast to Ferumoxytol, where the polysaccharide coating is designed to degrade once phagocytosed in the target tissues, silica nanoparticles do not generally have a fast biodegradation rate, unless they are specifically modified. Although OceanNanotech does not provide the specifics of their coating material or its biodegradation rate, they report a generally low iron exposure for their particles. Therefore, the SPIONs used in our study do not raise significant safety concerns due either to the coating material itself or the acute release of iron oxide.

#### 6.2.5.2 SPION toxicity after cell encapsulation

Despite the systemic safety of iron oxide nanoparticles, their application in cell tracking differs in two ways. First, concern arises regarding a possible toxic effect of free iron in the labeled cells (for example, if the cells were overloaded with SPIONs during labeling). A

second relates to potential toxicity of SPION leakage from labeled cells into small volumes of surrounding tissue.

Studies have reported an absence of iron oxide cytoxicity *in vitro* at concentrations below 100 µg/ml (Singh et al., 2010). The genotoxic effect of iron oxide nanoparticles has been less systematically evaluated. Such data is particularly scarce for ferumoxytol although the official safety datasheet provided by the FDA reports no evidence of mutagenic or clastogenic activity, either *in vitro* or *in vivo* (United States Food and Drug Administration, 2015). Since we use only 20 µg/ml of SPIONs to label cells for our magnetic TM cell therapy, injected cells are unlikely to experience cytotoxicity.

The effect of SPIONs on surrounding tissues after cell transplantation is harder to determine due to the variation and uncertainty about concentration and distribution pattern of these particles *in vivo*. Fortunately, several studies exist in which cells labelled with SPIONs were transplanted *in vivo*, employing much higher concentrations than we use, and reporting no toxicity or inflammation. The most relevant is a preclinical study by Gutova et al. which resulted in FDA approval for investigational clinical use of ferumoxytol to label neural stem cells for subsequent MRI tracking after transplantation into brain tumors (Gutova et al., 2013). They report that the labeled neural stem cells primarily localized within the hemisphere of the mouse brain where they were originally injected and showed no negative impact on cell viability and growth kinetics of the native tissue. They injected 250,000 cells incubated in a solution containing ~100 µg/ml iron oxide into one hemisphere of the mouse brain. This can be contrasted with our protocol, where we injected only 1,500 cells incubated in a solution containing 20 µg/ml SPIONs into the mouse anterior chamber. Assuming a volume of 210 $mm^3$ for one mouse brain hemisphere (Kovacević et al., 2005) and 7 $mm^3$ for the mouse anterior chamber (Zhang et al., 2002),

the concentration of iron oxide in the target tissue in the study of Gutova et al. study would be estimated to be 28 times higher than in ours.

The safety of neural stem cells labeled with iron oxide nanoparticles on brain tissue *in vivo* has also been shown in other studies (Kim et al., 2016; Thu et al., 2012). In another *in vivo* study, 300,000 mesenchymal stem cells were labeled with ferumoxytol at a final iron concentration of 10 mg/ml and were implanted in surgically-created 5x5x5 mm cartilage defects in pig knee (Suryadevara et al., 2023). The authors saw no difference between cartilage regenerative capacity in labeled vs. non-labeled preparations, indicating that the iron oxide labeling did not have a negative effect on the surrounding tissue. The safety of iron oxide nanoparticles for cell tracking has similarly been shown in rats using Schwann cell transplantation for spinal cord injury (Dunning et al., 2006) and intracoronary infusion of cardiosphere-derived stem cells (Vandergriff et al., 2014).

In summary, previous studies suggest that SPIONS, at suitable concentrations, are safe for cell labeling and cell therapy. Given the dose-dependent toxicity of these particles and considering the significantly lower dose used in our TM cell therapy approach vs. some of the abovementioned studies, our treatment is judged to be unlikely to lead to toxic effects due to SPIONs.

### *6.2.6 Future work*

As has been discussed in this chapter, this work highlights several potential avenues for future study to better understand TM cell therapy in terms of the underlying mechanisms, effectiveness in a glaucomatous eye, safety, and clinical translatability.

#### 6.2.6.1 Treatment effectiveness in a hypertensive animal model of POAG

The lack of a disease phenotype in our animal model casts uncertainty on the effectiveness of our magnetic TM cell therapy in a truly glaucomatous eye. The lack of a well-characterized POAG animal model with high fidelity to the disease is in general a major hurdle in the field of glaucoma research. Recently, a new version of the myocilin mutant mouse has been introduced, where the mice undergo transient transfection with the myocilin transgene using an adenoviral vector (Wang et al., 2022). Since the transfection has to be renewed for each litter, this model eliminates the risk of epigenetic silencing which has likely caused the failure of our transgenic animal model. Therefore, future studies can repeat parts of the experimental design performed in this study using this animal model in order to ensure our TM cell therapy is also effective in a hypertensive eye. In particular, injection of hAMSCs would be of interest and the resulting effect on IOP can be monitored at the three time points used in this dissertation (short-, mid-, and long-term) to allow direct comparison in between the two studies. As an additional benefit, the mid-term time point is the same as that used in previous studies (Zhu et al., 2017, 2016) as another reference of comparison.

#### 6.2.6.2 Safety studies

Safety evaluation of magnetic TM cell therapy falls beyond the scope of this thesis, yet future studies of safety are warranted. Such studies could use an animal model with an immune system and ocular physiology more similar to humans, such as non-human primates. Safety studies can include overall signs of irritation such as hyperemia or corneal cloudiness (which were absent in the treated mice in this thesis), slit-lamp exam to visualize potential inflammation inside the anterior segment, and fundoscopy to ensure the lack of any damage to the posterior segment structures such as retinal detachment or vitreous hemorrhage. All these tests can be performed *in vivo* and be documented over several time points to be inclusive of both transient and long-term potential abnormalities

caused by the magnetic TM cell therapy. *Post mortem* histopathological analysis at various time points of both the anterior and posterior segments at various time points will also be necessary to look for the presence of immune cells or anatomical changes in the eye. The tumorigenicity of the delivered cells can be evaluated similarly to the approach taken in this thesis.

As discussed, another safety concern with magnetic TM cell therapy arises from the potential cytotoxicity of the iron oxide nanoparticles. The local toxicity in the eye can be traced by Prussian blue staining of the anterior segment histological sections (as done in this thesis for mice) and by looking for signs of lesions and tissue necrosis. In systemic circulation, liver and spleen (tissues with high resident macrophage population) can similarly be investigated for signs of nanoparticle toxicity.

We recommend that future studies use Ferumoxytol, the only currently FDA-approved SPION, for magnetic TM cell therapy. The established safety profile of Ferumoxytol will help address concerns regarding SPION toxicity.

#### 6.2.6.3 Performing point magnet delivery technique in human eyes

Our magnetic TM cell delivery technique was tested in mice, which have some differences in ocular anatomy as compared to humans, as well as having much smaller eyes than humans. Further, previous studies have not performed TM cell delivery in intact human eye globes. Therefore, delivering TM cells in *ex vivo* human eyes using the point magnet approach would be important to ensure that the superior delivery quality observed in mice is translatable to human eyes. Even though *ex vivo* eyes lack AH flow, our point magnet delivery technique should be unaffected as it does not rely on the hydrodynamic forces of AH to deliver the cells to the TM. Note that this potential future study does not need to repeat the cell delivery using no magnet and ring magnet techniques, as the delivery

quality parameters introduced in this dissertation (off-target index and circumferential adequacy ratio) can be interpreted independently of any control group.

To perform TM cell therapy in human eyes, the concentration and total number of injected cells used in this work need to be scaled up accordingly. We suggest that the volume of TM in mouse vs. human is a reasonable first estimate for a scaling factor. To compute this scaling factor, we use the following dimensions for a mouse eye: a cross-sectional TM area of $137 \times 8\ \mu m$ and a limbal diameter of $2.3\ mm$ (Safa et al., 2023). Similarly, for a human eye we use a cross-sectional TM area of $350 \times 100\ \mu m$ and a limbal diameter of $13.6\ mm$ (Abass et al., 2018; Hogan et al., 1971). The volumetric ratio of human to mouse TM volume is then computed as 189, suggesting the total number of cells needed for a human eye to be about 283,000 (vs. 1,500 cells for mouse). This is similar to the number of cells used by Snider et al. in a porcine perfusion model (250 k cells injected at 1k cell/µl), which is comparable in size to a human eye (Snider et al., 2018).

#### 6.2.6.4 Improving the purification of iPSC-TMs

The iPSC-TMs used in our study resulted in significant tumorigenicity even though standard iPSC reprogramming, differentiation and separation protocols were employed. We only used SSEA-1 (CD15) specific antibodies for magnetic separation of undifferentiated iPSCs in this study, and the use of multiple antibodies can increase the efficiency of purification. Previously anti-CD30 antibody has successfully been used for targeting undifferentiated pluripotent stem cells (Sougawa et al., 2018) and their subsequent separation.

### *6.2.7 Final words*

In this dissertation, an optimized magnetic TM cell therapy was developed which in preclinical settings suggested significant therapeutic potential of magnetically-steered mesenchymal stem cells in alleviating ocular hypertension. The findings and the future directions discussed can help with the realization of TM cell therapy as a next generation treatment for glaucoma.

# APPENDIX A. A PROPOSED TECHNIQUE FOR DETERMINING "QUASI-INSTANTANEOUS" OUTFLOW FACILITY

Parts of this appendix have previously been presented at the Trabecular Meshwork Society Annual Meeting 2021. The proceedings of this meeting were not published.

## A.1 Problem statement and goal

Measurement of facility by *ex vivo* laboratory perfusion uses steady-state data; i.e. outflow facility is calculated as steady inflow rate divided by steady IOP. This approach is suitable since inflow rate equals outflow rate at steady state in an enucleated eye. However, by definition this approach is unable to detect transient facility changes as IOP is changed. Here we seek to develop a methodology to accurately determine aqueous outflow facility during the eye's transient response to a pressure disturbance. The ability to make such measurements would enable direct study of the eye's rapid homeostatic mechanisms for IOP control.

## A.2 Methods

### *A.2.1 General equations*

Our approach uses a mathematical model of the eye and the attached perfusion system to predict the eye's transient response to changes in perfusion pressure during a facility measurement experiment. Here we describe this model. The methodology we use is based on the studies by Sherwood et al. (Sherwood et al., 2019, 2016) and the reader is encouraged to review those articles for further introductory materials and details. In brief, we use the equivalence between electrical current flow and fluid flow to formulate the governing equations. Figure 20 shows the equivalent electrical circuit for the iPerfusion

system attached to an eye. The governing equations of this circuit model the system behavior at any given time, including the outflow facility.

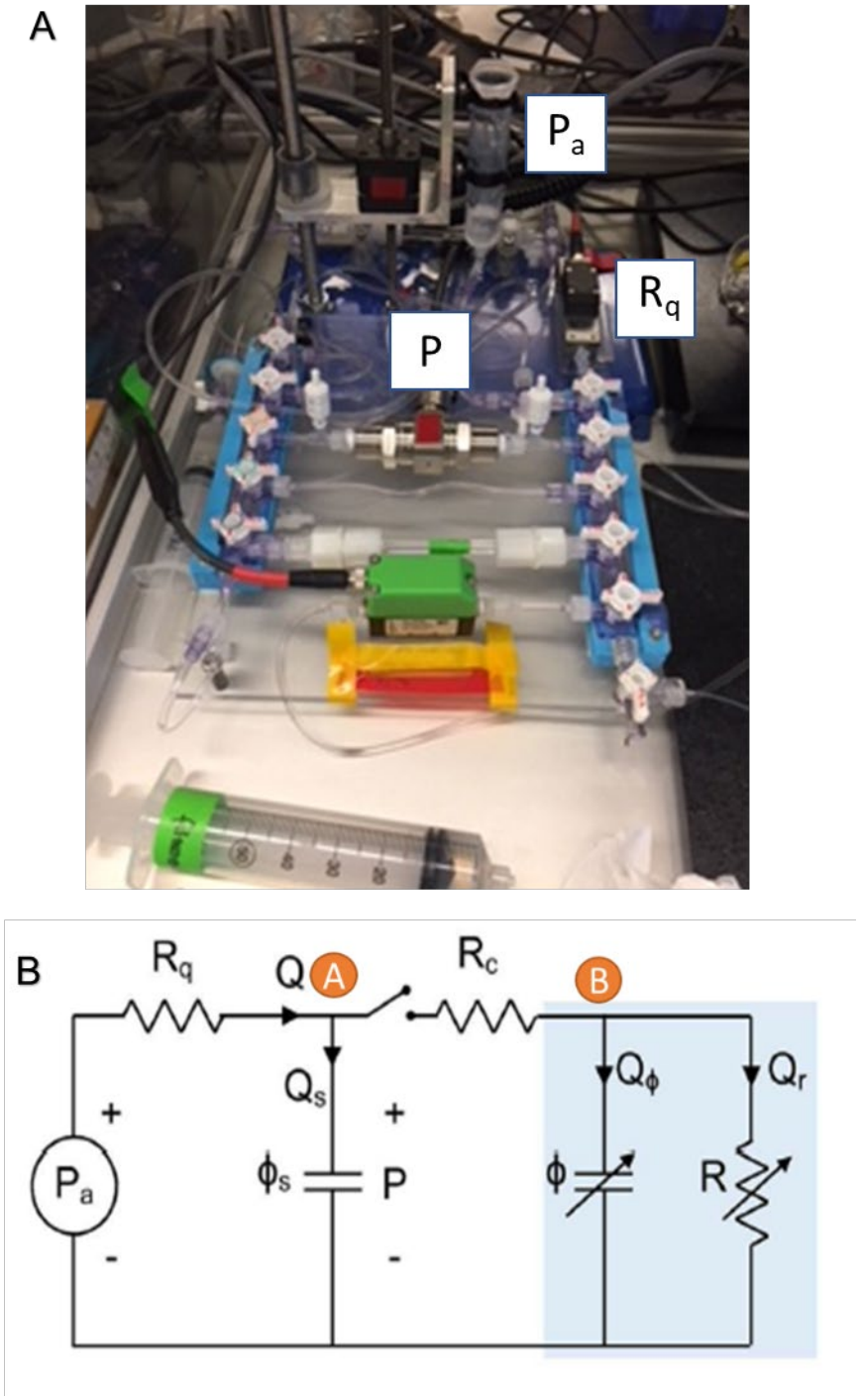


Figure 20. Photo of the iPerfusion system used for facility measurements (A) and its equivalent electrical circuit (B) (Sherwood et al., 2019, 2016). Major components of the

lumped model are labeled on the photo of the system. For a description of various parameters refer to text.

To derive the governing equations, we write Kirchhoff's law of currents (conservation of mass) for the nodes A and B shown in Figure 21. Writing currents for node (A):

$$C_q(P_a - P) - \phi_s \frac{dP}{dt} - C_c(P - IOP) = 0 \tag{4}$$

Note that the term $C_q(P_a - P)$ can be replaced by the flow sensor reading ($Q$). For node (B):

$$C_c(P - IOP) - \phi_{eye} \frac{d(IOP)}{dt} - C_{eye}\, IOP = 0 \tag{5}$$

In combination, Equations 4 and 5 form the governing equations of the circuit depicted in Figure 20. In these equations, $C_q$ and $C_c$ are conductances of flow sensor and the needle, respectively, $\phi_s$ denotes system compliance, $\phi_{eye}$ is ocular compliance, $P$ is the pressure sensor reading, $P_a$ is the applied pressure from the fluid column, $IOP$ is intraocular pressure and $C_{eye}$ is outflow facility. From Equation 4 IOP can be calculated by:

$$IOP = P - \frac{Q}{C_c} + \frac{\phi_s}{C_c}\frac{dP}{dt} \tag{6}$$

And the time derivative of IOP becomes:

$$\frac{d(IOP)}{dt} = \frac{dP}{dt} - \frac{1}{C_c}\frac{dQ}{dt} - \frac{\phi_s}{C_c}\frac{d^2P}{dt^2} \tag{7}$$

An alternative to analytically calculating the time derivative of IOP is numerical differentiation of the IOP signal, obtained directly from Equation 7.

To simplify and reduce the amount of noise in calculations, we consider the situation in which the needle resistance is much smaller than the flow sensor resistance, so that needle resistance can be neglected. Thus, points A and B will "merge" and we obtain a single governing equation:

$$Q = (\phi_s + \phi_{eye}) \frac{dP}{dt} + C_{eye}\, P \tag{8}$$

Please note that $\phi_{eye}$ and $C_{eye}$ are both non-constant, i.e. they depend on $P$ and $t$.

### *A.2.2 Instantaneous linear fitting*

Since we have 1 equation with two unknowns, we need to find a way to separate these two variables. To do so, we restructure Equation 8 as:

$$k_2 = k_1 C_{eye} + \phi_{eye} \tag{9}$$

$$k_1 = \frac{P}{dP/dt} \tag{9a}$$

$$k_2 = \frac{Q}{dP/dt} - \phi_s \tag{9b}$$

Although $\phi_{eye}$ and $C_{eye}$ are not constant in Equation 9, if we consider a short interval, their variations can be neglected. Therefore, by plotting $k_2$ vs. $k_1$ we expect to obtain a graph with outflow facility as the slope and ocular compliance as the y-intercept.

Equation 9 is derived using the assumption that needle resistance is negligible compared to flow sensor resistance. However, if this were not the case, Equation 5 could be rewritten as:

$$\frac{(P - IOP)C_c}{\frac{dIOP}{dt}} = C_{eye}\frac{IOP}{\frac{dIOP}{dt}} + \phi_{eye} \tag{10}$$

While we used no assumptions to derive Equation 10, other than those inherent in the electrical-fluid analogy, we now make three assumptions to simplify our fitting approach.

1. From Equation 4 we have $(P - IOP)C_c = Q - \frac{dP}{dt}\phi_s$. Our calculations show that the term $\frac{dP}{dt}\phi_s$ is in most cases negligible compared to $Q$, and we ignore it.

2. In most cases, the difference between $IOP$ and $P$ is small (less than 5% difference). As a result, $IOP$ can be replaced by $P$.

3. In Equation 7, $\frac{\phi_s}{C_c}\frac{d^2P}{dt^2}$ can be neglected compared to $\frac{1}{C_c}\frac{dQ}{dt}$.

As a result of these simplifications, Equation 10 becomes:

$$k_{2N} = k_{1N}\, C_{eye} + \phi_{eye} \tag{11}$$

$$k_{2N} = \frac{Q}{\frac{dIOP}{dt}} \tag{11a}$$

$$k_{1N} = \frac{P}{\frac{dIOP}{dt}} \tag{11b}$$

$$\frac{dIOP}{dt} = \frac{dP}{dt} - \frac{1}{C_c}\frac{dQ}{dt} \tag{11c}$$

The “N” subscript in these equations signifies the inclusion of needle resistance in the derivations. In the following sections, we apply Equation 9 to a sample experimental data set. Equation 11 is similarly applied to an experimental data set and the results are documented in supplementary information.

### *A.2.3 Validation with system compliance*

One way to validate our proposed methodology is by perfusing a compliant chamber with no outflow, which allows us to set $C_{eye} = 0$. Experiments in which we measure iPerfusion system compliance are suitable: we close all outflow routes and perfuse the tubing of the system. If our approach is correct, the values for system compliance should be the same as those computed by the discrete volume method (Sherwood et al., 2019). In such an experiment, Equation 8 can be rewritten as:

$$\phi_s = \frac{Q}{\frac{dP}{dt}} \tag{12}$$

By calculating $Q$ and $dP/dt$, system compliance can be calculated.

Unexpectedly, we noticed a non-zero flow rate on the order of 5 nl/min in the steady state region of the data collected from a system compliance experiment, which we suspected was due to a small leak or to limitations of the flow sensor. A leak would unpredictably complicate the calculations. To simplify, we assumed that this residual flow rate was an artifact of flow sensor uncertainty ($\pm 4\ nl/min$) and accounted for it by subtracting the measured average steady state flow rate ($Q_{offset}$) from the entire dataset. These

compliance values were then compared with those calculated using the volume filling approach (Sherwood et al., 2019).

### *A.2.4 Derivative calculations and data sampling*

To use the above equations, we must calculate derivatives of $Q$ and $P$ with respect to time, which we do numerically. Specifically, we use a simple first order differencing scheme, i.e. the difference between two subsequent samples is divided by the time interval between the samples.

An eye from a wild type C57BL6 mouse eye was perfused at several pressure steps of size 2.5 mmHg, starting from 5 mmHg to 17.5 mmHg, followed by downward steps back to 10 mmHg (Table 3). The first step is not considered for further analysis following the original methodology developed for iPerfusion system (Sherwood et al., 2016). Figure 21 and Figure 22 show representative flow rate and pressure time-traces. A Savitzky-Golay filter with first order regression was used to smooth $P$, $Q$, and $dP/dt$ (Figure 23). The length of the filter was 0.6 seconds which corresponded to 12 data points. The filtered data, shown as a blue curve in all figures, adequately follows the general trend of the unfiltered data without any shifts or attenuation. The data during actuator movement in each step was excluded from calculations due to a high degree of vibrational noise.

Table 3. Applied pressure steps used in perfusing a representative eye.

| Step No. | Pressure (mmHg) |
|---|---|
| 1* | 5 to 7.5 |
| 2 | 7.5 to 10 |
| 3 | 10 to 12.5 |
| 4 | 12.5 to 15 |
| 5 | 15 to 17.5 |
| 6 | 17.5 to 15 |
| 7 | 15 to 12.5 |
| 8 | 12.5 to 10 |

* Step 1 is not considered for further analysis according to an established protocol (Sherwood et al., 2016).

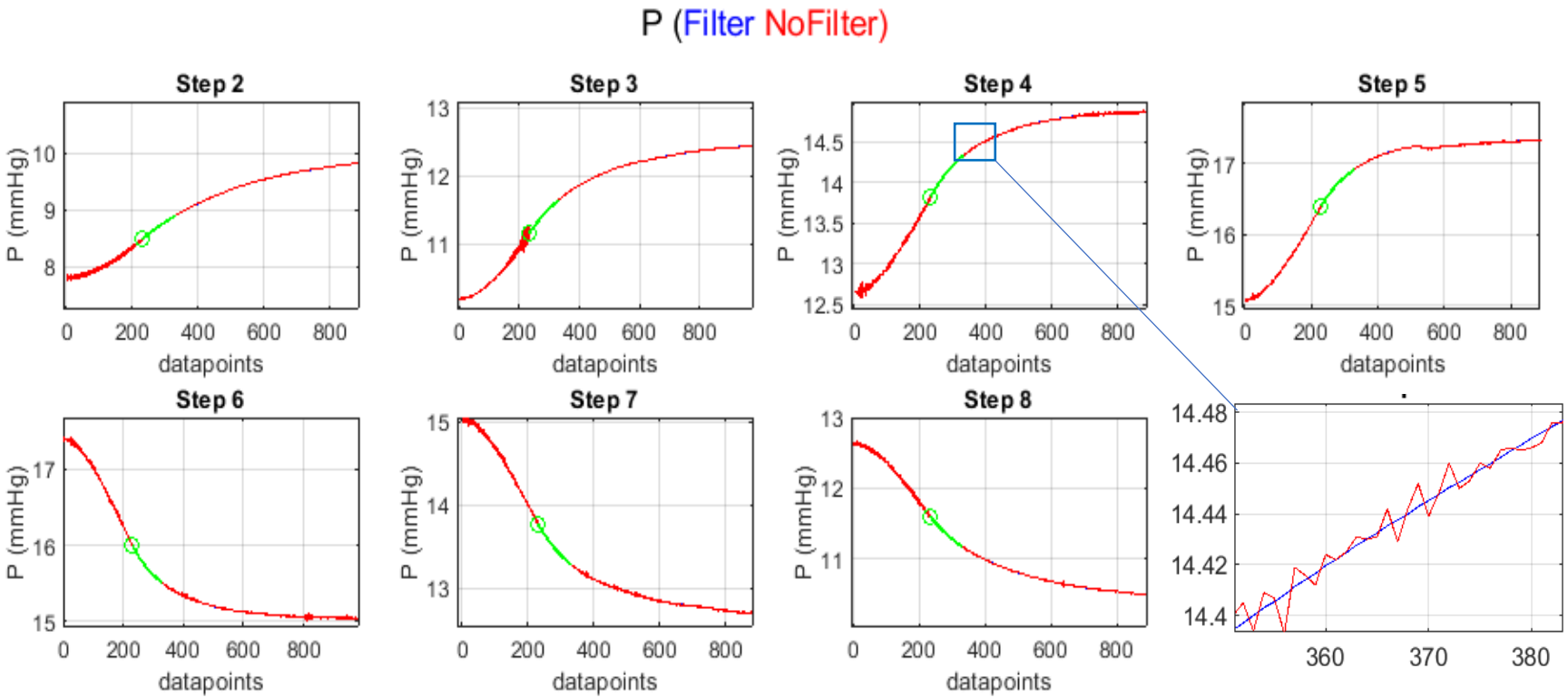
P (Filter NoFilter)
Step 2
Step 3
Step 4
Step 5
Step 6
Step 7
Step 8
P (mmHg)
datapoints

Figure 21. Pressure vs. time plots for a perfusion experiment, with data points collected at 20 Hz. Applied pressure steps are listed in Table 3. Green shows the small interval of data chosen for further analysis, so as to satisfy the assumptions of approximately constant ocular compliance and outflow facility. The small box shows a zoomed-in region to magnify the filtered vs. non-filtered data. Data point zero in this graph and in subsequent figures is the instant when the actuator began to move, as determined by the output voltage from the actuator. Similarly, the green circle shows when the actuator stopped moving. The x-axis can be converted to elapsed time by knowing the data point acquisition frequency, i.e. 20 Hz.

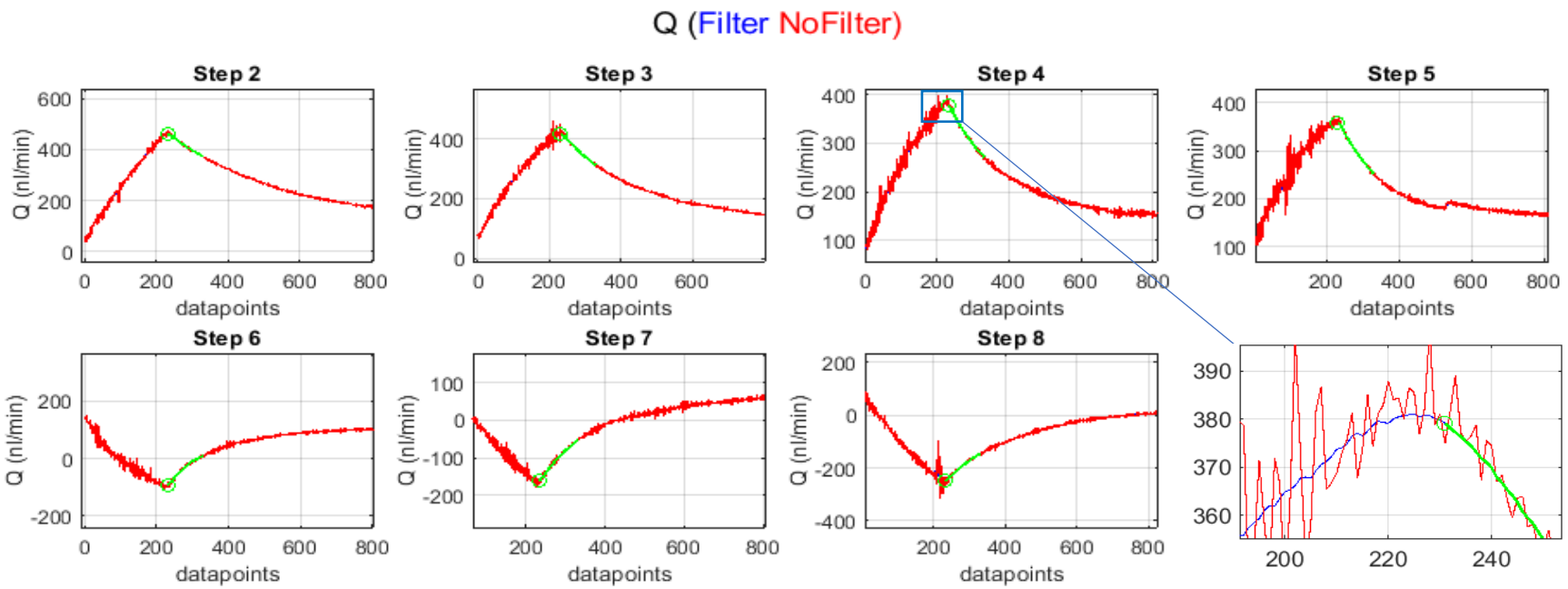
Q (Filter NoFilter)
Step 2
Step 3
Step 4
Step 5
Step 6
Step 7
Step 8
Q (nl/min)
datapoints

Figure 22. Flow rate vs. time plots for each pressure step shown in Figure 21. Refer to the caption of Figure 21 for an explanation of the different colors in the graphs and other details.

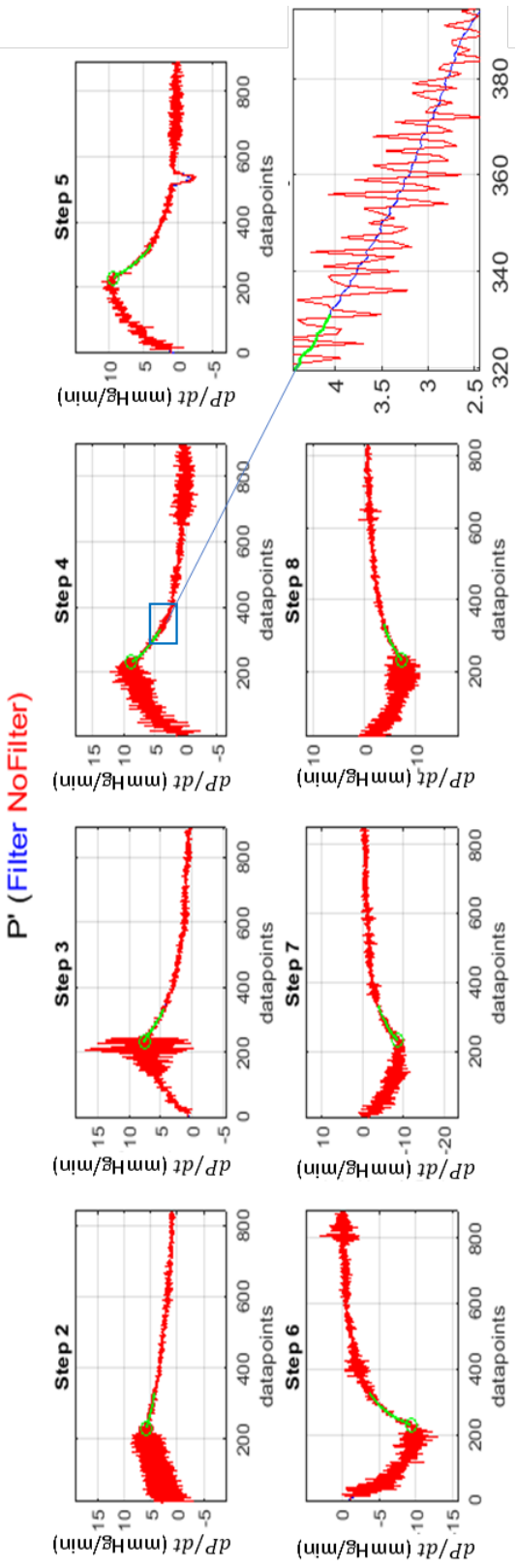
P' (Filter NoFilter)
Step 2
Step 3
Step 4
Step 5
Step 6
Step 7
Step 8
dP/dt (mmHg/min)
datapoints

Figure 23. Plots of the time derivatives of pressure corresponding to the steps shown in Figure 21. Refer to the caption of Figure 21 for an explanation of the different colors in the graphs and other details.

### *A.2.5 Instantaneous compliance calculation*

To determine ocular compliance over time we can rearrange Equation 9 to write:

$$\phi_{\mathrm{eye}} = \mathrm{k}_2 - \mathrm{k}_1 \mathrm{C}_{\mathrm{eye}}$$

$C_{eye}$ was taken as the value of the slope of the fitted line in Equation 9 and used to calculate the instantaneous compliance for each data point, $\phi_{\mathrm{eye}}$.

## A.3 Results

### *A.3.1 Validation by measuring system compliance*

A system compliance experiment, as described above, was used to validate the methodology we developed here. Figure 24 shows the resulting plots from the instantaneous compliance calculation method and discrete volume method (bold black equations on each plot).

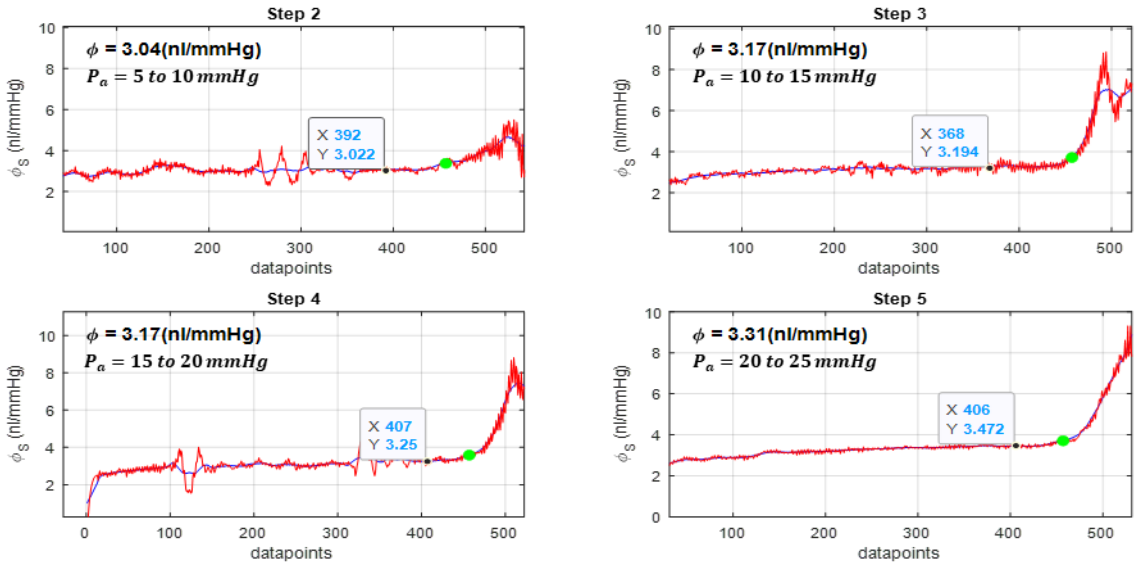


Figure 24. System compliance calculated using the instantaneous method for each pressure step of a system compliance experiment. Compliance values in bold black text were calculated using the discrete volume method (Sherwood et al., 2019). Selected data points show the compliance value at a representative data point. Green filled circle shows where the actuator stopped. $P_a$ = applied pressure at each step.

The system compliance values calculated after the end of actuator movement were found to be unstable with a steep upward trend. This indicates the inability of our governing equations to capture the dynamics of the system and is likely due to a small leak in the system, as discussed earlier. During the movement of the actuator, however, we obtained much more stable estimates of ocular compliance which were close to the values calculated using the discrete volume method. Since the temporal derivatives of flow rate and pressure are both large during actuator movement, the effect of any small leakage during this phase is less important, which may explain the more stable compliance estimates we obtained during actuator movement. These experiments should be repeated in the future after fixing the leakage or mathematically accounting for it.

### *A.3.2 Instantaneous outflow facility plots*

Equation 9 was fitted to the 5 seconds (100 datapoints) of the data immediately after the actuator stopped moving over a number of pressure steps (see Figure 21 to Figure 23; note that $R_c$ was negligible compared to $R_q$ for this experiment). Figure 25 shows plots of $k_2$ vs. $k_1$ and the corresponding fitted equations, where the slope is the instantaneous outflow facility and the y-intercept is the compliance. In step 3, for example, $C_{eye} = 12.7\ \frac{\frac{nl}{min}}{mmHg}$ and $\phi_{eye} = 32.8 \frac{nl}{mmHg}$. The calculated $R^2$ indicates the goodness of fit and is an indication of the validity of our assumptions that, over such short intervals, compliance and outflow facility are approximately constant.

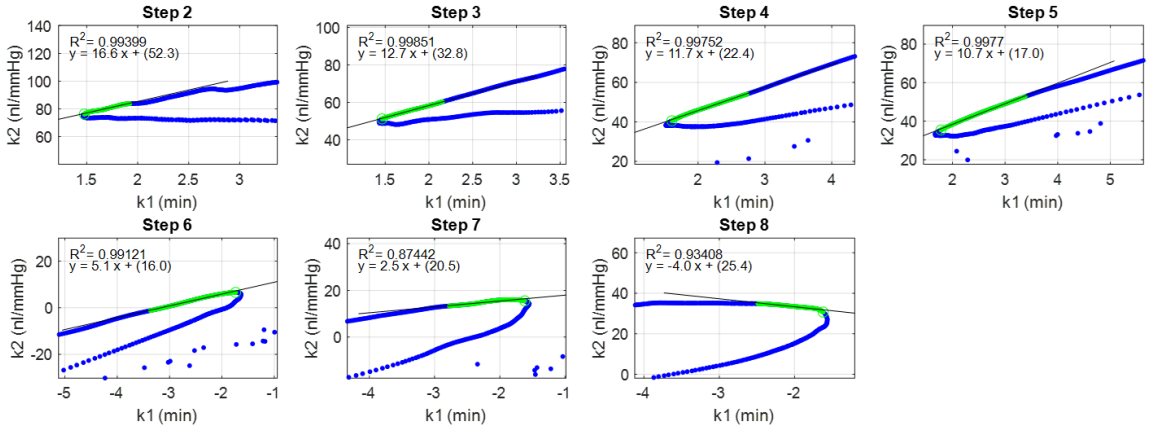


Figure 25. Plot of $k_2$ vs. $k_1$ according to Equation 9. The green region is the interval chosen for linear fitting (100 data points). The slope of the graph in the green region is the instantaneous outflow facility, while the y-intercept of the regression line (black line) is ocular compliance.

### *A.3.3 Instantaneous compliance*

Using the values of $C_{eye}$ derived in Figure 25, instantaneous compliance was calculated (Figure 26).

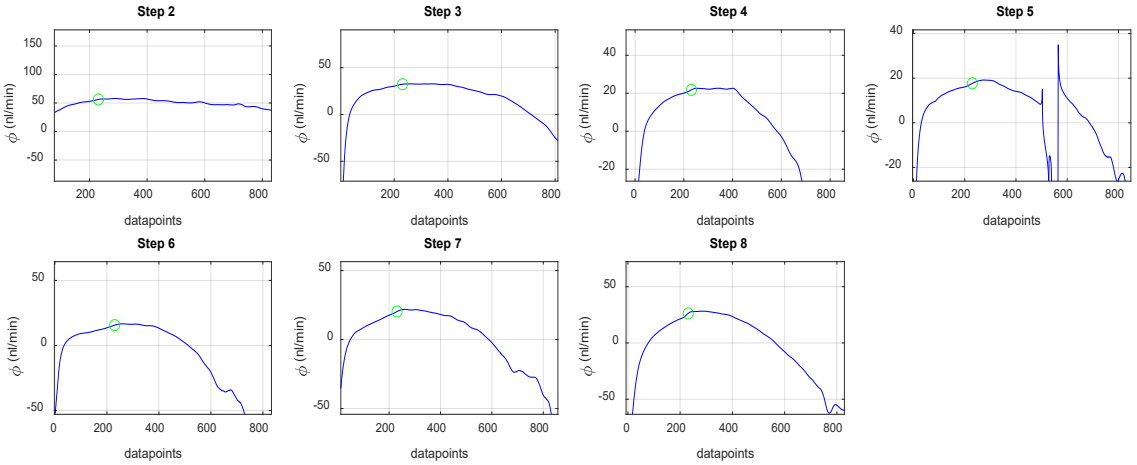


Figure 26. Instantaneous ocular compliance at different pressure steps. Green circles denote the data point where the actuator stopped moving.

The calculated compliances immediately after actuator stoppage seem to be within a reasonable range as compared to those calculated previously (Zhu et al., 2021). Two notable trends can be observed in the point-wise compliance plots. First, the estimate of instantaneous compliance decreases steeply with time, even reaching negative values. This variation in compliance is unphysical, and is likely because the time derivative of pressure in the denominator of equation 9 decreases with time and results in increasingly inaccurate estimates. Second, the compliance plots are flatter at lower pressure steps, which occurs because the system (including the eye) has a shorter time constant at higher pressures and thus reaches smaller pressure derivatives quicker.

### *A.3.4 Comparison between transient and steady-state outflow facilities*

Figure 27 shows the transient (calculated by Equation 9) and steady-state outflow facilities. At some pressures, two values for outflow facility can be observed because increasing and decreasing pressure steps were analyzed in this dataset.

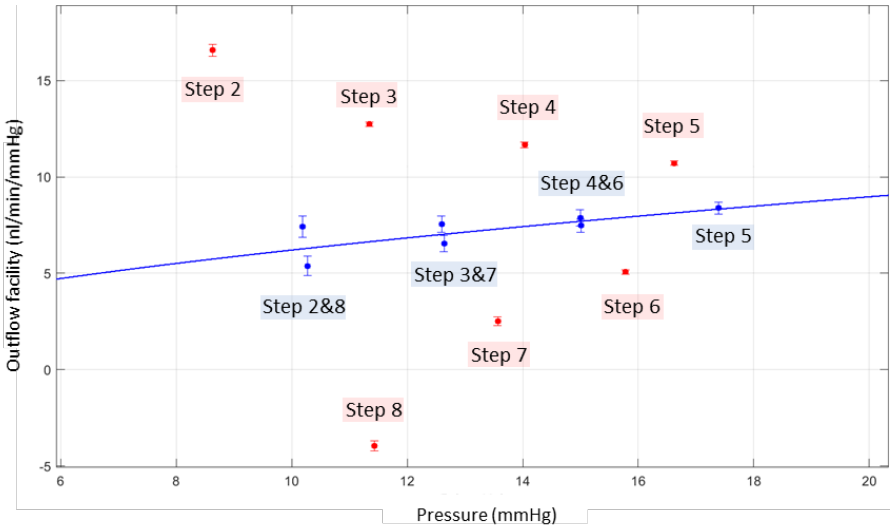


Figure 27. Transient and steady-state outflow facilities. Each point corresponds to the facility computed at one pressure step. Red points are the instantaneous facilities (calculated by Equation 9) and blue points are the steady state facilities. A negative outflow facility is unphysical and erroneous. Error bars show 95% confidence intervals on the mean, calculated using regression error for unsteady values and using error propagation according to established methods (Sherwood et al., 2016) for steady values. Pressure values are assigned to the red data by averaging over the green interval in Figure 21.

Notably, the instantaneous (transient) outflow facility is higher than the steady-state facility in increasing pressure steps, while the opposite is true for decreasing pressure steps. This behavior is consistent with the existence of an ocular homeostatic response to rapid pressure variations; such a response would quickly increase outflow in response to an IOP increase and reduce outflow in response to a sudden decrease in IOP.

A negative outflow facility, calculated for the last pressure step in Figure 27, is physically unfeasible. Interestingly, this step also exhibits a low $R^2$ value, suggesting a potential error due to a poor fit. The reason for the poor fit in decreasing pressure steps requires further investigation.

## A.4 Supplementary

### *A.4.1 Additional time traces*

Additional plots for the data analyzed in this report are provided here. These figures were helpful in understanding the behavior of individual parameters at various time points in the pressure transient.

Figure 28 and Figure 29 show plots for $k_1$ and $k_2$ vs. time for each pressure step.

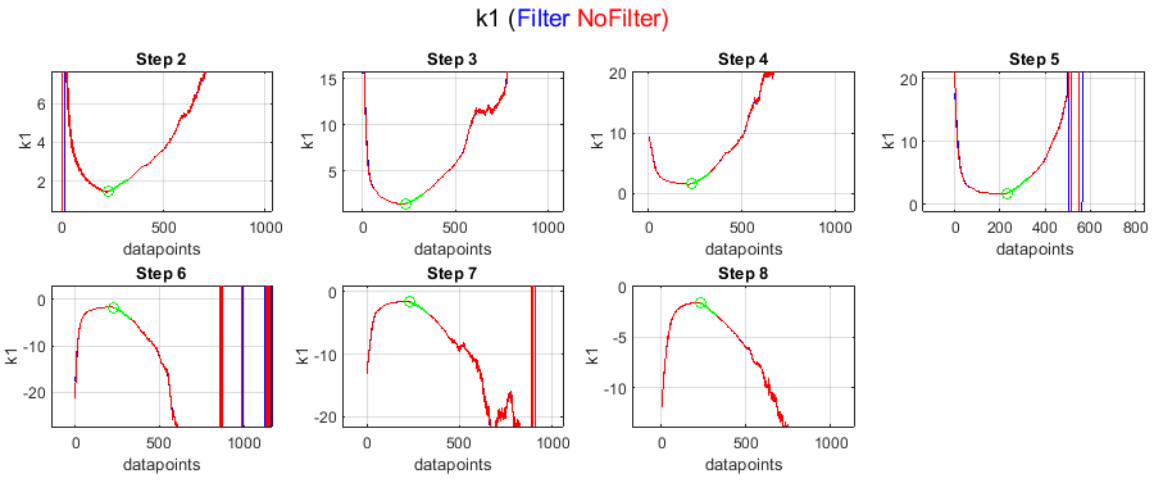


Figure 28. The quantity $k_1$, from Equation 9, plotted vs. time.

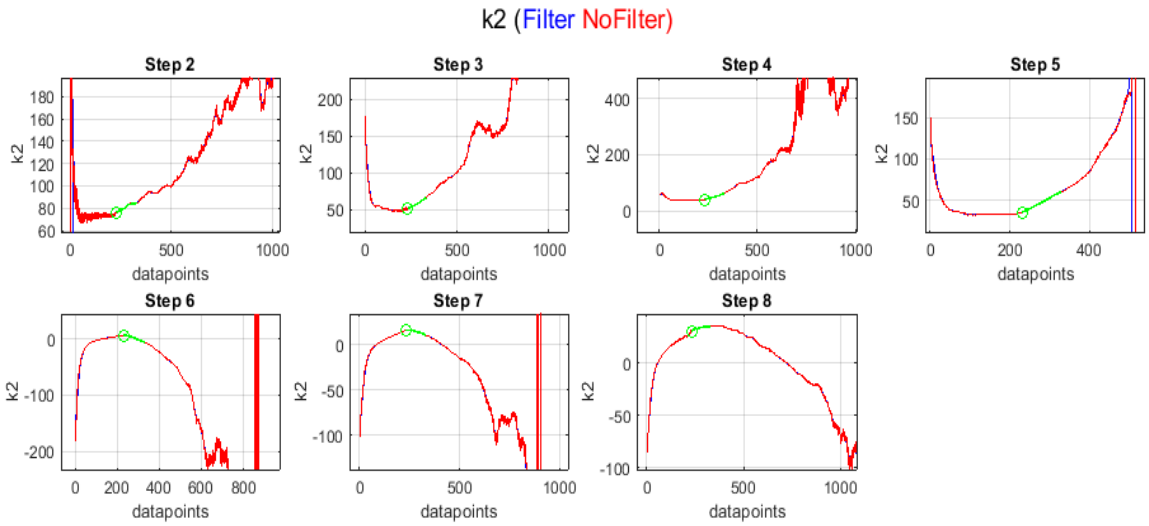


Figure 29. The quantity $k_2$, from Equation 9, plotted vs. time.

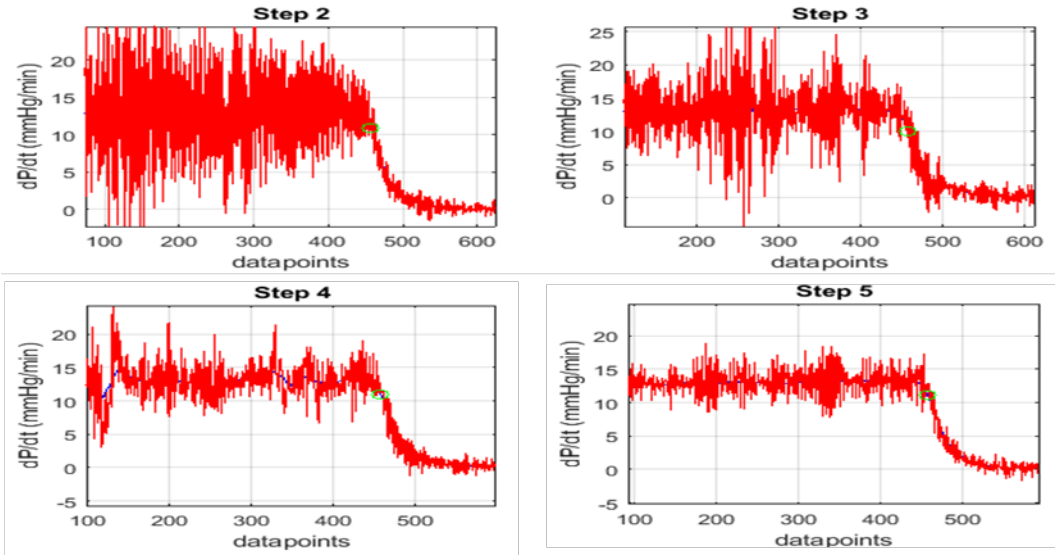


Figure 30. Temporal derivative of pressure vs. time from the system compliance experiment. Green circle shows the actuator stopping point.

### *A.4.2 Analysis using Equation 11*

In this section, the analysis described above is repeated for a perfusion of a control (wild-type) eye, with the difference that capillaries were removed from the iPerfusion system, resulting in a faster system time constant. The range of pressure steps was 4.5 – 15 mmHg, with 1.5 mmHg pressure steps (Table 4). Note that because of the faster response time in this system, a shorter time interval was considered for curve fitting. Specifically, the fitting interval was about 30 data points, which corresponds to 1.5 seconds of experimental data after the actuator stopped. Additionally, in this experiment, the needle resistance was more comparable to the flow sensor resistance and needed to be taken into account, as derived in Equation 11. The overall approach to the analysis is similar to the main text and is not repeated here. For comparison, we first analyze this dataset using Equation 9 and then using Equation 11.

Table 4. Applied pressure steps delivered to the eye described in Figure 31 to Figure 39.

| Step No. | Pressure (mmHg) |
|---|---|
| 1* | 4.5 to 6 |
| 2 | 6 to 7.5 |
| 3 | 7.5 to 9 |
| 4 | 9 to 10.5 |
| 5 | 10.5 to 12 |
| 6 | 12 to 13.5 |
| 7 | 13.5 to 15 |

* Step 1 is not considered for further analysis according to an established protocol (Sherwood et al., 2016).

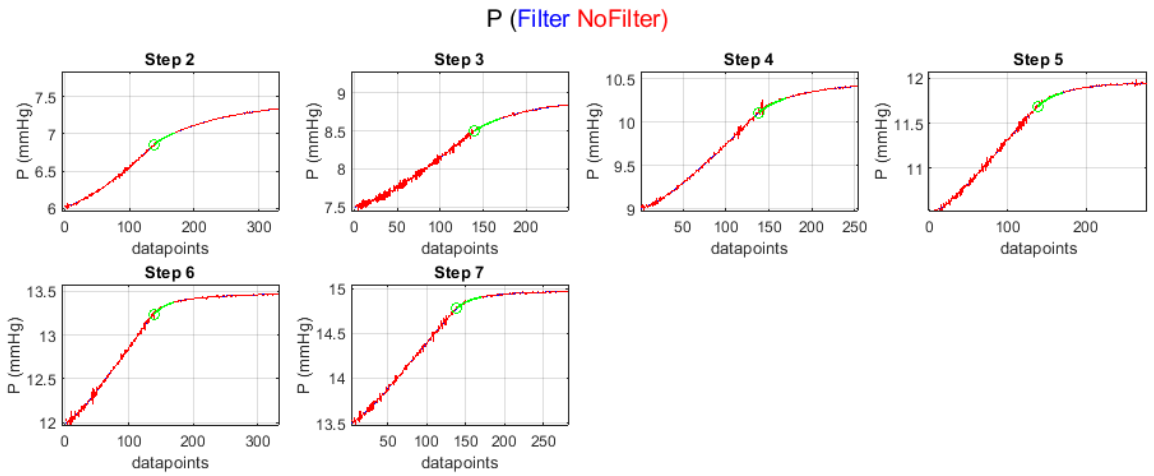


Figure 31. Pressure vs. time for each step. Green shows the interval picked for the analysis. Data points collected at 20 Hz.

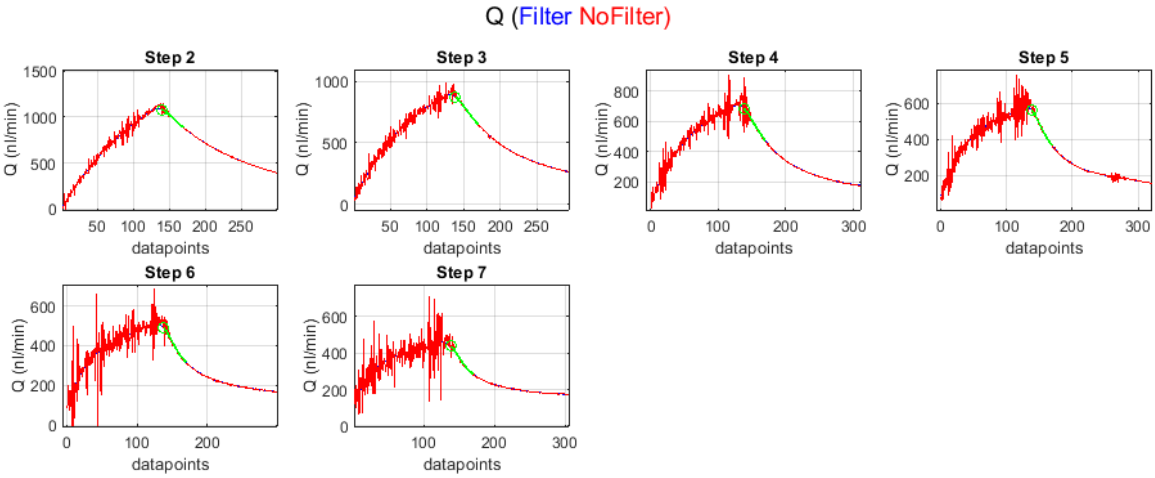


Figure 32. Flow rate vs. time corresponding to the pressure steps in Figure 31.

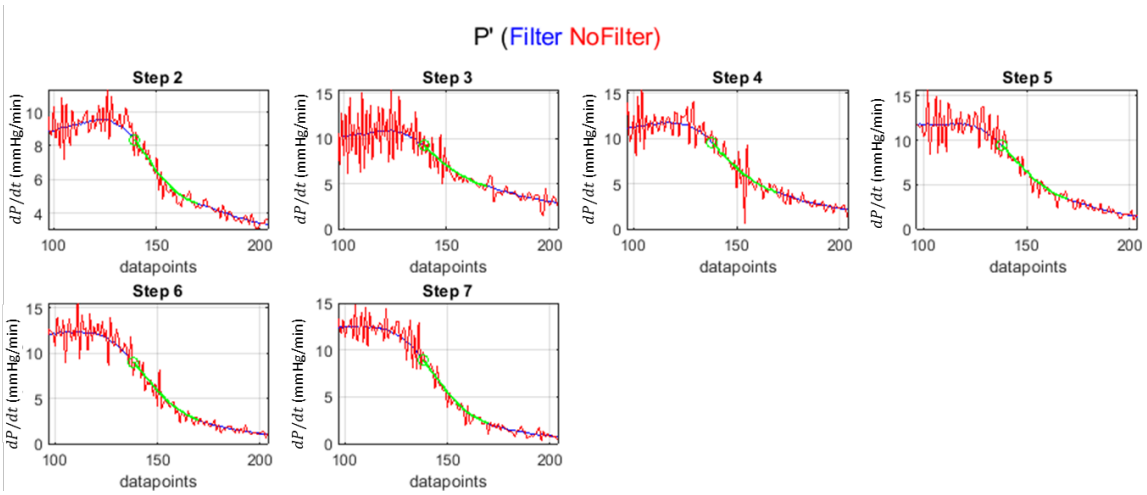


Figure 33. Time derivative of pressure vs. time corresponding to the steps in Figure 31.

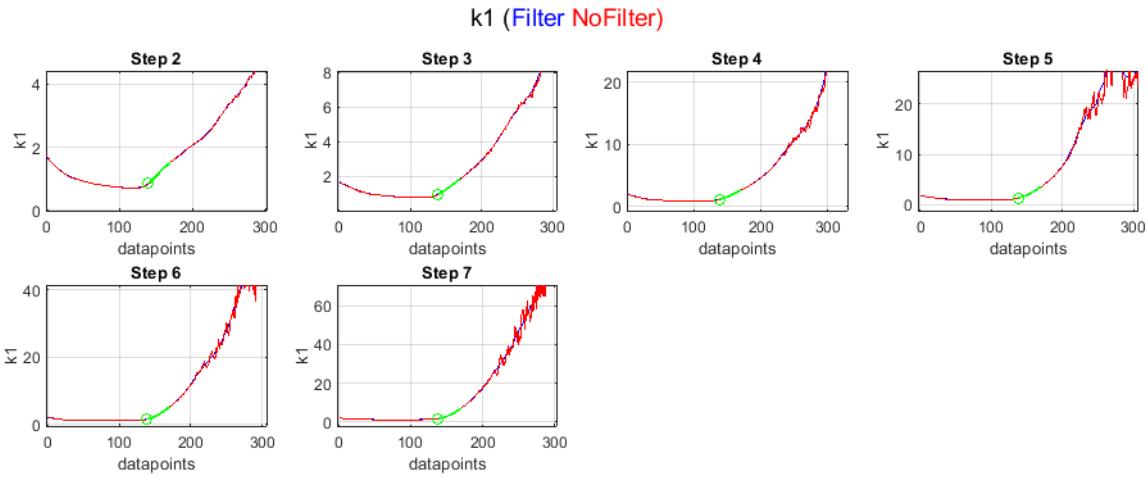


Figure 34. The quantity $k_1$, from Equation 9, vs. time.

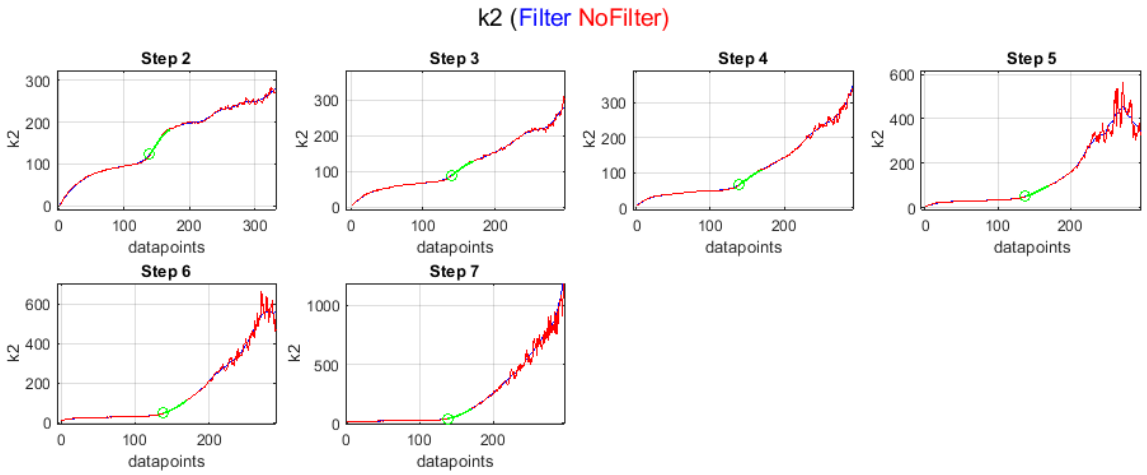


Figure 35. The quantity $k_2$, from Equation 9, vs. time.

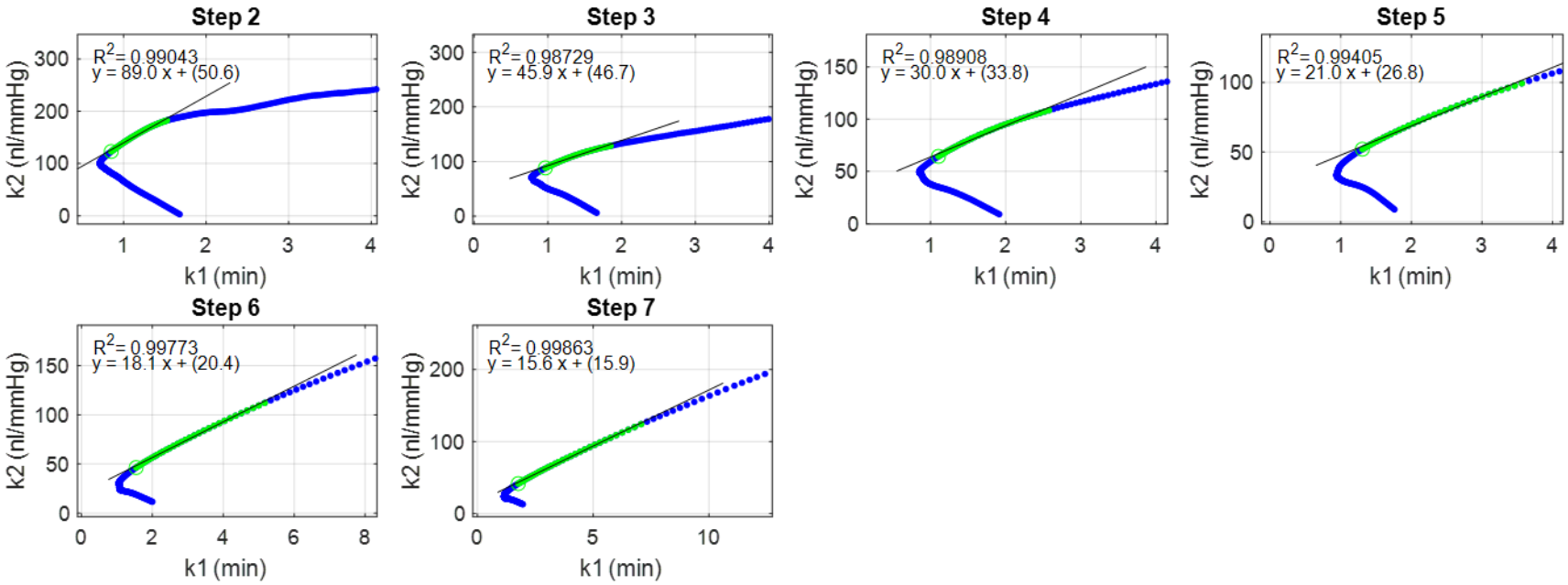
Step 2
R2= 0.99043
y = 89.0 x + (50.6)
k2 (nl/mmHg)
k1 (min)
Step 3
R2= 0.98729
y = 45.9 x + (46.7)
k2 (nl/mmHg)
k1 (min)
Step 4
R2= 0.98908
y = 30.0 x + (33.8)
k2 (nl/mmHg)
k1 (min)
Step 5
R2= 0.99405
y = 21.0 x + (26.8)
k2 (nl/mmHg)
k1 (min)
Step 6
R2= 0.99773
y = 18.1 x + (20.4)
k2 (nl/mmHg)
k1 (min)
Step 7
R2= 0.99863
y = 15.6 x + (15.9)
k2 (nl/mmHg)
k1 (min)

Figure 36. Plots of $k_2$ vs. $k_1$ for all the pressure steps. The slope of the regression line is the instantaneous outflow facility and the y-intercept is ocular compliance. Green shows the interval chosen for linear fitting.

In Figure 36, the instantaneous outflow facilities at initial steps are unexpectedly high and thus likely erroneous. Since the capillary upstream of flow sensor in the iPerfusion system was not in the circuit during this experiment, this error may be due to neglecting needle resistance. Thus, we decided to use Equation 11 to reanalyze the data, accounting for needle resistance. Before doing so, it was necessary to verify the assumptions mentioned in the Methods section under *Instantaneous linear fitting*, Figure 37 and Figure 38 show the validity of these assumptions.

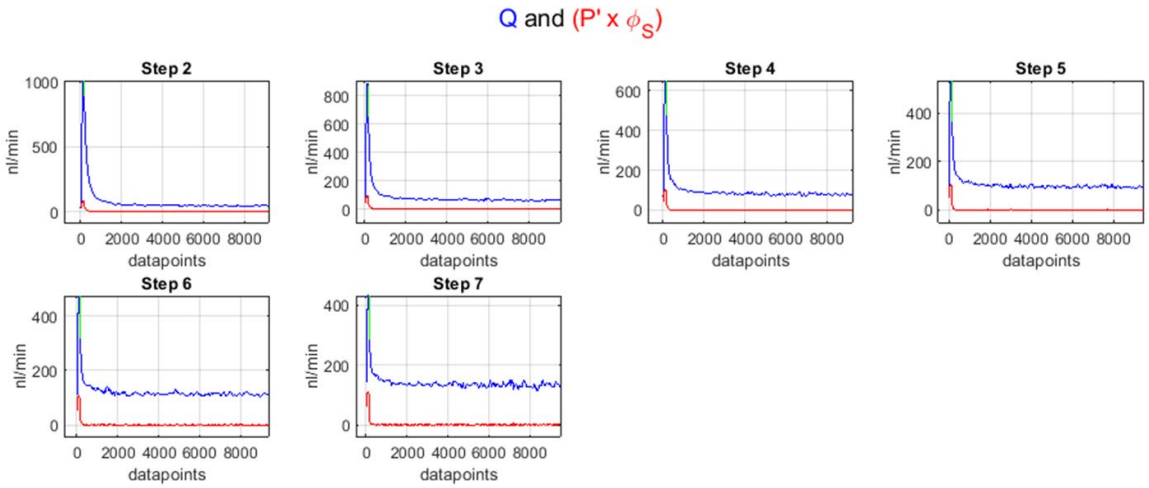


Figure 37. Plots of Q (blue) and $\frac{dP}{dt}$ $\phi_S$ (red) to confirm the negligibility of the latter quantity compared to the former. Note that the difference is greatest in the green region used in this analysis.

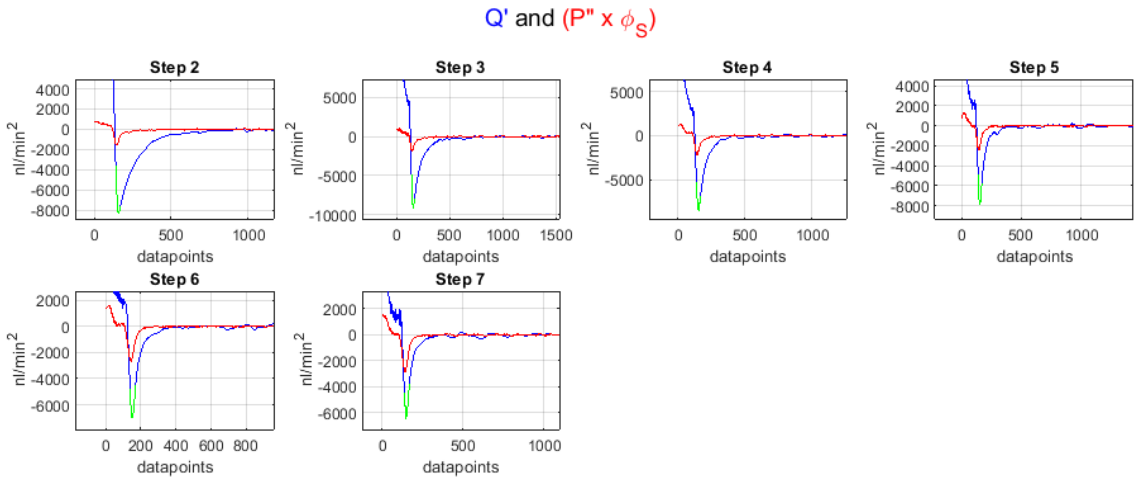


Figure 38. Plot of $\frac{dQ}{dt}$ and $\frac{d^2P}{dt^2}$ $\phi_S$ to confirm the negligibility of latter compared to the former. Interpretation is similar to Figure 37.

As confirmed by the above two figures, Equation 11 can be used to plot $k_{2N}$ vs. $k_{1N}$ (Figure 39). Values of instantaneous facility are lowered in this plot compared to Figure 36, but still appeared high.

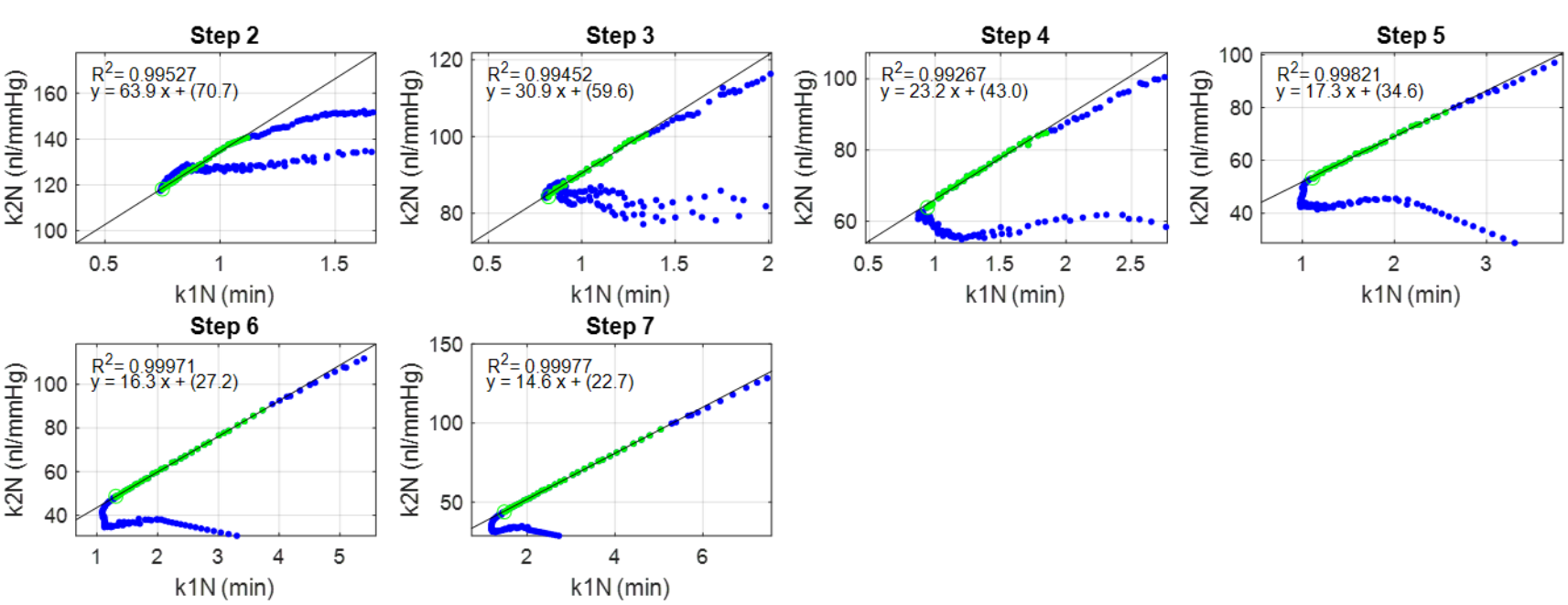
k2N vs k1N
Step 2
R2= 0.99527
y = 63.9 x + (70.7)
Step 3
R2= 0.99452
y = 30.9 x + (59.6)
Step 4
R2= 0.99267
y = 23.2 x + (43.0)
Step 5
R2= 0.99821
y = 17.3 x + (34.6)
Step 6
R2= 0.99971
y = 16.3 x + (27.2)
Step 7
R2= 0.99977
y = 14.6 x + (22.7)
k2N (nl/mmHg)
k1N (min)

Figure 39. Plot of $k_{2N}$ vs. $k_{1N}$ for each pressure step based on Equation 11. The slope of the regression line is the instantaneous outflow facility and the y-intercept is ocular compliance. Green shows the chosen interval for linear fitting.

# APPENDIX B. SUPPLEMENTARY INFORMATION FOR CHAPTER 4

## B.1 Purpose

In this appendix we calculate and compare the forces experienced by an individual SPION-labelled cell after injection into the anterior chamber. In addition to the buoyant, gravitational, and viscous forces in the no magnet method, the magnetic force exerted on the cell by the point magnet is also determined.

## B.2 Methods

To determine the magnetic force, 400 µl of the SPION solution (iron oxide concentration = 9 mg/ml, corresponding to 3.6 mg of iron oxide in 400 µl) was placed in a 0.6 ml microtube, which was then attached to a load cell (10 µN resolution, FSH03867, Futek, Irvine, CA) and the particles were collected at the bottom of the tube using a strong magnet. The bottom of this tube was then placed at precise distances from the tip of the point magnet using a high precision servo-controlled DC linear actuator (M-230.25, PI, Auburn, MA) incorporated in a micromechanical testing device. A tare force was read before placing the magnet in the vicinity of the SPION solution, and was subtracted from all readings to obtain the net magnetic force. The wall thickness of the microtube was 0.5 mm.

## B.3 Experimental Results

The magnetic force exerted by the point magnet on the SPIONs in the microtube decreased with distance from the magnet tip, as expected (Figure 40). In the point magnet delivery, the magnet tip is placed at the limbus and cells are released near the center of

the AC. Therefore, the smallest magnetic force experienced by injected cells occurs when the magnetic tip is separated from the cells by a distance equal to the radius of the mouse limbus, which we take as c. 1 mm. Using this distance to obtain an upper bound on the magnetic force, we read a force of 3.37 mN from Figure 40. The force on a single mesenchymal stem cell loaded with 25 μg/ml SPION (resulting in 35 pg intracellular iron oxide load (X. Li et al., 2019)) is then estimated as 33 pN, assuming the force experienced by a cell is scaled down from the measured 3.37 mN by the ratio of (iron oxide in the microtube)/(iron oxide in a cell). Table 5 includes the values of all the parameters used for the calculations throughout this chapter.

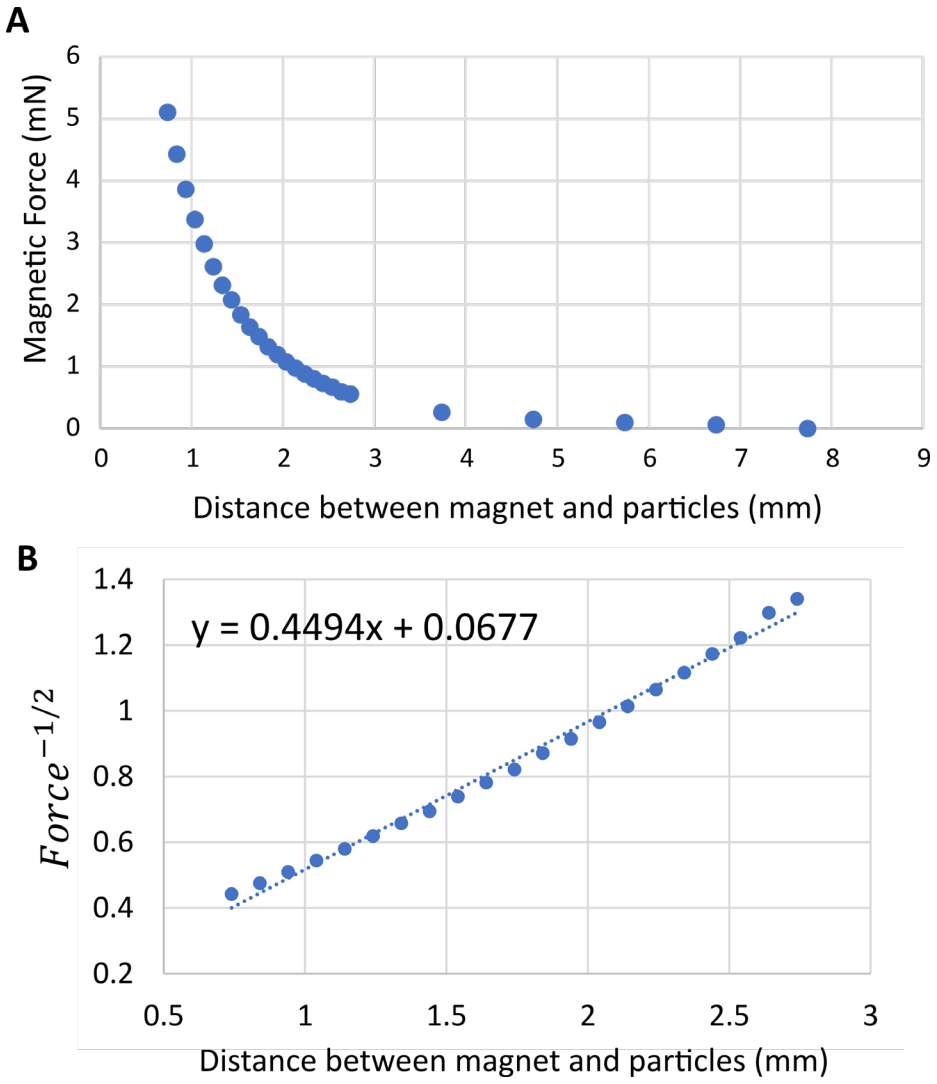


Figure 40. Measured magnetic force exerted by the point magnet on SPIONs in a microtube. A) Magnetic force as a function of distance between the particles and the magnet tip. B) Data in panel A linearized and fitted by linear regression ($R^2 = 0.99$). For two ideal magnetic dipoles, the force scales with the square of distance (Fernow, 2023). However, for more complicated geometries, such as the point magnet, deviation from this relationship is expected.

Table 5. Parameter values used for the calculations presented in this chapter.

| Parameter name | Value | Reference |
|---|---|---|
| Iron oxide per cell | $35 \times 10^{-12} g$ | (X. Li et al., 2019) |
| SPION stock solution density | $9\ mg/ml$ | Manufacturer |
| $2 \times r$ = Cell diameter | $15\ \mu m$ | (Drobek et al., 2023) |
| $\mu$ = AH viscosity at 37°C | $0.72\ cP$ | (Vass et al., 2004) |

| | | |
|---|---|---|
| Steady-state outflow rate | $50\ nl/min$ | Measured in perfusions |
| TM cross-sectional area | $0.0104\ cm^2$ | (Safa et al., 2023) |
| $\rho_{cell\ without\ SPIONs}$ = Cell density | $1.052\ g/cm^3$ | (Drobek et al., 2023) |
| $\rho_{AH}$=AH density | $1.007\ g/cm^3$ | (Vass et al., 2004) |
| $\rho_{SPION}$=SPION density | $5.24\ g/cm^3$ | Manufacturer |
| Mouse corneal (limbal) diameter | $2\ mm$ | (Wang et al., 2016) |

### B.4 Calculations

We now estimate other forces acting on cells by calculations.

*Viscous force due to AH flow:* Cells experience a force due to AH flow once they have been injected into the AC. In view of the low particle Reynolds number, this force can be calculated by Stokes' law:

$$F_v = 6\pi r\mu U \tag{12}$$

where $F_v$ is the viscous force, $r$ is particle (cell) radius, $\mu$ is AH dynamic viscosity, and $U$ is the relative velocity of the cell with respect to the AH. We obtain an upper bound for $F_v$ by considering the cell to be stationary and located in the anterior chamber at the location of maximal AH velocity, which is at the entrance of the TM where the flow-wise cross-sectional area is minimum. We compute this velocity as the ratio of steady-state flow rate measured in our perfusion experiments (50 nl/min) to the cross-sectional area of the TM (0.0104 $cm^2$). TM cross-sectional area is calculated using the dimensions found in the literature ($148\ \mu m$ anterior-posterior TM length and $2\ mm$ limbal diameter). The resulting velocity is $8 \times 10^{-5}\ cm/s$ and the viscous force experienced by a single cell is then estimated to be 0.0818 pN.

*Body forces:* The net body force is the sum of buoyant and gravitational force, which can be calculated as:

$$F_b = (\rho_{cell} - \rho_{AH}) g V_{cell} \tag{13}$$

where $\rho$ is density, $g$ is gravitational acceleration, and $V$ is volume. Here we neglect any viscous forces due to vertical flow of AH. Due to the uptake of SPIONs by the cell, its density changes, which can be estimated as:

$$\rho_{cell} = \frac{V_{uptaken\ SPIONs}}{V_{cell}} \rho_{SPION} + \frac{V_{Cell} - V_{uptaken\ SPIONs}}{V_{cell}} \rho_{cell\ without\ SPIONs} \tag{14}$$

Using this cell density ($\rho_{cell} = 1.068\ g/cm^3$), the net body force on a cell in AH is computed to be 1.06 pN.

### B.5 Conclusion

The force due to flowing AH experienced by a single MSC injected in the anterior chamber of a mouse eye is bounded above by our estimate of 0.0818 pN, which is ~400 times smaller than the smallest force applied by the point magnet (when the cell is at the center of the anterior chamber). This clearly indicates the benefit of using magnetic delivery using the point magnet compared to the no magnet approach, which relies on AH viscous forces, or compared to the ring magnet, which has zero horizonal component of magnetic force at the center of the eye. The force exerted by the point magnet is also 33 times larger than the net force due to gravity, allowing for efficient steering before injected cells sediment onto the lens and anterior iris.

# APPENDIX C. SUPPLEMENTARY INFORMATION FOR CHAPTER 5

## C.1 Supplementary figures

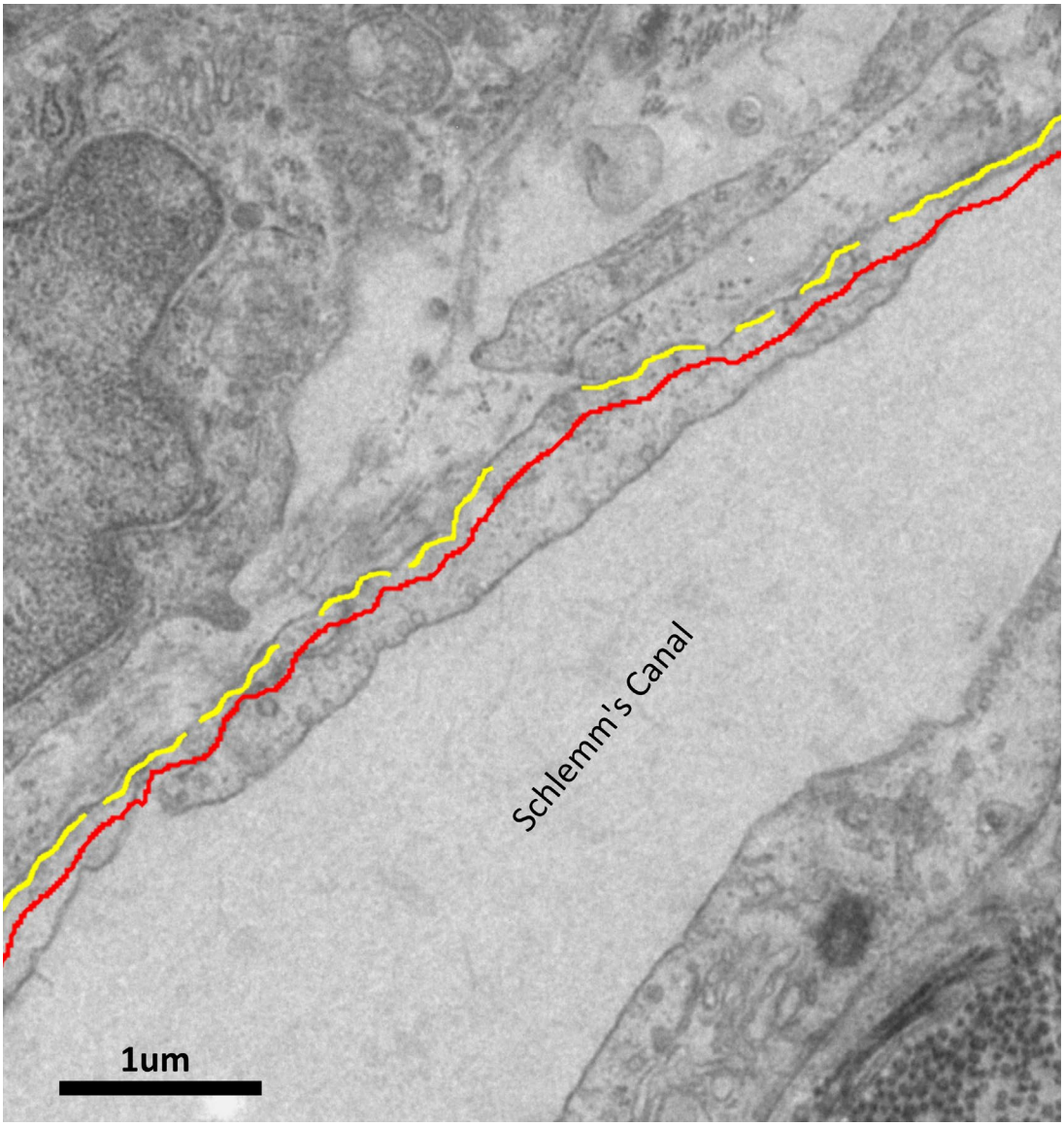


Figure 41. Quantification procedure for the amount of basement membrane materials adjacent to the inner wall of Schlemm's canal. The yellow line segments mark the basement membrane materials adjacent to the inner wall of Schlemm's canal. The summed length of yellow segments was then normalized by the overall length of the inner

wall (red) for quantifications. The red line is slightly shifted from the yellow segments for easier visualization.

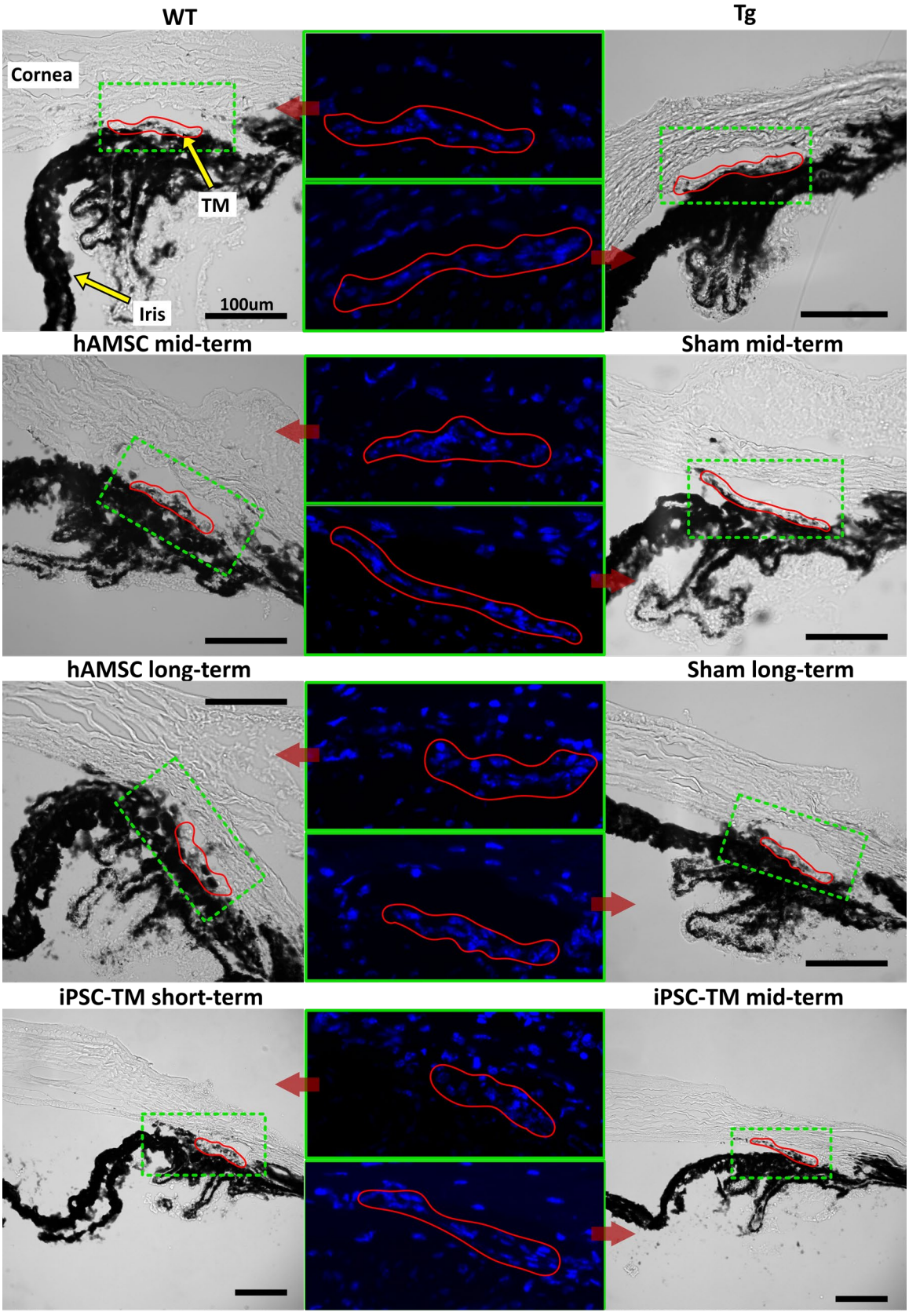
WT
Tg
Cornea
TM
Iris
100um
hAMSC mid-term
Sham mid-term
hAMSC long-term
Sham long-term
iPSC-TM short-term
iPSC-TM mid-term

Figure 42. Complementary micrographs to Figure 16 used for TM cellularity quantifications. Overview micrographs are shown in the left and right columns (see labels above images), with zoomed regions in the central column and indicated by the red arrows. Regions of interest (ROI), encompassing the parts of TM used for nuclei counting (demarcated in red) are outlined by green dashed boxes and the DAPI-stained nuclei (blue) are shown in a zoomed in fluorescent micrograph of the ROI (green solid box). In overview images in which the ROI is tilted, the corresponding fluorescent micrograph has been rotated counterclockwise so that it is horizontal so that the presentation is more compact.

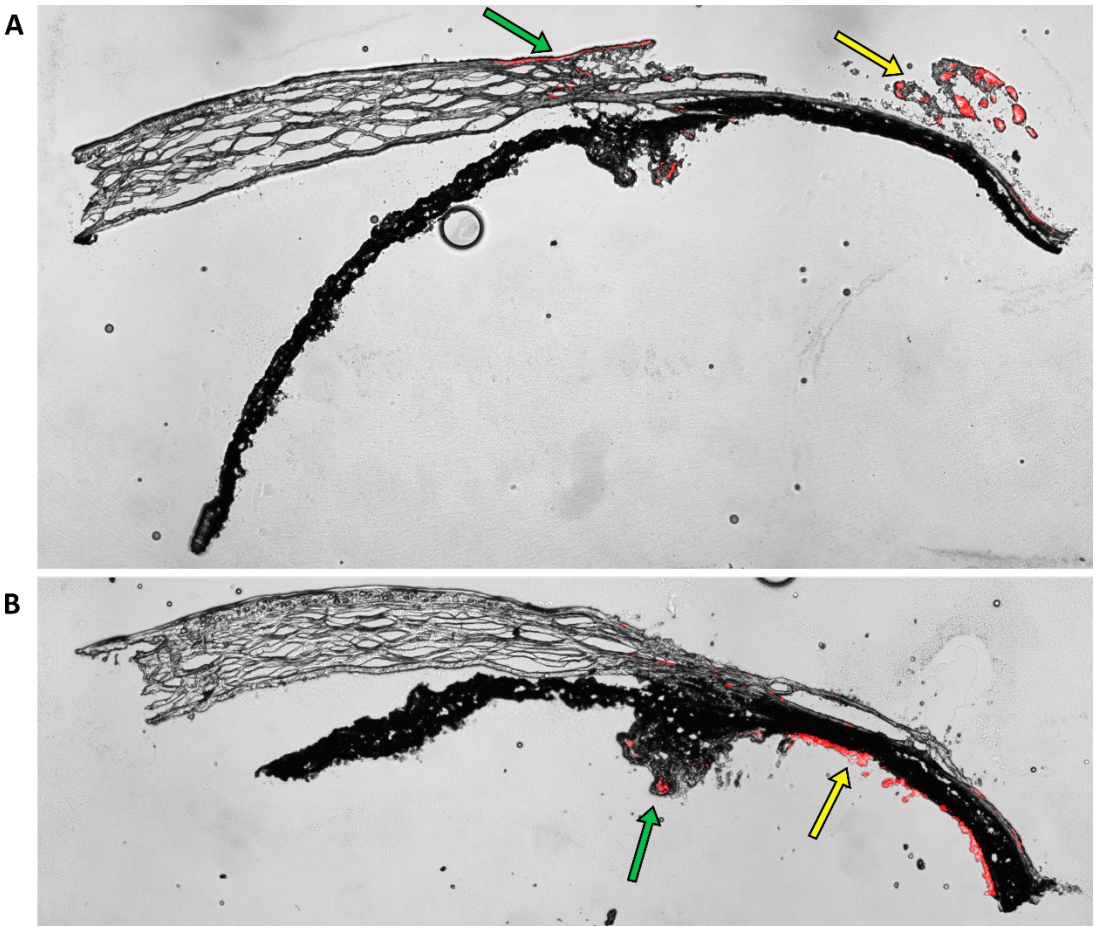


Figure 43. Autofluorescence from various ocular tissues at the same fluorescence settings as in Figure 18. The autofluorescence profile is contingent on the quality of dissection. In A, a signal is evident in insufficiently removed orbital tissue (yellow arrow) and at the limbus (green arrow). In B, autofluorescence is localized within the remaining retina (yellow arrow) and ciliary body (green arrow).

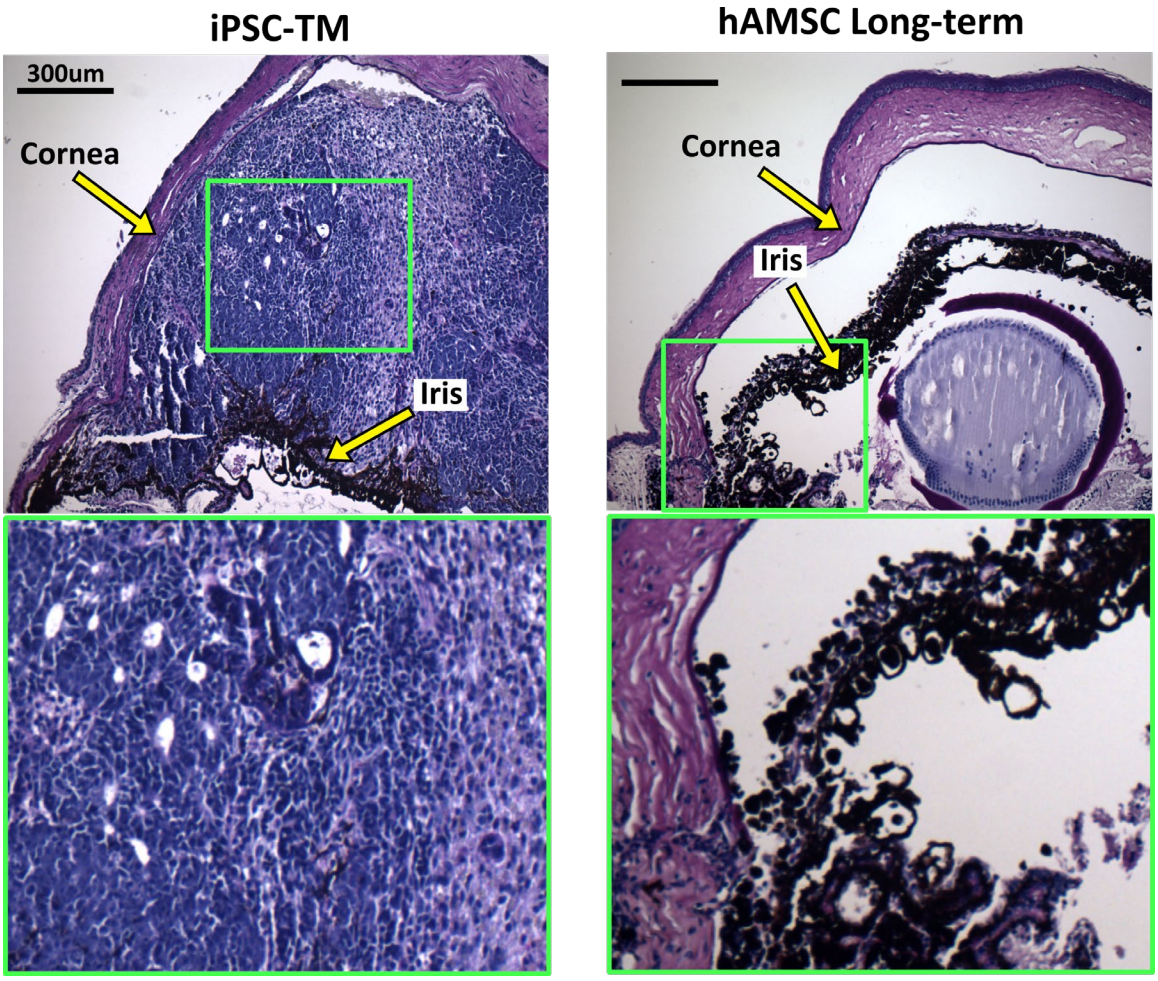


Figure 44. Histopathological assessment of tumorigenicity induced by transplanted cells, complementary to Figure 19. iPSC-TM- and hAMSC-transplanted eyes were stained with periodic acid–Schiff (PAS) stain. The degree of intracytoplasmic PAS stain in atypical cells is commonly used for identifiying tumor type and malignancy (Johnson and Wadehra, 2001). In this study, however, the PAS staining did not differentially add to the findings of H&E stain in Figure 19.

## C.2 SPION visualization post-transplantation

### *C.2.1 Prussian blue staining of SPIONs*

A Prussian blue solution was freshly prepared by mixing a 1:1 ratio of a 20% aqueous solution of hydrochloric acid and a 10% aqueous solution of potassium ferrocyanide (K4Fe(CN)6·3H2O, Sigma-Aldrich). Cryosections from the eyes which were sampled for cell retention studies were rehydrated for 30 minutes. Subsequently, the sections were

covered with the 10% potassium ferrocyanide solution for 5 minutes, followed by a 15-minute treatment with the Prussian blue solution. After treatment, the sections were rinsed three times in distilled water, dehydrated through increasing concentrations of ethanol, cleared in xylene, and then mounted for imaging.

### *C.2.2 SPIONs co-located with exogenous cells post-transplantation*

A major concern regarding the use of SPIONs for cell encapsulation is dose-dependent toxicity which could damage both the transplanted cells and native tissues (Sadeghiani et al., 2005; Stroh et al., 2004). We visualized the SPIONs in the sections used for cell retention visualization (same eyes as in Figure 18 but not necessarily the same sections) using Prussian blue staining (Figure 45). Unfortunately, this dark blue stain proved barely discernable from pigment. Detectible labeling could mostly be found at the same locations within the AC as in Figure 18 for the eye injected with hAMSC, where both the cells and SPIONs accumulated in the vicinity of TM, and for the eye injected with iPSC-TM, with the cells and SPIONs found within the TM. Prussian blue did not stain materials in the saline-injected control eyes.

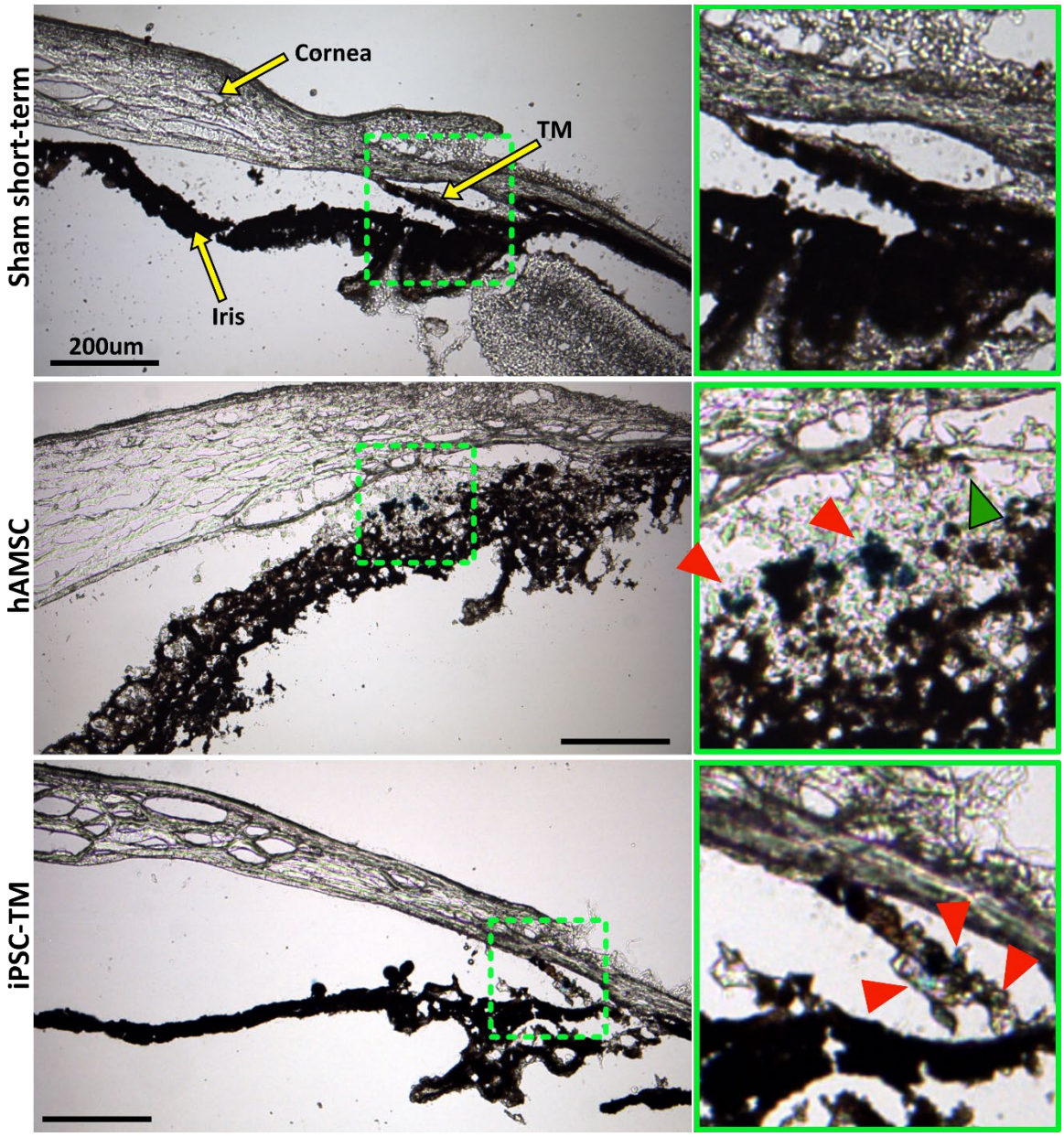


Figure 45. Prussian blue staining to locate SPIONs within the anterior segment after cell transplantation, taken from the same eyes as in Figure 18 (although not necessarily the same sections). The left column shows overview images of the anterior segment, while green boxes in the right column show a zoomed view of the region with strongest Prussian blue staining. Top row: No Prussian blue staining could be found in the saline injection control. Middle row: Prussian blue stain is challenging to distinguish from melanin, but accumulation of blue label (red arrowheads) can be seen to coincide with the locations of exogenous cells visualized in Figure 18. In particular, injected hAMSCs primarily accumulated close to the TM, corresponding to the location of Prussian blue stain. A small region of Prussian blue staining can be observed in the TM (green arrowhead). Bottom row: Similarly, in eyes receiving iPSC-TMs, most of the Prussian blue staining was found within the TM, corresponding to the location of injected cells (Figure 18). Unfortunately,

the fluorescent signal in Figure 18 was significantly attenuated after Prussian blue staining and could not be overlaid on these images to assist with interpretation.

### *C.2.3 SPIONs did not accumulate within the native tissues of the AC*

Iron oxide-induced toxicity, both as cytotoxicity and genotoxicity, is a major concern when using SPIONs in cell encapsulation and transplantation. *In vitro* studies have reported that SPION labeling is generally safe at concentrations below 100 µg/ml (Singh et al., 2010). Since we used a four-fold lower concentration for cell labeling in this study, the encapsulated cells were likely unaffected.

Once inside the AC, the SPIONs may be released from the injected cells. The TM, as the phagocytic and filtering component of the main AH outflow pathway, is a likely destination. Our Prussian blue staining to visualize SPIONs in the AC after delivery was masked by pigmentation and was hard to visualize (Figure 45). The SPIONs that we could detect were mostly co-located with the transplanted cells and were likely not released at a significant rate within the AC. In the case of iPSC-TM cells, which showed good integration with the TM, detectable SPIONs were also primarily found within the TM. Whether these SPIONs had been released from the injected cells or were still encapsulated remains unknown. Nevertheless, the significant increase in TM cellularity discussed above indicates that accumulation of SPIONs within the TM is unlikely to have any toxic effect on native tissues.

# REFERENCES


Abu-Hassan, D., Acott, T., Kelley, M., 2014. The Trabecular Meshwork: A Basic Review of Form and Function. J. Ocul. Biol. 2. https://doi.org/10.13188/2334-2838.1000017

Abu-Hassan, D.W., Li, X., Ryan, E.I., Acott, T.S., Kelley, M.J., 2015. Induced Pluripotent Stem Cells Restore Function in a Human Cell Loss Model of Open-Angle Glaucoma. Stem Cells 33, 751–761. https://doi.org/10.1002/stem.1885

Acott, T., Samples, J.R., Bradley, J.M., Bacon, D.R., Bylsma, S.S., Van Buskirk, E.M., 1989. Trabecular Repopulation by Anterior Trabecular Meshwork Cells After Laser Trabeculoplasty: Reply. Am. J. Ophthalmol. 108, 210.

Acott, T.S., Kelley, M.J., Keller, K.E., Vranka, J.A., Abu-Hassan, D.W., Li, X., Aga, M., Bradley, J.M., 2014. Intraocular pressure homeostasis: maintaining balance in a high-pressure environment. J. Ocul. Pharmacol. Ther. Off. J. Assoc. Ocul. Pharmacol. Ther. 30, 94–101. https://doi.org/10.1089/jop.2013.0185

Aihara, M., Lindsey, J.D., Weinreb, R.N., 2003. Twenty-four-hour pattern of mouse intraocular pressure. Exp. Eye Res. 77, 681–686. https://doi.org/10.1016/j.exer.2003.08.011

Alm, A., Nilsson, S.F., 2009. Uveoscleral outflow–a review. Exp. Eye Res. 88, 760–768.

Alvarado, J., Murphy, C., Juster, R., 1984. Trabecular Meshwork Cellularity in Primary Open-angle Glaucoma and Nonglaucomatous Normals. Ophthalmology 91, 564–579. https://doi.org/10.1016/S0161-6420(84)34248-8

Anselmo, A.C., Mitragotri, S., 2015. A Review of Clinical Translation of Inorganic Nanoparticles. AAPS J. 17, 1041. https://doi.org/10.1208/s12248-015-9780-2

Bahrani Fard, M.R., Chan, J., Sanchez Rodriguez, G., Yonk, M., Kuturu, S.R., Read, A.T., Emelianov, S.Y., Kuehn, M.H., Ethier, C.R., 2023. Improved magnetic delivery of cells to the trabecular meshwork in mice. Exp. Eye Res. 234, 109602. https://doi.org/10.1016/j.exer.2023.109602

Barnebey, H.S., Robin, A.L., 2017. Adherence to fixed-combination versus unfixed travoprost 0.004%/timolol 0.5% for glaucoma or ocular hypertension: a randomized trial. Am. J. Ophthalmol. 176, 61–69.

Bekerman, I., Gottlieb, P., Vaiman, M., 2014. Variations in eyeball diameters of the healthy adults. J. Ophthalmol. 2014.

Bianco, P., Robey, P.G., 2001. Stem cells in tissue engineering. Nature 414, 118–121.

Boone, C.W., DuPree, L.T., 1968. Quantitative tumorigenicity assays using the anterior chamber of the mouse eye. Cancer Res. 28, 1734–1737.

Braunger, B.M., Ademoglu, B., Koschade, S.E., Fuchshofer, R., B'Ann, T.G., Kiland, J.A., Hennes-Beann, E.A., Brunner, K.G., Kaufman, P.L., Tamm, E.R., 2014. Identification of adult stem cells in Schwalbe's line region of the primate eye. Invest. Ophthalmol. Vis. Sci. 55, 7499–7507.

Brubaker, R.F., 2004. Goldmann's equation and clinical measures of aqueous dynamics. Exp. Eye Res. 78, 633–637.

Brubaker, R.F., 2003. Targeting outflow facility in glaucoma management. Surv. Ophthalmol. 48 Suppl 1, S17-20. https://doi.org/10.1016/s0039-6257(03)00003-1

Burand Jr, A.J., Di, L., Boland, L.K., Boyt, D.T., Schrodt, M.V., Santillan, D.A., Ankrum, J.A., 2020. Aggregation of human mesenchymal stromal cells eliminates their ability to suppress human T cells. Front. Immunol. 11, 143.

Calkins, D.J., Lambert, W.S., Formichella, C.R., McLaughlin, W.M., Sappington, R.M., 2018. The Microbead Occlusion Model of Ocular Hypertension in Mice, in: Jakobs, T.C. (Ed.), Glaucoma: Methods and Protocols. Springer New York, New York, NY, pp. 23–39. https://doi.org/10.1007/978-1-4939-7407-8_3

Candia, O.A., Gerometta, R., Millar, J.C., Podos, S.M., 2010. Suppression of corticosteroid-induced ocular hypertension in sheep by anecortave. Arch. Ophthalmol. 128, 338–343.

Castro, A., Du, Y., 2019. Trabecular Meshwork Regeneration—a Potential Treatment for Glaucoma. Curr. Ophthalmol. Rep. 7, 80–88. https://doi.org/10.1007/s40135-019-00203-2

Chang, J.Y., Folz, S.J., Laryea, S.N., Overby, D.R., 2014a. Multi-scale analysis of segmental outflow patterns in human trabecular meshwork with changing intraocular pressure. J. Ocul. Pharmacol. Ther. 30, 213–223.

Chang, J.Y., Folz, S.J., Laryea, S.N., Overby, D.R., 2014b. Multi-scale analysis of segmental outflow patterns in human trabecular meshwork with changing intraocular pressure. J. Ocul. Pharmacol. Ther. 30, 213–223.

Chen, H., Wei, X., Cho, K.-S., Chen, G., Sappington, R., Calkins, D.J., Chen, D.F., 2011. Optic Neuropathy Due to Microbead-Induced Elevated Intraocular Pressure in the Mouse. Invest. Ophthalmol. Vis. Sci. 52, 36–44. https://doi.org/10.1167/iovs.09-5115

Coleman, A.L., Miglior, S., 2008. Risk factors for glaucoma onset and progression. Surv. Ophthalmol. 53, S3–S10.

Collaborative Normal-Tension Glaucoma Study Group, 1998. Comparison of glaucomatous progression between untreated patients with normal-tension glaucoma and patients with therapeutically reduced intraocular pressures. Am. J. Ophthalmol. 126, 487–497. https://doi.org/10.1016/S0002-9394(98)00223-2

Cone, F.E., Gelman, S.E., Son, J.L., Pease, M.E., Quigley, H.A., 2010. Differential susceptibility to experimental glaucoma among 3 mouse strains using bead and

viscoelastic injection. Exp. Eye Res. 91, 415–424. https://doi.org/10.1016/j.exer.2010.06.018

Coulon, S.J., Schuman, J.S., Du, Y., Fard, M.R.B., Ethier, C.R., Stamer, W.D., 2022. A novel glaucoma approach: Stem cell regeneration of the trabecular meshwork. Prog. Retin. Eye Res. 90, 101063.

Cyranoski, D., 2019. 'Reprogrammed' stem cells to treat spinal-cord injuries for the first time [WWW Document]. URL doi.org/10.1038/d41586-019-00656-2 (accessed 10.7.23).

Dammak, A., Pastrana, C., Martin-Gil, A., Carpena-Torres, C., Peral Cerda, A., Simovart, M., Alarma, P., Huete-Toral, F., Carracedo, G., 2023. Oxidative Stress in the Anterior Ocular Diseases: Diagnostic and Treatment. Biomedicines 11, 292. https://doi.org/10.3390/biomedicines11020292

Davis, G., 2016. The Evolution of Cataract Surgery. Mo. Med. 113, 58–62.

de Kater, A.W., Melamed, S., Epstein, D.L., 1989. Patterns of aqueous humor outflow in glaucomatous and nonglaucomatous human eyes: a tracer study using cationized ferritin. Arch. Ophthalmol. 107, 572–576.

Deinsberger, J., Reisinger, D., Weber, B., 2020. Global trends in clinical trials involving pluripotent stem cells: a systematic multi-database analysis. Npj Regen. Med. 5, 1–13. https://doi.org/10.1038/s41536-020-00100-4

Ding, Q.J., Zhu, W., Cook, A.C., Anfinson, K.R., Tucker, B.A., Kuehn, M.H., 2014. Induction of trabecular meshwork cells from induced pluripotent stem cells. Invest. Ophthalmol. Vis. Sci. 55, 7065–7072.

Du, Y., Roh, D.S., Mann, M.M., Funderburgh, M.L., Funderburgh, J.L., Schuman, J.S., 2012. Multipotent stem cells from trabecular meshwork become phagocytic TM cells. Invest. Ophthalmol. Vis. Sci. 53, 1566–1575.

Dunning, M.D., Kettunen, M.I., Ffrench Constant, C., Franklin, R.J.M., Brindle, K.M., 2006. Magnetic resonance imaging of functional Schwann cell transplants labelled with magnetic microspheres. NeuroImage 31, 172–180. https://doi.org/10.1016/j.neuroimage.2005.11.050

Ethier, C.R., Kamm, R.D., Palaszewski, B.A., Johnson, M.C., Richardson, T.M., 1986. Calculations of flow resistance in the juxtacanalicular meshwork. Invest. Ophthalmol. Vis. Sci. 27, 1741–1750.

Filippopoulos, T., Matsubara, A., Danias, J., Huang, W., Dobberfuhl, A., Ren, L., Mittag, T., Miller, J.W., Grosskreutz, C.L., 2006. Predictability and limitations of non-invasive murine tonometry: comparison of two devices. Exp. Eye Res. 83, 194–201. https://doi.org/10.1016/j.exer.2005.12.005

Finn, J.P., Nguyen, K.-L., Han, F., Zhou, Z., Salusky, I., Ayad, I., Hu, P., 2016. Cardiovascular MR Imaging with Ferumoxytol. Clin. Radiol. 71, 796–806. https://doi.org/10.1016/j.crad.2016.03.020

Frankfort, B.J., Khan, A.K., Tse, D.Y., Chung, I., Pang, J.-J., Yang, Z., Gross, R.L., Wu, S.M., 2013. Elevated Intraocular Pressure Causes Inner Retinal Dysfunction Before Cell Loss in a Mouse Model of Experimental Glaucoma. Invest. Ophthalmol. Vis. Sci. 54, 762–770. https://doi.org/10.1167/iovs.12-10581

Friedman, H., Ator, N., Haigwood, N., Newsome, W., Allan, J.S., Golos, T.G., Kordower, J.H., Shade, R.E., Goldberg, M.E., Bailey, M.R., Bianchi, P., 2017. The Critical Role of Nonhuman Primates in Medical Research. Pathog. Immun. 2, 352–365. https://doi.org/10.20411/pai.v2i3.186

Fuchshofer, R., Welge-Lussen, U., Lütjen-Drecoll, E., 2003. The effect of TGF-β2 on human trabecular meshwork extracellular proteolytic system. Exp. Eye Res. 77, 757–765. https://doi.org/10.1016/S0014-4835(03)00220-3

Gelatt, K.N., Mackay, E.O., 1998. The ocular hypertensive effects of topical 0.1% dexamethasone in beagles with inherited glaucoma. J. Ocul. Pharmacol. Ther. 14, 57–66.

Gerberich, B.G., Hannon, B.G., Brown, D.M., Read, A.T., Ritch, M.D., Schrader Echeverri, E., Nichols, L., Potnis, C., Sridhar, S., Toothman, M.G., Schwaner, S.A., Winger, E.J., Huang, H., Gershon, G.S., Feola, A.J., Pardue, M.T., Prausnitz, M.R., Ethier, C.R., 2022. Evaluation of Spatially Targeted Scleral Stiffening on Neuroprotection in a Rat Model of Glaucoma. Transl. Vis. Sci. Technol. 11, 7. https://doi.org/10.1167/tvst.11.5.7

Gerometta, R., Podos, S.M., Candia, O.A., Wu, B., Malgor, L.A., Mittag, T., Danias, J., 2004. Steroid-induced ocular hypertension in normal cattle. Arch. Ophthalmol. 122, 1492–1497.

Goel, M., Picciani, R.G., Lee, R.K., Bhattacharya, S.K., 2010. Aqueous humor dynamics: a review. Open Ophthalmol. J. 4, 52.

Gong, H., Swain, D.L., 2016a. SD The histopathological changes in the trabecular outflow pathway and their possible effects on aqueous outflow in eyes with primary open-angle glaucoma. Glaucoma Res. Clin. Adv. 2018, 17–40.

Gong, H., Swain, D.L., 2016b. The histopathological changes in the trabecular outflow pathway and their possible effects on aqueous outflow in eyes with primary open-angle glaucoma, in: Samples, J.R., Knepper, P.A. (Eds.), Glaucoma Research and Clinical Advances. Kugler Amsterdam, pp. 17–40.

Graber, T.G., Ferguson-Stegall, L., Kim, J.-H., Thompson, L.V., 2013. C57BL/6 Neuromuscular Healthspan Scoring System. J. Gerontol. A. Biol. Sci. Med. Sci. 68, 1326–1336. https://doi.org/10.1093/gerona/glt032

Gutova, M., Frank, J.A., D'Apuzzo, M., Khankaldyyan, V., Gilchrist, M.M., Annala, A.J., Metz, M.Z., Abramyants, Y., Herrmann, K.A., Ghoda, L.Y., Najbauer, J., Brown, C.E., Blanchard, M.S., Lesniak, M.S., Kim, S.U., Barish, M.E., Aboody, K.S., Moats, R.A., 2013. Magnetic Resonance Imaging Tracking of Ferumoxytol-Labeled Human Neural Stem Cells: Studies Leading to Clinical Use. Stem Cells Transl. Med. 2, 766–775. https://doi.org/10.5966/sctm.2013-0049

Ha, J., J, S., 2006. Toxicity of metal oxide nanoparticles in mammalian cells. J. Environ. Sci. Health Part A Tox. Hazard. Subst. Environ. Eng. 41. https://doi.org/10.1080/10934520600966177

Häfeli, U.O., Riffle, J.S., Harris-Shekhawat, L., Carmichael-Baranauskas, A., Mark, F., Dailey, J.P., Bardenstein, D., 2009. Cell Uptake and in Vitro Toxicity of Magnetic Nanoparticles Suitable for Drug Delivery. Mol. Pharm. 6, 1417–1428. https://doi.org/10.1021/mp900083m

Heijl, A., Leske, M.C., Bengtsson, Bo, Hyman, L., Bengtsson, Boel, Hussein, M., Group, E.M.G.T., 2002. Reduction of intraocular pressure and glaucoma progression: results from the Early Manifest Glaucoma Trial. Arch. Ophthalmol. 120, 1268–1279.

Hirano, K., Kobayashi, M., Kobayashi, K., Hoshino, T., Awaya, S., 1989. Experimental formation of 100 nm periodic fibrils in the mouse corneal stroma and trabecular meshwork. Invest. Ophthalmol. Vis. Sci. 30, 869–874.

Hogan, M., Alvarado, JA,, Weddell, JE, 1971. Histology of the Human Eye: An Atlas and Textbook. Atlas Textb.

Hu, Y., Danias, J., 2018. Noninvasive intraocular pressure measurement in animals models of glaucoma. Glaucoma Methods Protoc. 49–61.

Huang, Y., Hsu, J.C., Koo, H., Cormode, D.P., 2022. Repurposing ferumoxytol: Diagnostic and therapeutic applications of an FDA-approved nanoparticle. Theranostics 12, 796–816. https://doi.org/10.7150/thno.67375

Inagaki, E., Arai, E., Hatou, S., Sayano, T., Taniguchi, H., Negishi, K., Kanai, Y., Sato, Y., Okano, H., Tsubota, K., Shimmura, S., 2022. The Anterior Eye Chamber as a Visible Medium for In Vivo Tumorigenicity Tests. Stem Cells Transl. Med. 11, 841–849. https://doi.org/10.1093/stcltm/szac036

Ito, Y.A., Belforte, N., Cueva Vargas, J.L., Di Polo, A., 2016. A Magnetic Microbead Occlusion Model to Induce Ocular Hypertension-Dependent Glaucoma in Mice. J. Vis. Exp. JoVE e53731. https://doi.org/10.3791/53731

Jia, L., Cepurna, W.O., Johnson, E.C., Morrison, J.C., 2000. Patterns of intraocular pressure elevation after aqueous humor outflow obstruction in rats. Invest. Ophthalmol. Vis. Sci. 41, 1380–1385.

Johnson, M., McLaren, J.W., Overby, D.R., 2017. Unconventional aqueous humor outflow: a review. Exp. Eye Res. 158, 94–111.

Johnson, S.J., Wadehra, V., 2001. The importance of intracytoplasmic DPAS positivity in fine needle aspirates of breast lesions. J. Clin. Pathol. 54, 146–151. https://doi.org/10.1136/jcp.54.2.146

Johnston, M.C., Noden, D.M., Hazelton, R.D., Coulombre, J.L., Coulombre, A.J., 1979. Origins of avian ocular and periocular tissues. Exp. Eye Res. 29, 27–43.

Kass, M.A., Heuer, D.K., Higginbotham, E.J., Johnson, C.A., Keltner, J.L., Miller, J.P., Parrish, R.K., Wilson, M.R., Gordon, M.O., 2002. The Ocular Hypertension Treatment Study: a randomized trial determines that topical ocular hypotensive medication delays or prevents the onset of primary open-angle glaucoma. Arch. Ophthalmol. Chic. Ill 1960 120, 701–713; discussion 829-830. https://doi.org/10.1001/archopht.120.6.701

Kelley, M.J., Rose, A.Y., Keller, K.E., Hessle, H., Samples, J.R., Acott, T.S., 2009. Stem cells in the trabecular meshwork: present and future promises. Exp. Eye Res. 88, 747–751.

Kim, J.S., Yoon, T.-J., Yu, K.N., Kim, B.G., Park, S.J., Kim, H.W., Lee, K.H., Park, S.B., Lee, J.-K., Cho, M.H., 2006. Toxicity and Tissue Distribution of Magnetic Nanoparticles in Mice. Toxicol. Sci. 89, 338–347. https://doi.org/10.1093/toxsci/kfj027

Kim, S.J., Lewis, B., Steiner, M.-S., Bissa, U.V., Dose, C., Frank, J.A., 2016. Superparamagnetic iron oxide nanoparticles for direct labeling of stem cells and in vivo MRI tracking. Contrast Media Mol. Imaging 11, 55–64. https://doi.org/10.1002/cmmi.1658

Klein, B.E.K., Klein, R., Knudtson, M.D., 2005. Intraocular pressure and systemic blood pressure: longitudinal perspective: the Beaver Dam Eye Study. Br. J. Ophthalmol. 89, 284–287.

Koskela, T.K., Reiss, G.R., Brubaker, R.F., Ellefson, R.D., 1989. Is the high concentration of ascorbic acid in the eye an adaptation to intense solar irradiation? Invest. Ophthalmol. Vis. Sci. 30, 2265–2267.

Kovacević, N., Henderson, J.T., Chan, E., Lifshitz, N., Bishop, J., Evans, A.C., Henkelman, R.M., Chen, X.J., 2005. A three-dimensional MRI atlas of the mouse brain with estimates of the average and variability. Cereb. Cortex N. Y. N 1991 15, 639–645. https://doi.org/10.1093/cercor/bhh165

Lalu, M.M., McIntyre, L., Pugliese, C., Fergusson, D., Winston, B.W., Marshall, J.C., Granton, J., Stewart, D.J., 2012. Safety of Cell Therapy with Mesenchymal Stromal Cells (SafeCell): A Systematic Review and Meta-Analysis of Clinical Trials. PLOS ONE 7, e47559. https://doi.org/10.1371/journal.pone.0047559

Lamm, N., Ben-David, U., Golan-Lev, T., Storchová, Z., Benvenisty, N., Kerem, B., 2016. Genomic Instability in Human Pluripotent Stem Cells Arises from Replicative Stress and Chromosome Condensation Defects. Cell Stem Cell 18, 253–261. https://doi.org/10.1016/j.stem.2015.11.003

Li, G., Lee, C., Agrahari, V., Wang, K., Navarro, I., Sherwood, J.M., Crews, K., Farsiu, S., Gonzalez, P., Lin, C.-W., Mitra, A.K., Ethier, C.R., Stamer, W.D., 2019. In vivo measurement of trabecular meshwork stiffness in a corticosteroid-induced ocular hypertensive mouse model. Proc. Natl. Acad. Sci. U. S. A. 116, 1714–1722. https://doi.org/10.1073/pnas.1814889116

Li, G., Lee, C., Read, A.T., Wang, K., Ha, J., Kuhn, M., Navarro, I., Cui, J., Young, K., Gorijavolu, R., 2021. Anti-fibrotic activity of a rho-kinase inhibitor restores outflow function and intraocular pressure homeostasis. Elife 10, e60831.

Lukomska, B., Stanaszek, L., Zuba-Surma, E., Legosz, P., Sarzynska, S., Drela, K., 2019. Challenges and Controversies in Human Mesenchymal Stem Cell Therapy. Stem Cells Int. 2019, e9628536. https://doi.org/10.1155/2019/9628536

Lütjen-Drecoll, E., Rittig, M., Rauterberg, J., Jander, R., Mollenhauer, J., 1989. Immunomicroscopical study of type VI collagen in the trabecular meshwork of normal and glaucomatous eyes. Exp. Eye Res. 48, 139–147. https://doi.org/10.1016/0014-4835(89)90027-4

Lütjen-Drecoll, E., Shimizu, T., Rohrbach, M., Rohen, J.W., 1986. Quantitative analysis of “plaque material” in the inner- and outer wall of Schlemm’s canal in normal- and glaucomatous eyes. Exp. Eye Res. 42, 443–455. https://doi.org/10.1016/0014-4835(86)90004-7

Maeda, A., Mandai, M., Takahashi, M., 2019. Gene and Induced Pluripotent Stem Cell Therapy for Retinal Diseases. Annu. Rev. Genomics Hum. Genet. 20, 201–216. https://doi.org/10.1146/annurev-genom-083118-015043

Mandai, M., Kurimoto, Y., Takahashi, M., 2017. Autologous Induced Stem-Cell-Derived Retinal Cells for Macular Degeneration. N. Engl. J. Med. 377, 792–793. https://doi.org/10.1056/NEJMc1706274

Manuguerra-Gagné, R., Boulos, P.R., Ammar, A., Leblond, F.A., Krosl, G., Pichette, V., Lesk, M.R., Roy, D.-C., 2013. Transplantation of mesenchymal stem cells promotes tissue regeneration in a glaucoma model through laser-induced paracrine factor secretion and progenitor cell recruitment. Stem Cells 31, 1136–1148.

Marcus, M., Smith, A., Maswadeh, A., Shemesh, Z., Zak, I., Motiei, M., Schori, H., Margel, S., Sharoni, A., Shefi, O., 2018. Magnetic Targeting of Growth Factors Using Iron Oxide Nanoparticles. Nanomaterials 8, 707. https://doi.org/10.3390/nano8090707

McDonald, R.J., McDonald, J.S., Kallmes, D.F., Jentoft, M.E., Murray, D.L., Thielen, K.R., Williamson, E.E., Eckel, L.J., 2015. Intracranial Gadolinium Deposition after Contrast-enhanced MR Imaging. Radiology 275, 772–782. https://doi.org/10.1148/radiol.15150025

McDowell, C.M., Kizhatil, K., Elliott, M.H., Overby, D.R., van Batenburg-Sherwood, J., Millar, J.C., Kuehn, M.H., Zode, G., Acott, T.S., Anderson, M.G., 2022. Consensus recommendation for mouse models of ocular hypertension to study aqueous humor outflow and its mechanisms. Invest. Ophthalmol. Vis. Sci. 63, 12–12.

Moore, M.J., Sebastian, J.A., Kolios, M.C., 2019. Determination of cell nucleus-to-cytoplasmic ratio using imaging flow cytometry and a combined ultrasound and photoacoustic technique: a comparison study. J. Biomed. Opt. 24, 106502. https://doi.org/10.1117/1.JBO.24.10.106502

Morris, C.A., Crowston, J.G., Lindsey, J.D., Danias, J., Weinreb, R.N., 2006. Comparison of invasive and non-invasive tonometry in the mouse. Exp. Eye Res. 82, 1094–1099. https://doi.org/10.1016/j.exer.2005.12.001

Morrison, J.C., Moore, C.G., Deppmeier, L.M., Gold, B.G., Meshul, C.K., Johnson, E.C., 1997. A rat model of chronic pressure-induced optic nerve damage. Exp. Eye Res. 64, 85–96.

Murugadoss, S., Lison, D., Godderis, L., Van Den Brule, S., Mast, J., Brassinne, F., Sebaihi, N., Hoet, P.H., 2017. Toxicology of silica nanoparticles: an update. Arch. Toxicol. 91, 2967–3010. https://doi.org/10.1007/s00204-017-1993-y

Neri, S., 2019. Genetic Stability of Mesenchymal Stromal Cells for Regenerative Medicine Applications: A Fundamental Biosafety Aspect. Int. J. Mol. Sci. 20, 2406. https://doi.org/10.3390/ijms20102406

Noecker, R.J., 2006. The management of glaucoma and intraocular hypertension: current approaches and recent advances. Ther. Clin. Risk Manag. 2, 193–206.

Olson, L., Seiger, Å., 1972. Brain tissue transplanted to the anterior chamber of the eye. Z. Für Zellforsch. Mikrosk. Anat. 135, 175–194. https://doi.org/10.1007/BF00315125

Overby, D.R., Bertrand, J., Tektas, O.-Y., Boussommier-Calleja, A., Schicht, M., Ethier, C.R., Woodward, D.F., Stamer, W.D., Lütjen-Drecoll, E., 2014. Ultrastructural Changes Associated With Dexamethasone-Induced Ocular Hypertension in Mice. Invest. Ophthalmol. Vis. Sci. 55, 4922–4933. https://doi.org/10.1167/iovs.14-14429

Pease, M.E., Cone, F.E., Gelman, S., Son, J.L., Quigley, H.A., 2011. Calibration of the TonoLab Tonometer in Mice with Spontaneous or Experimental Glaucoma. Invest. Ophthalmol. Vis. Sci. 52, 858–864. https://doi.org/10.1167/iovs.10-5556

Perazella, M.A., 2009. Current status of gadolinium toxicity in patients with kidney disease. Clin. J. Am. Soc. Nephrol. CJASN 4, 461–469. https://doi.org/10.2215/CJN.06011108

Polak, J.M., Bishop, A.E., 2006. Stem cells and tissue engineering: past, present, and future. Ann. N. Y. Acad. Sci. 1068, 352–366.

Progatzky, F., Dallman, M.J., Lo Celso, C., 2013. From seeing to believing: labelling strategies for in vivo cell-tracking experiments. Interface Focus 3, 20130001. https://doi.org/10.1098/rsfs.2013.0001

Provenzano, R., Schiller, B., Rao, M., Coyne, D., Brenner, L., Pereira, B.J.G., 2009. Ferumoxytol as an Intravenous Iron Replacement Therapy in Hemodialysis Patients. Clin. J. Am. Soc. Nephrol. CJASN 4, 386–393. https://doi.org/10.2215/CJN.02840608

Qiu, Y., Yang, H., Lei, B., 2014. Effects of three commonly used anesthetics on intraocular pressure in mouse. Curr. Eye Res. 39, 365–369. https://doi.org/10.3109/02713683.2013.845224

Raghunathan, V.K., Benoit, J., Kasetti, R., Zode, G., Salemi, M., Phinney, B.S., Keller, K.E., Staverosky, J.A., Murphy, C.J., Acott, T., Vranka, J., 2018. Glaucomatous cell derived matrices differentially modulate non-glaucomatous trabecular meshwork cellular behavior. Acta Biomater. 71, 444–459. https://doi.org/10.1016/j.actbio.2018.02.037

Reardon, G., Kotak, S., Schwartz, G.F., 2011. Objective assessment of compliance and persistence among patients treated for glaucoma and ocular hypertension: a systematic review. Patient Prefer. Adherence 441–463.

Rodríguez-Fuentes, D.E., Fernández-Garza, L.E., Samia-Meza, J.A., Barrera-Barrera, S.A., Caplan, A.I., Barrera-Saldaña, H.A., 2021. Mesenchymal Stem Cells Current Clinical Applications: A Systematic Review. Arch. Med. Res. 52, 93–101. https://doi.org/10.1016/j.arcmed.2020.08.006

Roubeix, C., Godefroy, D., Mias, C., Sapienza, A., Riancho, L., Degardin, J., Fradot, V., Ivkovic, I., Picaud, S., Sennlaub, F., 2015. Intraocular pressure reduction and neuroprotection conferred by bone marrow-derived mesenchymal stem cells in an animal model of glaucoma. Stem Cell Res. Ther. 6, 1–13.

Sadeghiani, N., Barbosa, L.S., Silva, L.P., Azevedo, R.B., Morais, P.C., Lacava, Z.G.M., 2005. Genotoxicity and inflammatory investigation in mice treated with magnetite nanoparticles surface coated with polyaspartic acid. J. Magn. Magn. Mater., Proceedings of the 10th International Conference on Magnetic Fluids 289, 466–468. https://doi.org/10.1016/j.jmmm.2004.11.131

Saeki, T., Aihara, M., Ohashi, M., Araie, M., 2008. The efficacy of TonoLab in detecting physiological and pharmacological changes of mouse intraocular pressure--comparison with TonoPen and microneedle manometery. Curr. Eye Res. 33, 247–252. https://doi.org/10.1080/02713680801919716

Samples, J.R., Bradley, J.M., Bacon, D.R., Bylsma, S.S., Van Buskirk, E.M., Acott, T.S., 1989. Trabecular repopulation by anterior trabecular meshwork cells after laser trabeculoplasty. Am. J. Ophthalmol. 107, 1–6.

Samsel, P.A., Kisiswa, L., Erichsen, J.T., Cross, S.D., Morgan, J.E., 2011. A novel method for the induction of experimental glaucoma using magnetic microspheres. Invest. Ophthalmol. Vis. Sci. 52, 1671–1675. https://doi.org/10.1167/iovs.09-3921

Sappington, R.M., Carlson, B.J., Crish, S.D., Calkins, D.J., 2010. The Microbead Occlusion Model: A Paradigm for Induced Ocular Hypertension in Rats and Mice. Invest. Ophthalmol. Vis. Sci. 51, 207–216. https://doi.org/10.1167/iovs.09-3947

Savinova, O.V., Sugiyama, F., Martin, J.E., Tomarev, S.I., Paigen, B.J., Smith, R.S., John, S.W., 2001. Intraocular pressure in genetically distinct mice: an update and strain survey. BMC Genet. 2, 12. https://doi.org/10.1186/1471-2156-2-12

Schiller, B., Bhat, P., Sharma, A., 2014. Safety and effectiveness of ferumoxytol in hemodialysis patients at 3 dialysis chains in the United States over a 12-month period. Clin. Ther. 36, 70–83. https://doi.org/10.1016/j.clinthera.2013.09.028

Sherwood, J.M., Boazak, E.M., Feola, A.J., Parker, K., Ethier, C.R., Overby, D.R., 2019. Measurement of Ocular Compliance Using iPerfusion. Front. Bioeng. Biotechnol. 7, 276. https://doi.org/10.3389/fbioe.2019.00276

Sherwood, J.M., Reina-Torres, E., Bertrand, J.A., Rowe, B., Overby, D.R., 2016. Measurement of outflow facility using iPerfusion. PloS One 11, e0150694.

Singh, N., Jenkins, G.J.S., Asadi, R., Doak, S.H., 2010. Potential toxicity of superparamagnetic iron oxide nanoparticles (SPION). Nano Rev. 1, 5358. https://doi.org/10.3402/nano.v1i0.5358

Snider, E.J., Hardie, B.A., Li, Y., Gao, K., Splaine, F., Kim, R.K., Vannatta, R.T., Read, A.T., Ethier, C.R., 2021. A porcine organ-culture glaucoma model mimicking trabecular meshwork damage using oxidative stress. Invest. Ophthalmol. Vis. Sci. 62, 18–18.

Snider, E.J., Kubelick, K.P., Tweed, K., Kim, R.K., Li, Y., Gao, K., Read, A.T., Emelianov, S., Ethier, C.R., 2018. Improving stem cell delivery to the trabecular meshwork using magnetic nanoparticles. Sci. Rep. 8, 1–13.

Sougawa, N., Miyagawa, S., Fukushima, S., Kawamura, A., Yokoyama, J., Ito, E., Harada, A., Okimoto, K., Mochizuki-Oda, N., Saito, A., Sawa, Y., 2018. Immunologic targeting of CD30 eliminates tumourigenic human pluripotent stem cells, allowing safer clinical application of hiPSC-based cell therapy. Sci. Rep. 8, 3726. https://doi.org/10.1038/s41598-018-21923-8

Spinowitz, B.S., Kausz, A.T., Baptista, J., Noble, S.D., Sothinathan, R., Bernardo, M.V., Brenner, L., Pereira, B.J.G., 2008. Ferumoxytol for treating iron deficiency anemia in CKD. J. Am. Soc. Nephrol. JASN 19, 1599–1605. https://doi.org/10.1681/ASN.2007101156

Stroh, A., Zimmer, C., Gutzeit, C., Jakstadt, M., Marschinke, F., Jung, T., Pilgrimm, H., Grune, T., 2004. Iron oxide particles for molecular magnetic resonance imaging cause transient oxidative stress in rat macrophages. Free Radic. Biol. Med. 36, 976–984. https://doi.org/10.1016/j.freeradbiomed.2004.01.016

Sun, Y., Williams, A., Waisbourd, M., Iacovitti, L., Katz, L.J., 2015. Stem cell therapy for glaucoma: science or snake oil? Surv. Ophthalmol. 60, 93–105.

Suryadevara, V., Hajipour, M.J., Adams, L.C., Aissaoui, N.M., Rashidi, A., Kiru, L., Theruvath, A.J., Huang, C., Maruyama, M., Tsubosaka, M., Lyons, J.K., Wu, W. (Emma), Roudi, R., Goodman, S.B., Daldrup-Link, H.E., 2023. MegaPro, a clinically translatable nanoparticle for in vivo tracking of stem cell implants in pig cartilage defects. Theranostics 13, 2710–2720. https://doi.org/10.7150/thno.82620

Takagi, S., Mandai, M., Gocho, K., Hirami, Y., Yamamoto, M., Fujihara, M., Sugita, S., Kurimoto, Y., Takahashi, M., 2019. Evaluation of Transplanted Autologous

Induced Pluripotent Stem Cell-Derived Retinal Pigment Epithelium in Exudative Age-Related Macular Degeneration. Ophthalmol. Retina 3, 850–859. https://doi.org/10.1016/j.oret.2019.04.021

Tamm, E.R., 2009. The trabecular meshwork outflow pathways: Structural and functional aspects. Exp. Eye Res. 88, 648–655. https://doi.org/10.1016/j.exer.2009.02.007

Tamm, E.R., Fuchshofer, R., 2007. What Increases Outflow Resistance in Primary Open-angle Glaucoma? Surv. Ophthalmol. 52, S101–S104. https://doi.org/10.1016/j.survophthal.2007.08.002

Tham, Y.-C., Li, X., Wong, T.Y., Quigley, H.A., Aung, T., Cheng, C.-Y., 2014. Global prevalence of glaucoma and projections of glaucoma burden through 2040: a systematic review and meta-analysis. Ophthalmology 121, 2081–2090.

Thu, M.S., Bryant, L.H., Coppola, T., Jordan, E.K., Budde, M.D., Lewis, B.K., Chaudhry, A., Ren, J., Varma, N.R.S., Arbab, A.S., Frank, J.A., 2012. Self-assembling nanocomplexes by combining ferumoxytol, heparin and protamine for cell tracking by magnetic resonance imaging. Nat. Med. 18, 463–467. https://doi.org/10.1038/nm.2666

Tripathi, B.J., Tripathi, R.C., 1989. Neural crest origin of human trabecular meshwork and its implications for the pathogenesis of glaucoma. Am. J. Ophthalmol. 107, 583–590.

Tripathi, R.C., Li, J., Chan, W.F., Tripathi, B.J., 1994. Aqueous humor in glaucomatous eyes contains an increased level of TGF-beta 2. Exp. Eye Res. 59, 723–727. https://doi.org/10.1006/exer.1994.1158

Tsai, J.C., Kanner, E.M., 2005. Current and emerging medical therapies for glaucoma. Expert Opin. Emerg. Drugs 10, 109–118.

Tsuchiya, S., Higashide, T., Hatake, S., Sugiyama, K., 2021. Effect of inhalation anesthesia with isoflurane on circadian rhythm of murine intraocular pressure. Exp. Eye Res. 203, 108420. https://doi.org/10.1016/j.exer.2020.108420

Turner, A.J., Vander Wall, R., Gupta, V., Klistorner, A., Graham, S.L., 2017. DBA/2J mouse model for experimental glaucoma: pitfalls and problems. Clin. Experiment. Ophthalmol. 45, 911–922.

United States Food and Drug Administration, 2015. Feraheme (ferumoxytol) Injection Label [WWW Document]. URL https://www.accessdata.fda.gov/drugsatfda_docs/label/2015/022180s011s013lbl.pdf

Vahabikashi, A., Gelman, A., Dong, B., Gong, L., Cha, E.D.K., Schimmel, M., Tamm, E.R., Perkumas, K., Stamer, W.D., Sun, C., Zhang, H.F., Gong, H., Johnson, M., 2019. Increased stiffness and flow resistance of the inner wall of Schlemm's canal in glaucomatous human eyes. Proc. Natl. Acad. Sci. 116, 26555–26563. https://doi.org/10.1073/pnas.1911837116

van den Bosch, J.J.O.N., Pennisi, V., Mansouri, K., Weinreb, R.N., Thieme, H., Hoffmann, M.B., Choritz, L., 2022. Effect of eyelid muscle action and rubbing on telemetrically obtained intraocular pressure in patients with glaucoma with an IOP sensor implant. Br. J. Ophthalmol.

Vandergriff, A.C., Hensley, T.M., Henry, E.T., Shen, D., Anthony, S., Zhang, J., Cheng, K., 2014. Magnetic targeting of cardiosphere-derived stem cells with ferumoxytol nanoparticles for treating rats with myocardial infarction. Biomaterials 35, 8528–8539. https://doi.org/10.1016/j.biomaterials.2014.06.031

Vitale, I., Manic, G., De Maria, R., Kroemer, G., Galluzzi, L., 2017. DNA damage in stem cells. Mol. Cell 66, 306–319.

Vranka, J.A., Acott, T.S., 2017. Pressure-induced expression changes in segmental flow regions of the human trabecular meshwork. Exp. Eye Res. 158, 67–72.

Wang, R.-F., Schumer, R.A., Serle, J.B., Podos, S.M., 1998. A comparison of argon laser and diode laser photocoagulation of the trabecular meshwork to produce the glaucoma monkey model. J. Glaucoma 7, 45–49.

Wang, X., Cao, Q., Wu, S., Bahrani Fard, M.R., Wang, N., Cao, J., Zhu, W., 2022. Magnetic Nano-Platform Enhanced iPSC-Derived Trabecular Meshwork Delivery and Tracking Efficiency. Int. J. Nanomedicine 17, 1285–1307. https://doi.org/10.2147/IJN.S346141

Weerasuriya, D.R.K., Bhakta, S., Hiniduma, K., Dixit, C.K., Shen, M., Tobin, Z., He, J., Suib, S.L., Rusling, J.F., 2021. Magnetic Nanoparticles with Surface Nanopockets for Highly Selective Antibody Isolation. ACS Appl. Bio Mater. 4, 6157–6166. https://doi.org/10.1021/acsabm.1c00502

Weinreb, R.N., Aung, T., Medeiros, F.A., 2014. The pathophysiology and treatment of glaucoma: a review. Jama 311, 1901–1911.

Wippold, F.J., Perry, A., 2006. Neuropathology for the Neuroradiologist: Rosettes and Pseudorosettes. AJNR Am. J. Neuroradiol. 27, 488–492.

Xiong, S., Kumar, A., Tian, S., Taher, E.E., Yang, E., Kinchington, P.R., Xia, X., Du, Y., 2021. Stem cell transplantation rescued a primary open-angle glaucoma mouse model. eLife 10, e63677. https://doi.org/10.7554/eLife.63677

Yamanaka, S., 2020. Pluripotent Stem Cell-Based Cell Therapy-Promise and Challenges. Cell Stem Cell 27, 523–531. https://doi.org/10.1016/j.stem.2020.09.014

Yu, T., Greish, K., McGill, L.D., Ray, A., Ghandehari, H., 2012. Influence of Geometry, Porosity, and Surface Characteristics of Silica Nanoparticles on Acute Toxicity: Their Vasculature Effect and Tolerance Threshold. ACS Nano 6, 2289–2301. https://doi.org/10.1021/nn2043803

Yun, H., Wang, Y., Zhou, Y., Kumar, A., Wang, K., Sun, M., Stolz, D.B., Xia, X., Ethier, C.R., Du, Y., 2018. Human stem cells home to and repair laser-damaged trabecular meshwork in a mouse model. Commun. Biol. 1, 216.

Zhang, D., Vetrivel, L., Verkman, A.S., 2002. Aquaporin Deletion in Mice Reduces Intraocular Pressure and Aqueous Fluid Production. J. Gen. Physiol. 119, 561–569. https://doi.org/10.1085/jgp.20028597

Zhou, Y., Xia, X., Yang, E., Wang, Y., Marra, K.G., Ethier, C.R., Schuman, J.S., Du, Y., 2020. Adipose-derived stem cells integrate into trabecular meshwork with glaucoma treatment potential. FASEB J. Off. Publ. Fed. Am. Soc. Exp. Biol. 34, 7160.

Zhu, W., Godwin, C.R., Cheng, L., Scheetz, T.E., Kuehn, M.H., 2020. Transplantation of iPSC-TM stimulates division of trabecular meshwork cells in human eyes. Sci. Rep. 10, 2905. https://doi.org/10.1038/s41598-020-59941-0

Zhu, W., Gramlich, O.W., Laboissonniere, L., Jain, A., Sheffield, V.C., Trimarchi, J.M., Tucker, B.A., Kuehn, M.H., 2016. Transplantation of iPSC-derived TM cells rescues glaucoma phenotypes in vivo. Proc. Natl. Acad. Sci. 113, E3492–E3500.

Zhu, W., Hou, F., Fang, J., Fard, M.R.B., Liu, Y., Ren, S., Wu, S., Qi, Y., Sui, S., Read, A.T., 2021. The role of Piezo1 in conventional aqueous humor outflow dynamics. Iscience 24, 102042.

Zhu, W., Jain, A., Gramlich, O.W., Tucker, B.A., Sheffield, V.C., Kuehn, M.H., 2017. Restoration of aqueous humor outflow following transplantation of iPSC-derived trabecular meshwork cells in a transgenic mouse model of glaucoma. Invest. Ophthalmol. Vis. Sci. 58, 2054–2062.

Zode, G.S., Kuehn, M.H., Nishimura, D.Y., Searby, C.C., Mohan, K., Grozdanic, S.D., Bugge, K., Anderson, M.G., Clark, A.F., Stone, E.M., Sheffield, V.C., 2011. Reduction of ER stress via a chemical chaperone prevents disease phenotypes in a mouse model of primary open angle glaucoma. J. Clin. Invest. 121, 3542–3553. https://doi.org/10.1172/JCI58183